MODELING OF PORE PRESSURE CHANGE, FAULT SLIP POTENTIAL AND INDUCED SEISMICITY IN FORT WORTH BASIN

A Thesis

by

CHANGQING YAO

Submitted to the Office of Graduate and Professional Studies of
Texas A&M University
in partial fulfillment of the requirements for the degree of

MASTER OF SCIENCE

Chair of Committee,	Akhil Datta-Gupta
Committee Member,	Michael J. King
	Debjyoti Banerjee
Head of Department,	Jeff Spath

May 2020

Major Subject: Petroleum Engineering

ABSTRACT

The seismicity rate in Fort-Worth Basin, north-central Texas, where a lot of hydrocarbon production and disposal water injection activities happen, has increased dramatically from 2008 till now. There are five main seismicity sequences in this region, which are DFW Airport Earthquake (2008), Cleburne Earthquake (2010), Azle Earthquake (2013), Irving Earthquake (2014) and Venus Earthquake (2015). Previous studies attribute the seismicity events to pore pressure increase caused by wastewater injection into Ellenburger Formation. However, hydrocarbon production from the overlying Barnett Shale is not included in those previous studies. This study introduces a 10 year analysis comparing regional seismicity with Fort-Worth Basin wide production and injection activities.

In order to better understand the controlling mechanism of induced seismicity and its relationship to hydrocarbon production and disposal water injection, a 3D heterogeneous basin model, including monthly injection rate for 112 injectors and monthly production rate for more than 18000 producers is constructed. The model incorporates all available well log data, stratigraphic data from more than 1200 wells and petrophysical analysis of 47 wells. Moreover, fault permeability, which enhances the permeability of the carbonate system, is added to further adjust the model.

For the purpose of improving simulation efficiency during model calibration process, a combination of layer and areal coarsening is used to reduce the computational cost. The areal coarsening approach follows a regular structured upgridding, while for the

layer upgridding we adopt the optimal layer coarsening approach. The coarsened model is then calibrated using a streamline-based inversion method, constrained by the bottom hole pressure (BHP) of 122 injection wells while honoring their injection volume history over 10 years.

Fluid flow simulation is then performed on the calibrated coarsened model to provide a basin-wide pore pressure distribution, serving as a fundamental step to find controlling mechanism for seismicity events and assess fault reactivation potential. Then, fault slip potential is calculated based on the time variant pore pressure and fault framework model to further analyze the controlling mechanism of seismic events in the Fort Worth Basin. All earthquake sequences, except for Azle earthquakes, were found to be triggered by pore pressure increase. We proposed a different controlling mechanism for the phenomenon we observed in Azle area, which is the unbalanced loading on two sides of a critically stressed fault. A site-specific study of Azle was conducted to further validate this mechanism.

DEDICATION

To my beloved family and friends.

ACKNOWLEDGEMENTS

I would like to thank my committee chair, Dr. Akhil Datta-gupta, for providing academic guidance and support throughout my study at TAMU. Also, I appreciate his understanding and support for helping me against difficulties.

Also, I would like to thank my committee members, Dr. Michael J. King and Dr. Debjyoti Banerjee, for their guidance and support throughout the course of this research.

Thanks also go to my MCERI colleagues for their patient teaching and guidance throughout my research work.

Finally, thanks to my family members for their encouragement, patience and love.

CONTRIBUTORS AND FUNDING SOURCES

Contributors

This work was supervised by a thesis committee consisting of Professor Akhil Datta-Gupta, Michael J. King of the Department of Petroleum Engineering and Professor Debjyoti Banerjee of the Department of Mechanical Engineering.

The site-specific study of Azle area and basin-wide pore pressure analysis is a collaborative project with Texnet-CISR.

All other work conducted for the thesis was completed by the student independently.

Funding Sources

This work was made possible by the financial support of the member companies of the Model Calibration and Efficient Reservoir Imaging (MCERI) consortium.

TABLE OF CONTENTS

Page

ABSTRACT ii

DEDICATION iv

ACKNOWLEDGEMENTS v

CONTRIBUTORS AND FUNDING SOURCES vi

TABLE OF CONTENTS vii

LIST OF FIGURES ix

LIST OF TABLES xiii

CHAPTER I INTRODUCTION 1

1.1 Background of Induced Seismicity 2
1.2 Background of Optimal Layer Coarsening 4
1.3 Background of Streamline-Based History Matching 5
1.4 Objectives and Thesis Outline 6

CHAPTER II MODEL DESCRIPTION 9

2.1 Data Sources 9
2.2 Permeability Characterization 12
2.3 Permeability Adjustment from Faults 13
2.4 Summary 15

CHAPTER III UPSCALING AND MODEL CALIBRATION 17

3.1 Introduction 17
3.2 Geologic Model Upscaling 17
3.3 Streamline-based Model Calibration 31
3.4 Summary 37

CHAPTER IV PORE PRESSURE AND FAULT SLIP POTENTIAL ANALYSIS 39

4.1 Introduction 39
4.2 Pore Pressure Analysis 41
4.3 Fault Slip Potential Analysis 54
4.4 Azle Site-Specific Study 68
4.5 Summary 74

CHAPTER V SUMMARY AND RECOMMENDATIONS 75

5.1 Summary 75
5.2 Recommendation 78

REFERENCES 79

APPENDIX A TUBING HEAD PRESSURE (THP) TO BOTTOM HOLE PRESSURE (BHP) 83

APPENDIX B GAS PRODUCTION CALCULATION 85

APPENDIX C FAULT SLIP POTENTIAL CALCULATION AND RESULTS 87

LIST OF FIGURES

Page

Figure 1.1 3D Heterogeneous Model of Fort-Worth Basin 2

Figure 2.1 Fault framework model of Fort Worth Basin 10

Figure 2.2 Comparison of field water production vs. time between original dataset and the approximated dataset 12

Figure 2.3 Distribution of (a) permeability index and (b) permeability 13

Figure 2.4 Distribution of (a) matrix permeability, (b) fault/fracture permeability and (c) adjusted permeability 14

Figure 3.1 Variation of heterogeneity 19

Figure 3.2 Cross-section of porosity field of (a) Fine scale (b) 64 Layers (c) 52 Layers (d) 48 Layers 20

Figure 3.3 Cross-section of permeability field of (a) Fine scale (b) 64 Layers (c) 52 Layers (d) 48 Layers 21

Figure 3.4 Well configuration of model used for validation 22

Figure 3.5 Validation of upscaling based on TOF from injector (a) Fine scale (b) 64 Layers (c) 52 Layers (d) 48 Layers 23

Figure 3.6 Validation of upscaling based on TOF from producers (a) Fine scale (b) 64 Layers (c) 52 Layers (d) 48 Layers 24

Figure 3.7 Validation of upscaling based on streamline partitions from injectors (a) Fine scale (b) 64 Layers (c) 52 Layers (d) 48 Layers 25

Figure 3.8 Validation of upscaling based on streamline partitions from producers (a) Fine scale (b) 64 Layers (c) 52 Layers (d) 48 Layers 26

Figure 3.9 Comparison of upscaled porosity field (a) 1x1x48 (b) 2x2x48 (c) 3x3x48 28

Figure 3.10 Comparison of upscaled permeability field (a) 1x1x48 (b) 2x2x48 (c) 3x3x48 29

Figure 3.11 Geological model upscaling validation, comparing simulation responses between fine and coarse models based on (a) field water injection rate (b) field water production rate (c) field average pressure 30

Figure 3.12 Comparison of (a) computational cost and (b) cell count between fine and coarse models....30

Figure 3.13 Streamline-based history matching workflow....31

Figure 3.14 Illustration of sensitivity calculation....33

Figure 3.15 Normalized data misfit vs. number of iterations....33

Figure 3.16 Well response shift after calibration....34

Figure 3.17 Illustration of sensitivity smoothing method....35

Figure 3.18 Permeability change after calibration in different layers....36

Figure 3.19 Flow pattern visualization of (a) initial model (b) updated model....38

Figure 4.1 Location map of earthquake sequences....40

Figure 4.2 County map superimposed with the permeability distribution of Viola Simpson....42

Figure 4.3 Produced fluid volumes used in this study (reservoir conditions)....43

Figure 4.4 Comparison of pore pressure change map in different years between (a) case with water production only (b) case with gas and water production....44

Figure 4.5 (a) Pore pressure change map in 2008 superimposed with DFW Airport Earthquake (b) zoom-in pore pressure change map in DFW Airport area....45

Figure 4.6 “South Well” monthly Injection Schedule....47

Figure 4.7 (a) Pore pressure change map in 2010 superimposed with Cleburne Earthquake (b) zoom-in pore pressure change map in Cleburne area....48

Figure 4.8 (a) Pore pressure change map in 2013 superimposed with Azle Earthquake (b) zoom-in pore pressure change map in Azle area....50

Figure 4.9 “North Well” monthly Injection Schedule....52

Figure 4.10 (a) Pore pressure change map in 2014 superimposed with Irving Earthquake (b) zoom-in pore pressure change map in Irving area....52

Figure 4.11 (a) Pore pressure change map in 2015 superimposed with Venus Earthquake (b) zoom-in pore pressure change map in Venus area....54

Figure 4.12 Fault framework model and partition of stress area 57

Figure 4.13 Fault slip potential change of Fort Worth Basin at 2008 58

Figure 4.14 Histogram of fault slip potential change of fault segments in (a) DFW Airport Area (b) Fort Worth Basin excludes study area (c) Fault held DFW Airport earthquake 59

Figure 4.15 Fault slip potential change of Fort Worth Basin at 2010 60

Figure 4.16 Histogram of fault slip potential change of fault segments in (a) Cleburne Area (b) Fort Worth Basin excludes study area (c) Fault held Cleburne earthquake 61

Figure 4.17 Fault slip potential change of Fort Worth Basin at 2013 62

Figure 4.18 Histogram of fault slip potential change of fault segments in (a) Azle Area (b) Fort Worth Basin excludes study area (c) Fault held Azle earthquake 63

Figure 4.19 Fault slip potential change of Fort Worth Basin at 2014 64

Figure 4.20 Histogram of fault slip potential change of fault segments in (a) Irving Area (b) Fort Worth Basin excludes study area (c) Fault held Irving earthquake 65

Figure 4.21 Fault slip potential change of Fort Worth Basin at 2015 66

Figure 4.22 Histogram of fault slip potential change of fault segments in (a) Venus Area (b) Fort Worth Basin excludes study area (c) Fault held Venus earthquake 67

Figure 4.23 Azle fine-scale geologic model 70

Figure 4.24 Normalized data misfit vs. number of iterations 71

Figure 4.25 Well response shift after calibration 71

Figure 4.26 (a) Horizontal view of streamlines from producers and injectors (10000 days cut-off) (b) vertical view of streamlines from producers and injectors 72

Figure 4.27 Pressure distribution along streamlines 72

Figure 4.28 Pore pressure change and poroelastic stress change at the top of basement (Chen et al. 2019) 73

Figure C1 Illustration example of Mohr-Circle 88

Figure C2 Illustration of stress transformation from principal to global 89

Figure C3 Illustration of stress transformation from global to fault plane.....90

Figure C4 Example illustrates FSP calculation.....91

Figure C5 Fault Slip Potential (FSP) of Fort Worth Basin at hydrostatic state 93

Figure C6 Fault Slip Potential (FSP) of Fort Worth Basin at 2008 superimposed with DFW Airport earthquake 94

Figure C7 Fault Slip Potential (FSP) of Fort Worth Basin at 2010 superimposed with Cleburne earthquake 95

Figure C8 Fault Slip Potential (FSP) of Fort Worth Basin at 2013 superimposed with Azle earthquake 96

Figure C9 Fault Slip Potential (FSP) of Fort Worth Basin at 2014 superimposed with Irving earthquake 97

Figure C10 Fault Slip Potential (FSP) of Fort Worth Basin at 2015 superimposed with Venus earthquake.....98

Figure C11 Illustration of the calculation of CDF 99

Figure C12 CDF of faults in Fort Worth Basin.....99

LIST OF TABLES

Page

Table 4.1 Well information of two injectors in DFW Airport Area…… 46

Table 4.2 Input Parameters for FSP Calculation……. 56

Table 4.3 Stress Gradients in Fort Worth Basin…….. 56

Table 4.4 Summary of mean FSP change in different area……. 68

CHAPTER I

INTRODUCTION

Within the last few years, seismicity events of magnitude range of 2 to 3, have occurred in an increased number in the central and eastern United States and have increased the visibility of induced seismic risk (Frohlich 2012a). The increase in number of earthquakes has been linked to oil and gas activities (Frohlich et al. 2012b; Hornbach et al. 2015; Chen et al. 2018). Both operators and regulators are under pressure from residents and media to investigate the controlling mechanism for the sharp increase in frequency of these seismicity events.

Several studies have been conducted to investigate these seismicity events and most of them attribute them to the wastewater injection near the fault regions and reactivation of the faults (Frohlich et al. 2011; Gono et al. 2015; Hornbach et al. 2015; Frohlich et al. 2016;). However, most of these studies did not include hydrocarbon production in their model.

In this study, a 3D heterogeneous basin model, including monthly injection rate for 112 injectors and monthly production rate for more than 18000 producers over the last 10 years is constructed (**Figure 1.1**). The model incorporates all available well log data, stratigraphic data of more than 1200 wells and petrophysical analysis of 47 wells. Moreover, fault permeability, which enhances the permeability of the carbonate system, is added to further adjust the model.

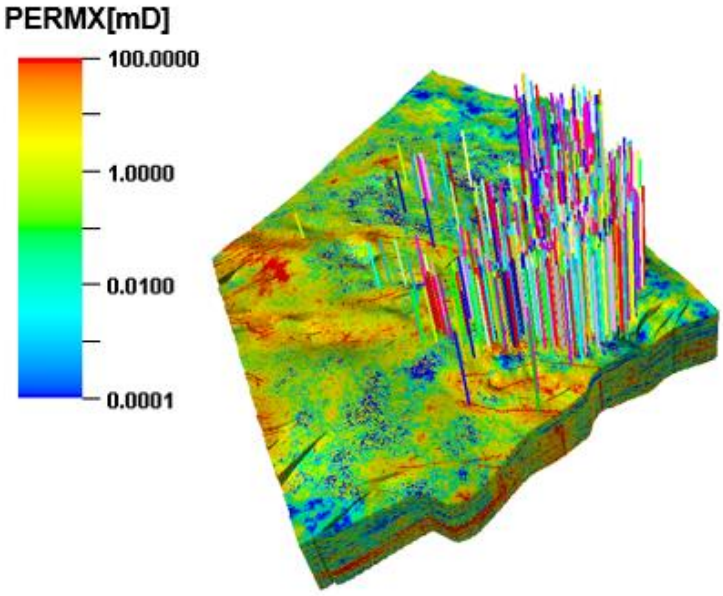

Figure 1.1 3D Heterogeneous Model of Fort-Worth Basin

This study provides a basin-wide pore pressure distribution to serve as a fundamental step to assess fault reactivation and gives insights to understand induced seismicity. Moreover, the areal extent of the pore pressure front is also of interest, since there is a possibility that the pore pressure front will extend further than the region in the proximity of the injection well. Understanding the areal extent and the magnitude of pore pressure response from fluid injection is a key factor in correlating induced seismicity and injection/production activities.

1.1 Background of Induced Seismicity

Induced seismicity has been studied from the last century. These studies could be categorized into site-specific study and basin-wide study. Hornbach (2015) constructed a fluid flow model for the Ellenburger formation of the Azle area to simulate pore pressure

change and found the pore pressure increase near the fault could trigger seismic events for near-critically stressed faults. Chen (2018) built a coupled fluid flow and geomechanical model for Azle area and attributed the cause of seismicity in Azle area to unbalanced loading on different sides of the fault. There are a lot more literatures in site-specific studies, but the important aspect of this study is basin-wide study, which will be reviewed more thoroughly.

Gono (2015) performed a basin-wide fluid flow simulation to study the correlation between seismicity and wastewater injection in Fort-Worth Basin. He found some spatial and temporal correlation between seismic activity and pore pressure change. He also found a lack of seismicity in areas of predicted increase in pressure, implying that favorably oriented and sized pre-existing faults are required in addition to the change in pore pressure in order to induce seismicity.

Frohlich et al. (2016) conducted a comprehensive analysis comparing regional seismicity with basin-wide injection volume in Fort-Worth Basin. They compared Ellenburger injection volumes to earthquake locations and rates and found that earthquakes often occurred in areas where the largest fluid volumes were injected into the Ellenburger.

Zhai (2018) applied a coupled poroelastic model to simulate the spatiotemporal evolution of pore pressure and poroelastic stresses at the basin-wide scale. The results suggested that the location and timing of the seismicity correspond to zones of increased pore pressure, poroelastic stress and total CFS change.

1.2 Background of Optimal Layer Coarsening

Using high resolution geological models for reservoir simulation is not computationally efficient, especially during history matching and optimization process (Durlofsky, et al. 1996; Li and Becker 2000). As a result, several upgridding and upscaling approaches are developed to improve computation efficiency (Li and Lake, 1995; Stern and Dawson, 1999; King, 2005; Hosseini and Kelkar, 2008; Du, 2012).

Li and Lake (1995) developed a method to upscale permeability globally while preserving the variance and spatial correlation for the whole permeability field. Li and Beckner (2000) presented a new static measure, which combined several reservoir properties as permeability, porosity, endpoint saturation, etc. A residual curve, showing how much heterogeneity could be preserved during coarsening, was generated.

Stern and Dawson (1999) proposed a sequential coarsening algorithm to select optimal locations for layer boundaries and calculate the number of layers needed. Their method was an iterative method to sequentially combine the layers from the bottom of the model that could minimize the changes of reservoir properties. Two objective functions were used to quantify the change of reservoir properties, which were the change in the time required for single-phase breakthrough in fine and coarse grid and flux difference between fine and coarse grid.

King (2005) presented a new way to measure reservoir heterogeneity, which was local velocity, the product of Buckley Leverett velocity and interstitial flow velocity within each layer. The preserved reservoir heterogeneity was maximized by combining the layers that minimize the deviation from the original fine scale variance.

Hosseini and Kelkar (2008) provided two new parameters for choosing the optimum number of layer, which were a design factor representing the quality of the layering design and the change of error per layer calculated at each step.

Du (2012) introduced two novel heterogeneity measures, “Velocity & Slowness” and Lorenz coefficient to predict optimal number of layers for convective dominated process.

1.3 Background of Streamline-Based History Matching

History matching is the process to integrate static data with dynamic data, which is production history, well test results or time-lapse seismic measurement data. Several history matching methods have been proposed, which could be categorized into manual, deterministic (Yang and Watson, 1988; Vega, Datta-Gupta, 2004; Hoffman, 2006) and stochastic method (Hastings, 1970; Granville, 1994). The stochastic method is typically a non-gradient method because it tries to search all of the solution space by the evolutionary algorithm, Monte-Carlo method or geosatistical method such as Ensemble Kalman Filter (Aanonsen et al. 2009, Tanaka et al. 2010) or smoother (Chen and Oliver 2012). These methods generally require multiple initial static models and update to find the global minimum of the solution space. The deterministic approach, or often called a gradient based approach is a method to find local or global minimum from a given single initial static data. The gradient method uses sensitivity of static data to production data to update the model. There is quite a bit of prior work to calculate sensitivity matrix efficiently. One example is the perturbation method and it requires (n+1) simulation with given n static

parameters. If static parameter is permeability of each grid cell, the number of simulations need to be conducted (number of discretized grid +1) times and thus, it is computationally expensive to update individual cell property (Dogru and Seinfeld 1981). The gradzone method is a practical approach for the perturbation method (Brun, Gosselin, and Barker 2004) because this approach samples static data and calculate parameter sensitivity sparsely and uses interpolation to extend sparse sensitivity to entire field. The gradient simulator or adjoint method (Dogru and Seinfeld 1981, Wu and Datta-Gupta 2002, Zhang et al. 2006, Daoud and Velasquez. 2006, Chen et al. 2020) is effective compared with perturbation method, because it requires one forward simulation and another system of adjoint equation. Thus, the computational cost is less than two simulations. However, this approach requires a system of linear equation, which is a discretized form of the flow equation and its derivative with respect to model parameters. Because of these reasons, it has difficulties in applicability unless the reservoir simulator can generate derivative of the discretized flow equation with respect to the static parameters.

Compared with these deterministic approaches, the streamline-based history matching has three main advantages. First, it is fast because of analytical ways of sensitivity calculation. Second, streamline based method enables updating of high-resolution geological models. Third, the approach can be applied using post processing from simulation results and can be applicable to any available simulator.

1.4 Objectives and Thesis Outline

The objectives of this study are as follows:

The basin-wide pore pressure analysis serves as a fundamental step to assess fault reactivation and gives some insights to understand induced seismicity. Moreover, the areal extent of the pore pressure front is also of interest, since there is a possibility that the pore pressure front will extend further than the region in the proximity of the injection well. Understanding the areal extent and the magnitude of pore pressure response from fluid injection is a key factor in correlating induced seismicity and injection/production activities. Now, we will outline the specific procedure of this thesis in Chapters II-V.

1) In Chapter II, a basin-wide 3D heterogeneous model is constructed using well log data, stratigraphic data from more than 1000 wells in the Fort Worth Basin. The heterogeneous geological model has 47 million grid cells and includes Barnett shale formation, Ellenburger formation with karstic platform carbonates and crystalline basement. Moreover, based on seismic reflection data, regional subsurface mapping and outcrop mapping, major faults and minor fractures are also included into this model. Monthly injection rate and pressure from 112 injectors over ten years from Texas Railroad Commission and production rate from 18000+ producers from Drilling Info are included into the model for fluid flow simulation.
2) In Chapter III, recursive sequential coarsening method is used to reduce the computational time and help with the history matching process during which multiple simulation runs will be conducted. A combination of areal coarsening and layer coarsening will decrease the number of grid cells in the model dramatically while preserving model heterogeneity. After

upscaling, streamline based inversion method is used to calibrate the model constrained by bottom hole pressure of 104 injectors.

3) In Chapter IV, basin-wide time variant pore pressure distribution from flow simulation results of the calibrated model is analyzed to find the correlation between pore pressure change and occurrence of seismic events. Then, fault slip potential is calculated based on the time variant pore pressure to further analyze the controlling mechanism of seismic events in the Fort Worth Basin.
4) Finally, in Chapter V, the research is concluded with a summary of the key findings. Recommendations and proposals for further research are also presented.

CHAPTER II

MODEL DESCRIPTION

In this chapter, the details of the geological model is discussed, including the data sources, permeability characterization and permeability adjustment.

2.1 Data Sources

The accuracy of the simulation results depends on the data building the model. This model utilizes all possible well log data, stratigraphic data and petrophysical analysis results. The description of the data used in the simulation as well as the data sources are explained in detail in the following subsections.

2.1.1 Geologic Model

Geologic model is provided by Bureau of Economic Geology (**Figure 1.1**), including corner point grid geometry, reservoir properties such as permeability index and porosity. The model has 90 million grid cells (725×714×173) and an areal extent of 281km × 403km. The model has 173 layers, including Barnett, Viola Simpson and Ellenburger. This model includes 251 faults interpreted based on a wide range of existing information (**Figure 2.1**), such as seismic reflection data, regional subsurface mapping, outcrop mapping, earthquake hypocenters and focal plane mechanisms and all publicly available information sources (Hennings et al, 2019). The petrophysical properties (permeability

index and porosity) are obtained based on well log data from more than 1200 wells and then populated in the model using Sequential Gaussian Simulation.

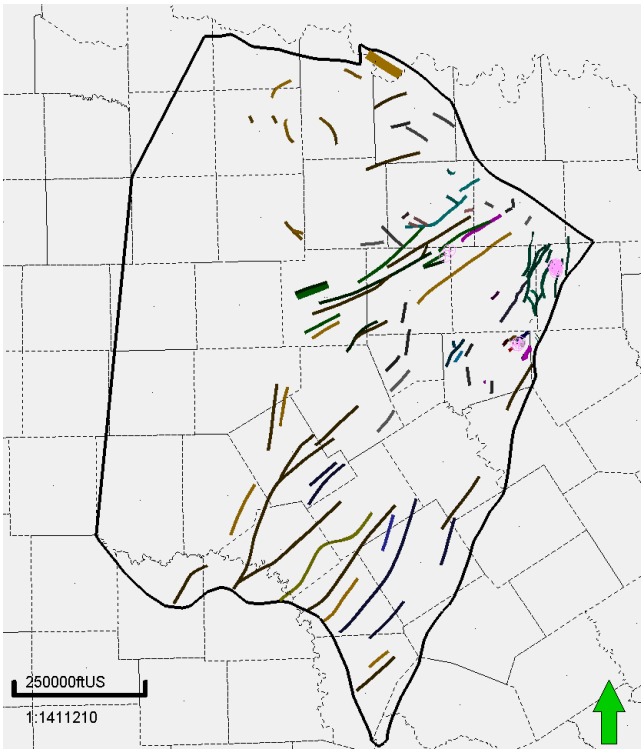

Figure 2.1 Fault framework model of Fort Worth Basin

2.1.2 Injection Data

The wastewater injection data of 122 injectors in Fort Worth Basin was obtained from the Railroad Commission of Texas (RRC), including well locations, injection volumes, injection depths and injection pressures.

The well locations were queried by the counties using the Injection & Disposal Query form by the county. Each injection well in the RRC database has an American Petroleum Institute (API) number and an Underground Injection Control (UIC) number.

The API number is unique to each well and the UIC number is a unique number issued for a specific well each time an injection permit is issued for the well.

The injection volume of each well was queried using the UIC number in the H10 Injection Volume Query. We could obtain monthly injection data of each well and total injection volumes for a specific county as well.

The injection pressure of each well, which was tubing head pressure, was queried using the UIC number in the Search for H10s Query. The tubing head pressure (THP) was then converted to Bottom Hole Pressure (BHP) as the reference data to calibrate the fluid flow model (Appendix A).

2.1.3 Production Data

Production data of more than 18,000 producers in Fort Worth Basin was queried from DrillingInfo, including well locations and monthly production rate of water and gas. Gas production rate was then converted from surface condition to bottom-hole conditions and equivalent reservoir fluid withdrawal rates (Appendix B).

To simplify the fluid flow model, a producer reduction procedure was taken. Producers that are located in the same cell are combined and the top 1153 combined producers are selected that contribute 90% of the total production (**Figure 2.2**).

2.1.4 Seismic Data

Seismic data was obtained from the United States Geological Survey (USGS) National Survey (USGS) National Earthquake Information Center (NEIC) database for

the Fort Worth Basin, including time, latitude, longitude and magnitude.

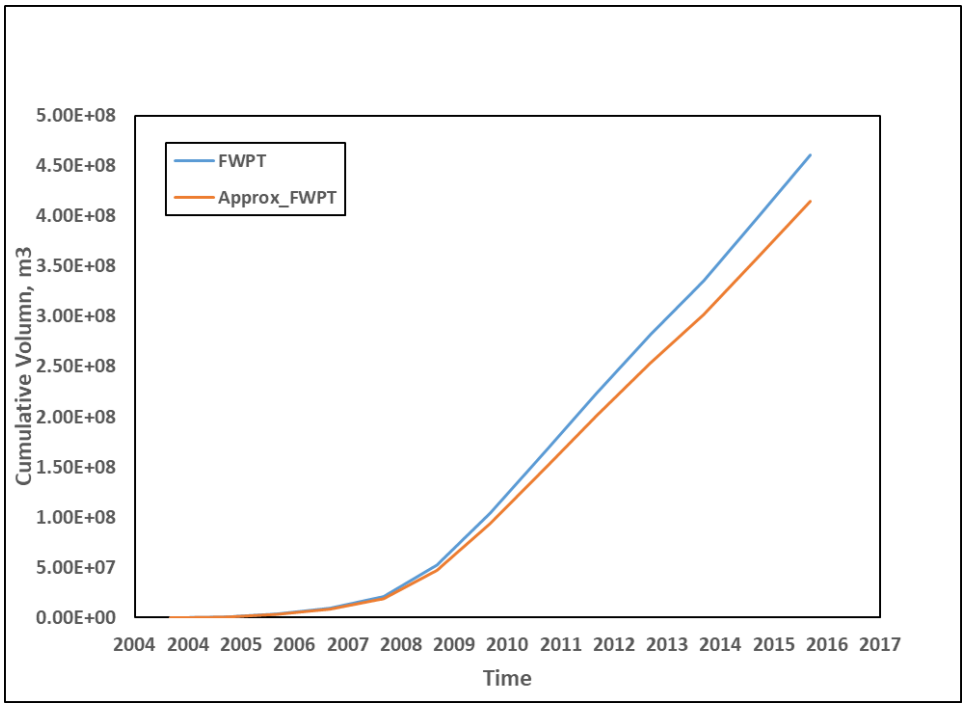

Figure 2.2 Comparison of field water production vs. time between original dataset and the approximated dataset

2.2 Permeability Characterization

The Fort Worth Basin geological model does not have permeability value, but permeability index instead, which need to be preprocessed and converted to permeability to be used in flow simulation. Average permeability of each group of Ellenburger, which are from the Azle site-specific study (Appendix C), were used as reference to convert permeability index to permeability. During this process, a multiplier is added to each group of Ellenburger to make sure the updated value is close to the reference value. After this calibration, we get permeability of Ellenburger, ranging from 10-4 to 100md (**Figure 2.3**), which will be used as inputs for flow simulation.

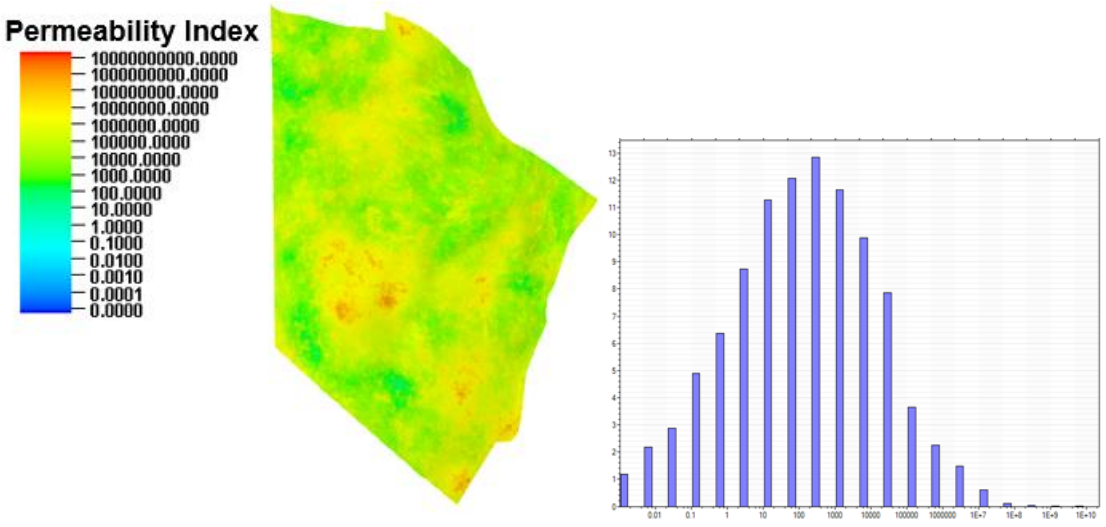

(a)

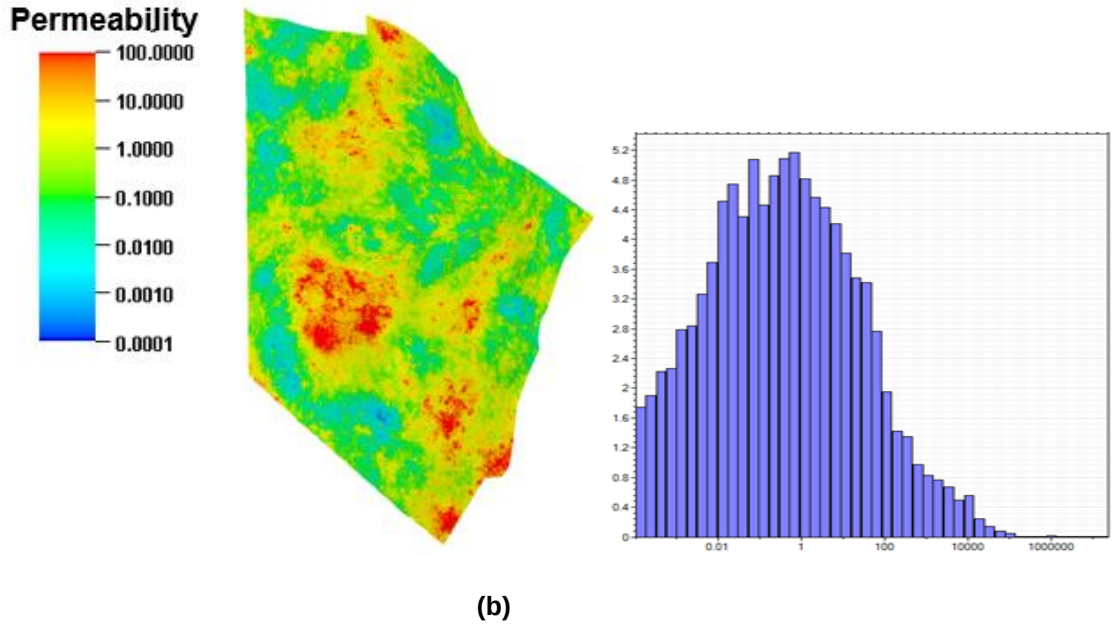

(b)

Figure 2.3 Distribution of (a) permeability index and (b) permeability

2.3 Permeability Adjustment from Faults

Ellenburger consists of karstic platform carbonates, with faults and fractures to enhance the permeability of the carbonate system. For the sake of simplicity and computation efficiency, single permeability single porosity (SPSP) model is preferred. So

the adjusted permeability is constructed by adding matrix permeability and fault/fracture permeability (**Figure 2.4**).

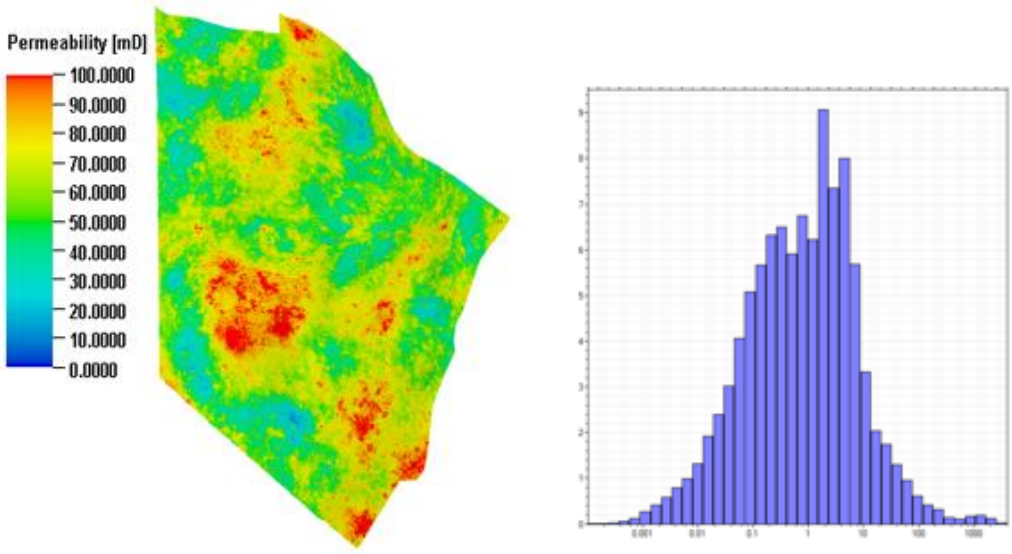

(a)

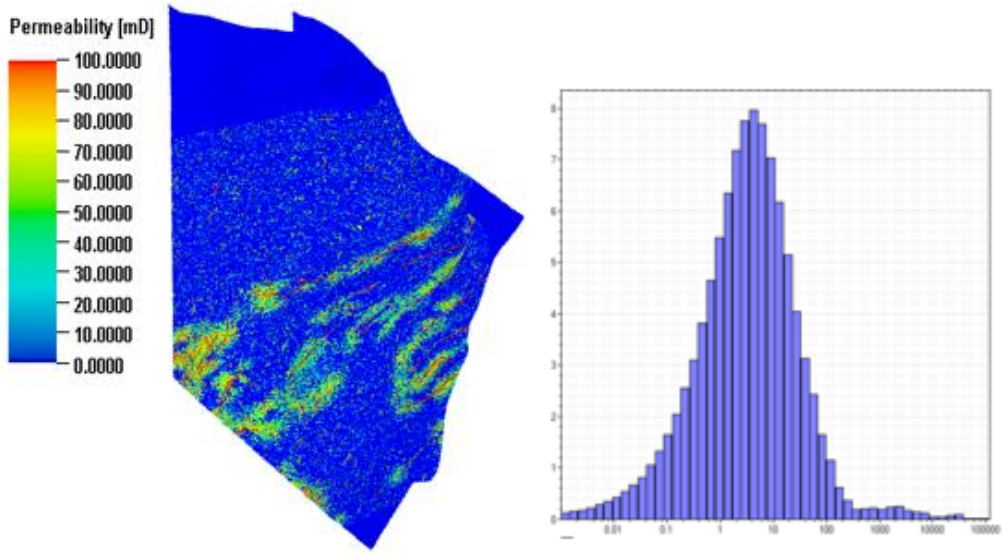

(b)

Figure 2.4 Distribution of (a) matrix permeability, (b) fault/fracture permeability and (c) adjusted permeability

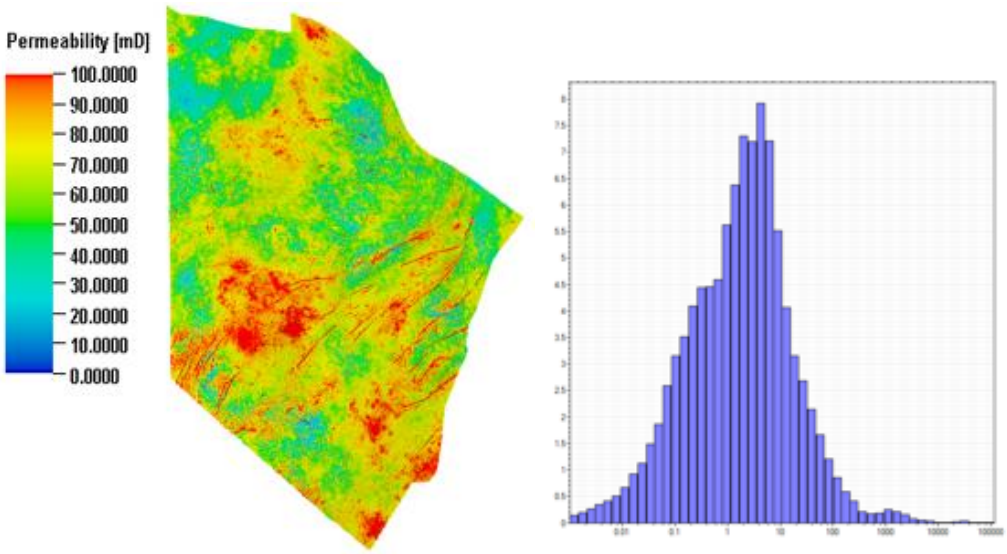

(c)

Figure 2.4 cont.

2.4 Summary

In this Chapter, the original geologic model has been descripted in detail. The Fort Worth Basin model is a basin-wide 3D heterogeneous model constructed using well log data, stratigraphic data from more than 1000 wells in the Fort Worth Basin. The heterogeneous geological model has 47 million grid cells and includes Barnett shale formation, Ellenburger formation with karstic platform carbonates and crystalline basement. Moreover, based on seismic reflection data, regional subsurface mapping and outcrop mapping, major faults and minor fractures are also included into this model. We also introduced sources for model inputs (well log, seismic reflection data, regional subsurface mapping etc.), wastewater injection data for 112 injectors over ten years, hydrocarbon gas production data for 18000+ producers and seismic data. We discussed the characterization of permeability field using permeability index based on the history

matched Azle site-specific model. Finally, we showed the permeability adjustment from faults to account for the permeability enhancement from minor faults and fractures and permeability reduction from major faults.

CHAPTER III

UPSCALING AND MODEL CALIBRATION

3.1 Introduction

High resolution geological model with high heterogeneity and large number of grid blocks (~47 million) is computationally demanding. It was therefore necessary to upscale the geologic model to improve simulation efficiency prior to carrying out model calibration. This chapter presents upscaling methodologies we applied, followed by the streamline-based calibration method.

3.2 Geologic Model Upscaling

As described in Chapter II, Fort Worth Basin model is a high resolution geological model constructed using all available well log data, stratigraphic data, petrophysical analysis and faults from outcrop data. Although accurate, it is not computationally feasible to use high resolution model for history matching and optimizations, which could require hundreds of reservoir simulations (Durlofsky, et al. 1996; Li and Becker 2000). Upscaling and upgridding methods are therefore developed to improve computational efficiency.

A trade-off between bias and variance exists during upscaling process: if coarsened too much, although it requires less simulation time, the model may lose geologic realism; if coarsened too little, the cost of the simulation model may remain too high. Therefore, it is desired to find an optimal coarsening scheme (King, et al. 2005).

For this study, a combination of layer and areal coarsening was conducted to reduce computational cost required for the following history matching step. The areal coarsening approach follows a regular structured upgridding (3x3, 5x5 upgridding, etc.) in commercial simulator, while for the layer upgridding we adopted the optimal layer coarsening approach (King, et al. 2005, S. Du 2012). The recursive sequential coarsening scheme will merge neighboring layers that results in the least loss of the total variation of heterogeneity defined by:

$$H = \sum_{i,j,k=1}^{NX,NY,NZ} n_{i,j,k}(P_{i,j,k} - \overline{P}_{i,j})^2 \tag{2.1}$$

And,

$$\overline{P}_{i,j} = \frac{\sum_{k=1}^{NZ} n_{i,j,k} \bullet P_{i,j,k}}{\sum_{k=1}^{NZ} n_{i,j,k}} \tag{2.2}$$

where $n_{i,j,k}$ is the net rock volume of the cell and $P_{i,j,k}$ is a proxy of flow speed given by the ratio of cell permeability and porosity, which is a combination of the local speed (k/ϕ) and the local slowness (ϕ/k). $\overline{P}_{i,j}$ is a bulk volume weighted average of $P_{i,j,k}$ for the (i, j) grid pillar. The optimal layer coarsening algorithm consists of two steps. First, we compute loss of heterogeneity between adjacent layer pairs (δW). A pair with minimum δW will be merged into a single layer and this procedure is repeated until the model becomes a single layer. Second, we need to find an optimal number of layer which is defined as the number of layers that could preserve major heterogeneity. We could specify the maximum number of layers to be merged into a single layer. In this study, we

used three different values: 12, 16, 18, resulting in 64, 52 and 48 layers, respectively. **Figure 3.1** shows the variation of heterogeneity with different layer coarsening schemes, where x-axis is the number of coarsened layers and y-axis is preserved relative heterogeneity. Comparison of cross-section of upscaled permeability and porosity with different layer coarsening schemes are shown in **Figure 3.2** and **Figure 3.3**. Areal coarsening was conducted to further reduce number of grid cells to reduce computational time for the following history matching procedure.

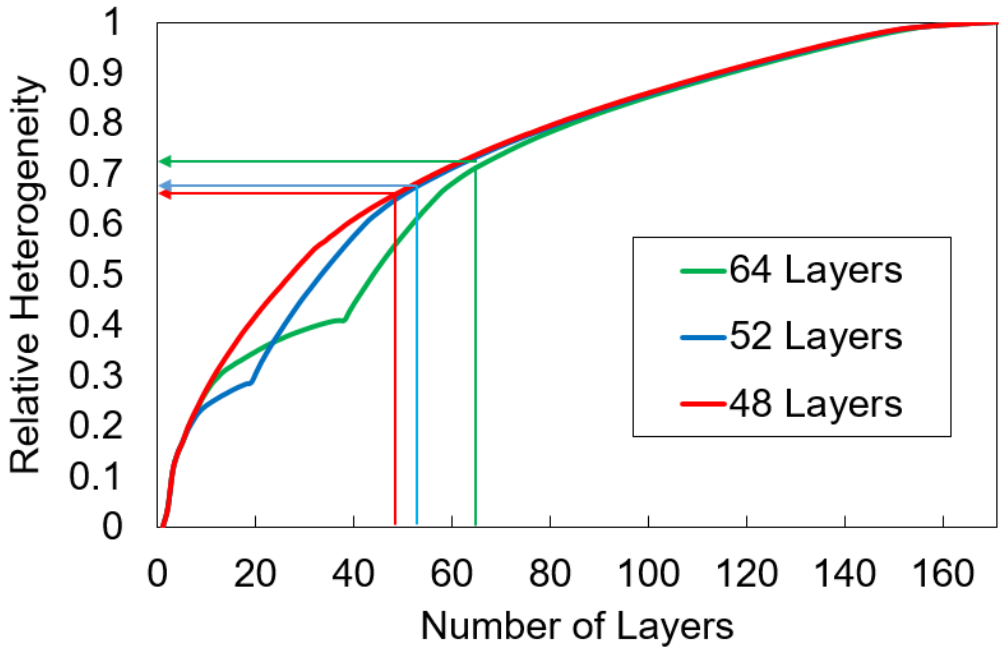

Figure 3.1 Variation of heterogeneity

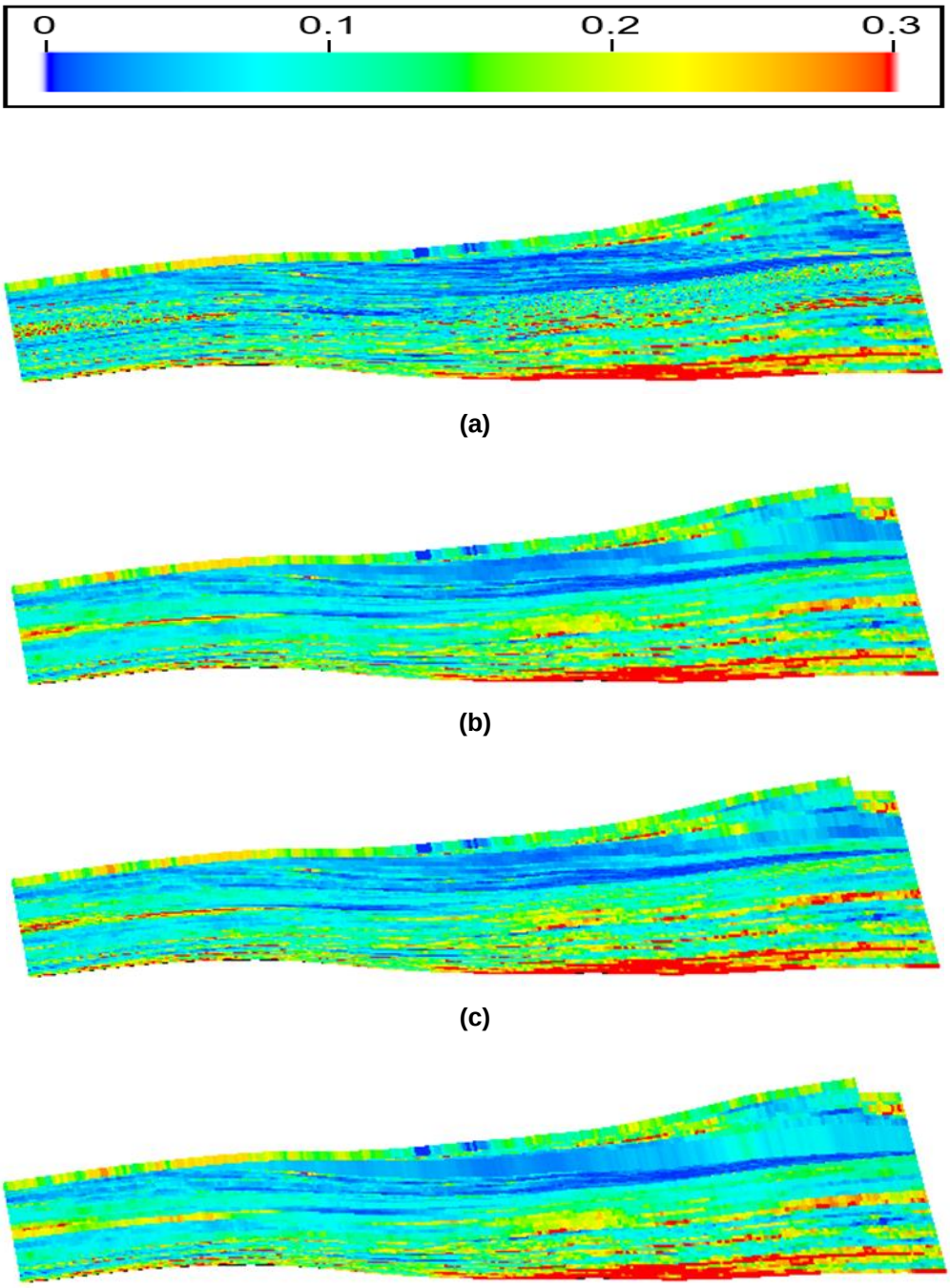

Figure 3.2 Cross-section of porosity field of (a) Fine scale (b) 64 Layers (c) 52 Layers (d) 48 Layers

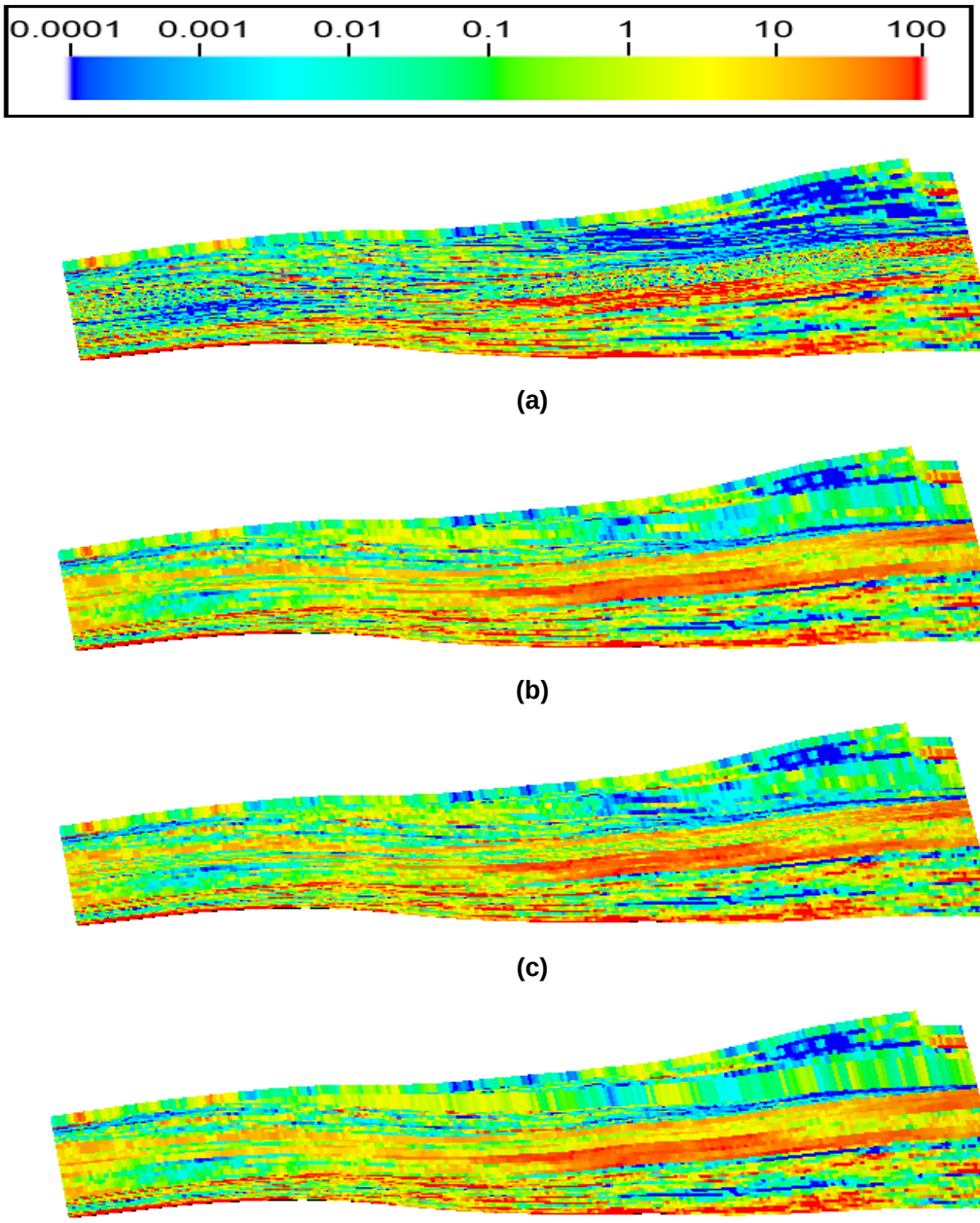

Figure 3.3 Cross-section of permeability field of (a) Fine scale (b) 64 Layers (c) 52 Layers (d) 48 Layers

Upscaling results were validated using single phase flow simulations, in which we put 13 injectors and 26 producers. **Figure 3.4** shows the well configuration of the model used for validation. Streamline time of flight (TOF), which is defined as travel time of a neural particle along streamlines (Datta-Gupta and King, 2007), from producers and injectors, and flow partitions from injectors and producers are compared for different layer coarsening schemes. **Figure 3.5**, **Figure 3.6**, **Figure 3.7**, **Figure 3.8** show TOF from injectors, TOF from producers, flow partitions from injectors (swept volume) and flow partitions from producers (drainage volume), respectively. Visual comparison shows consistent results between fine and coarse model, which validates our vertical upscaling approach.

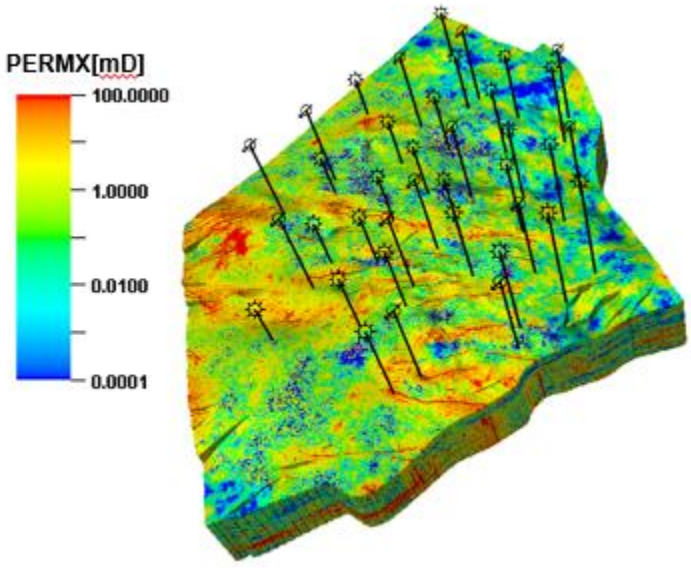

Figure 3.4 Well configuration of model used for validation

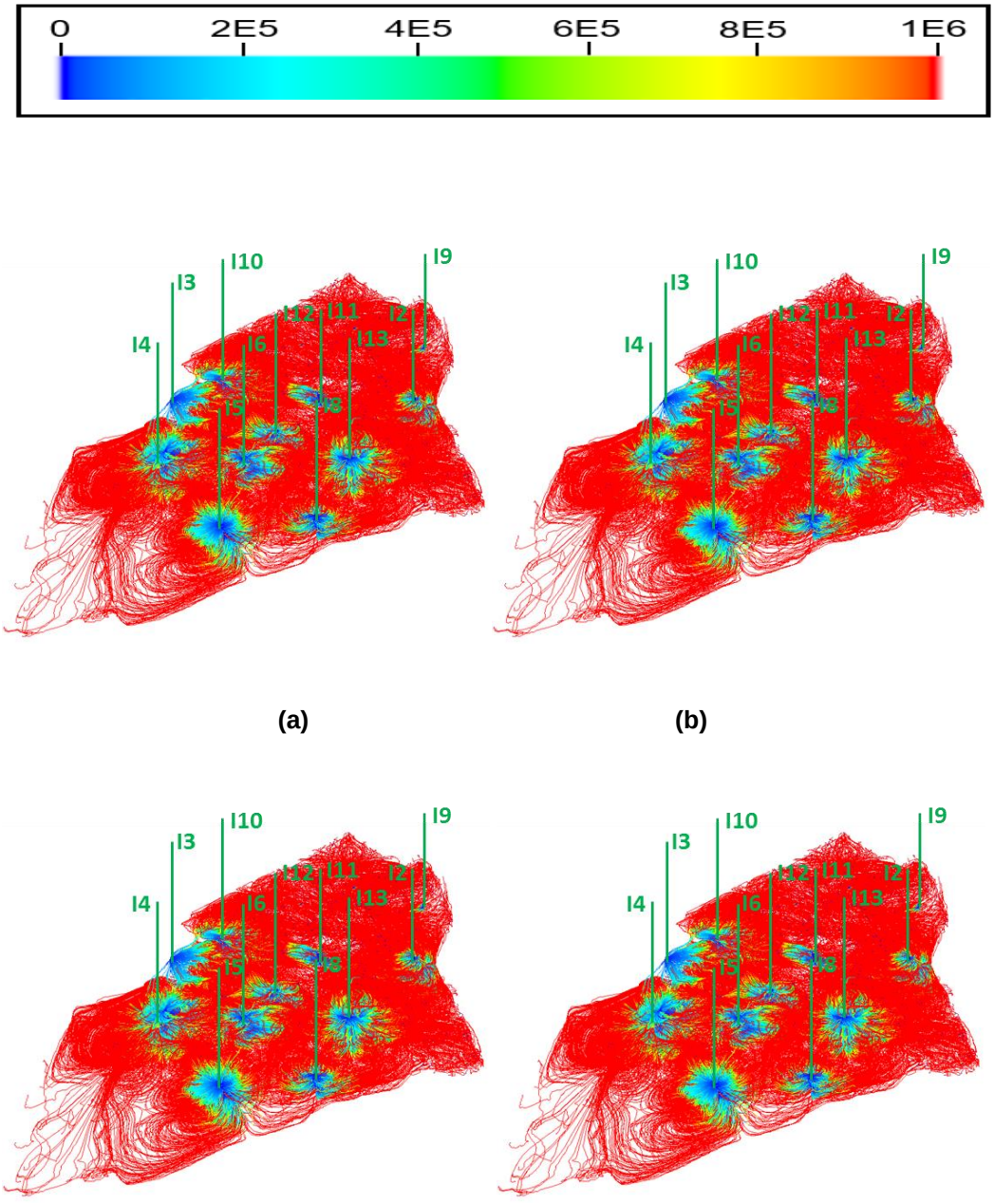

Figure 3.5 Validation of upscaling based on TOF from injector (a) Fine scale (b) 64 Layers (c) 52 Layers (d) 48 Layers

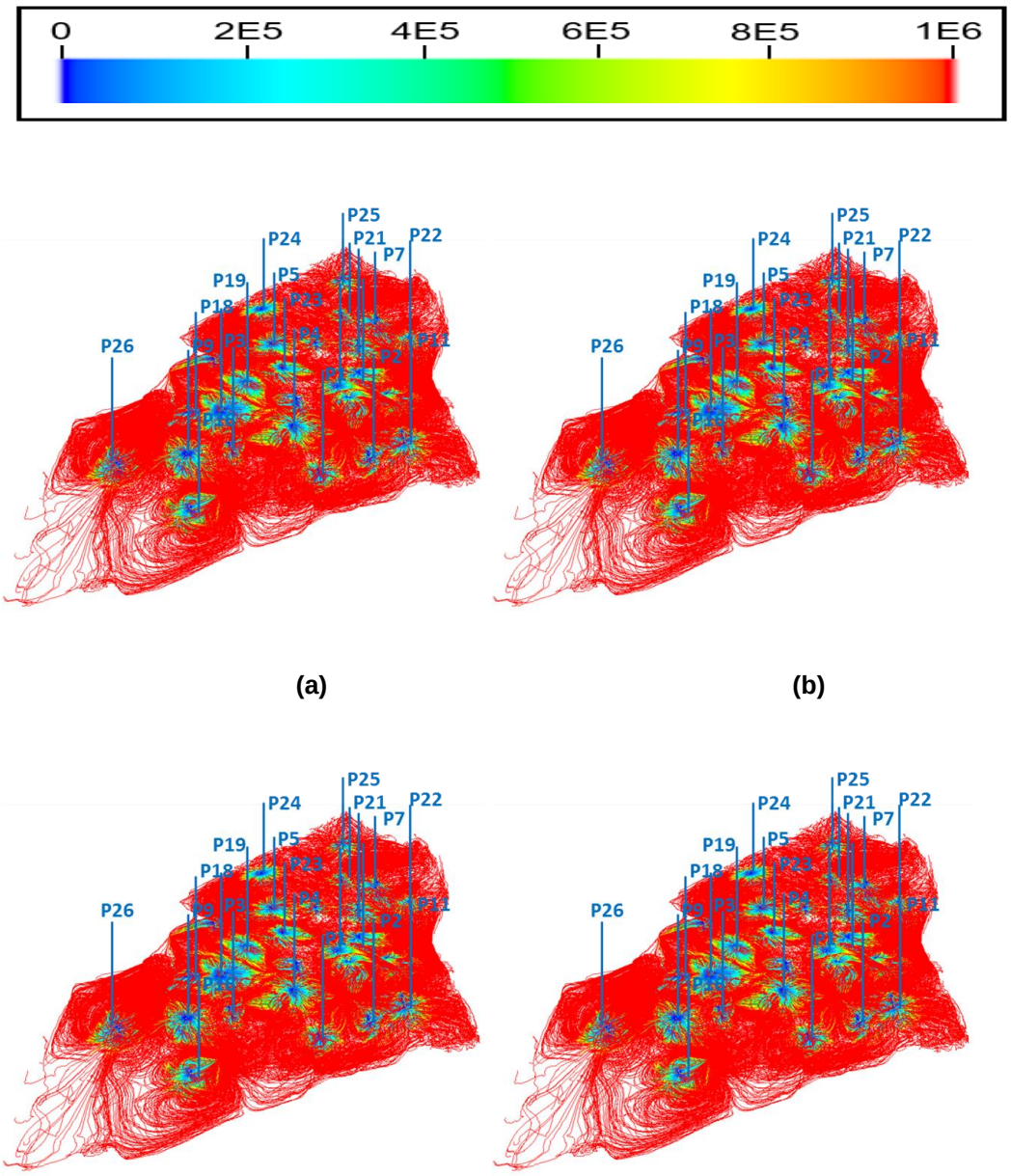

Figure 3.6 Validation of upscaling based on TOF from producers (a) Fine scale (b) 64 Layers (c) 52 Layers (d) 48 Layers

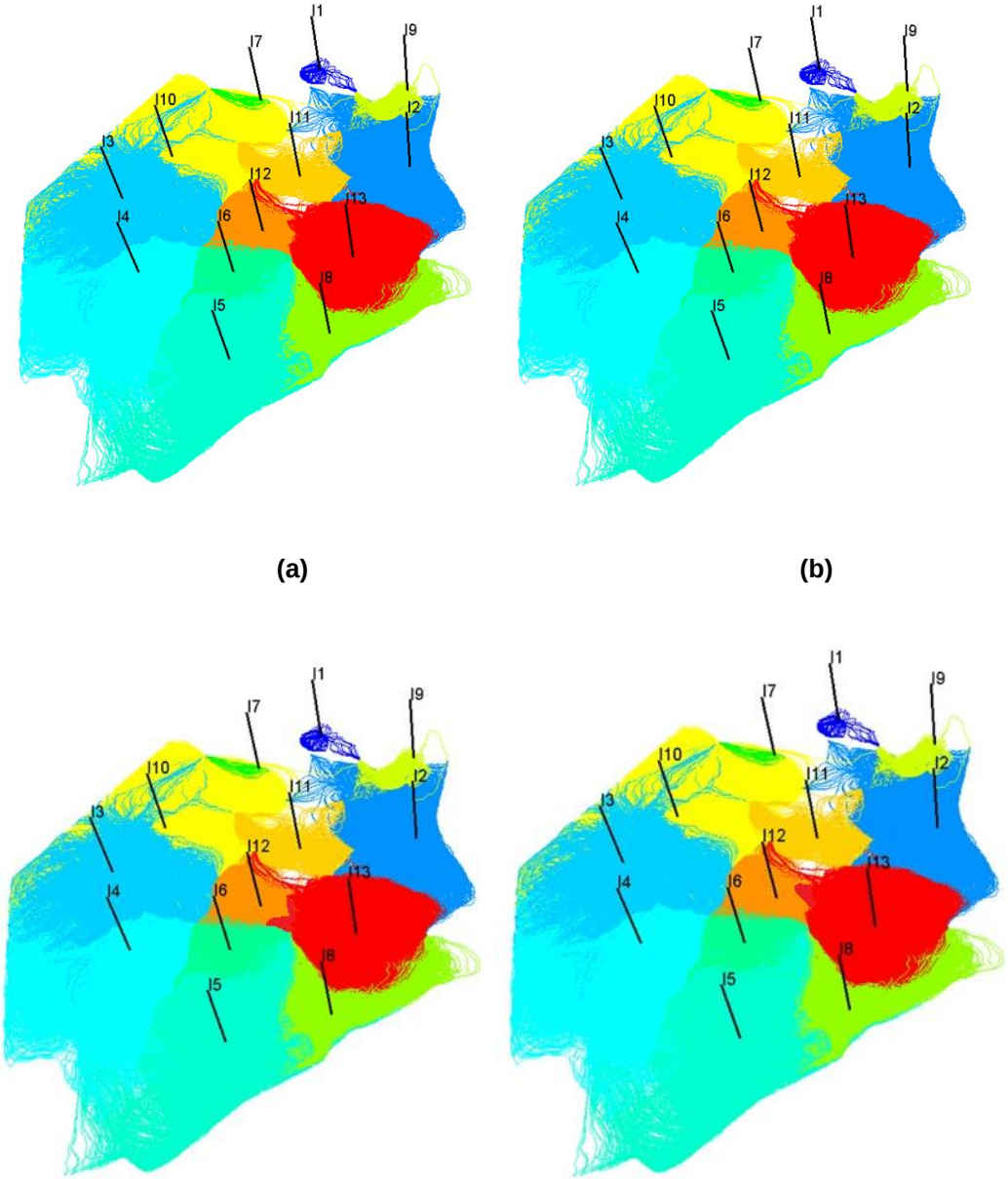

Figure 3.7 Validation of upscaling based on streamline partitions from injectors (a) Fine scale (b) 64 Layers (c) 52 Layers (d) 48 Layers

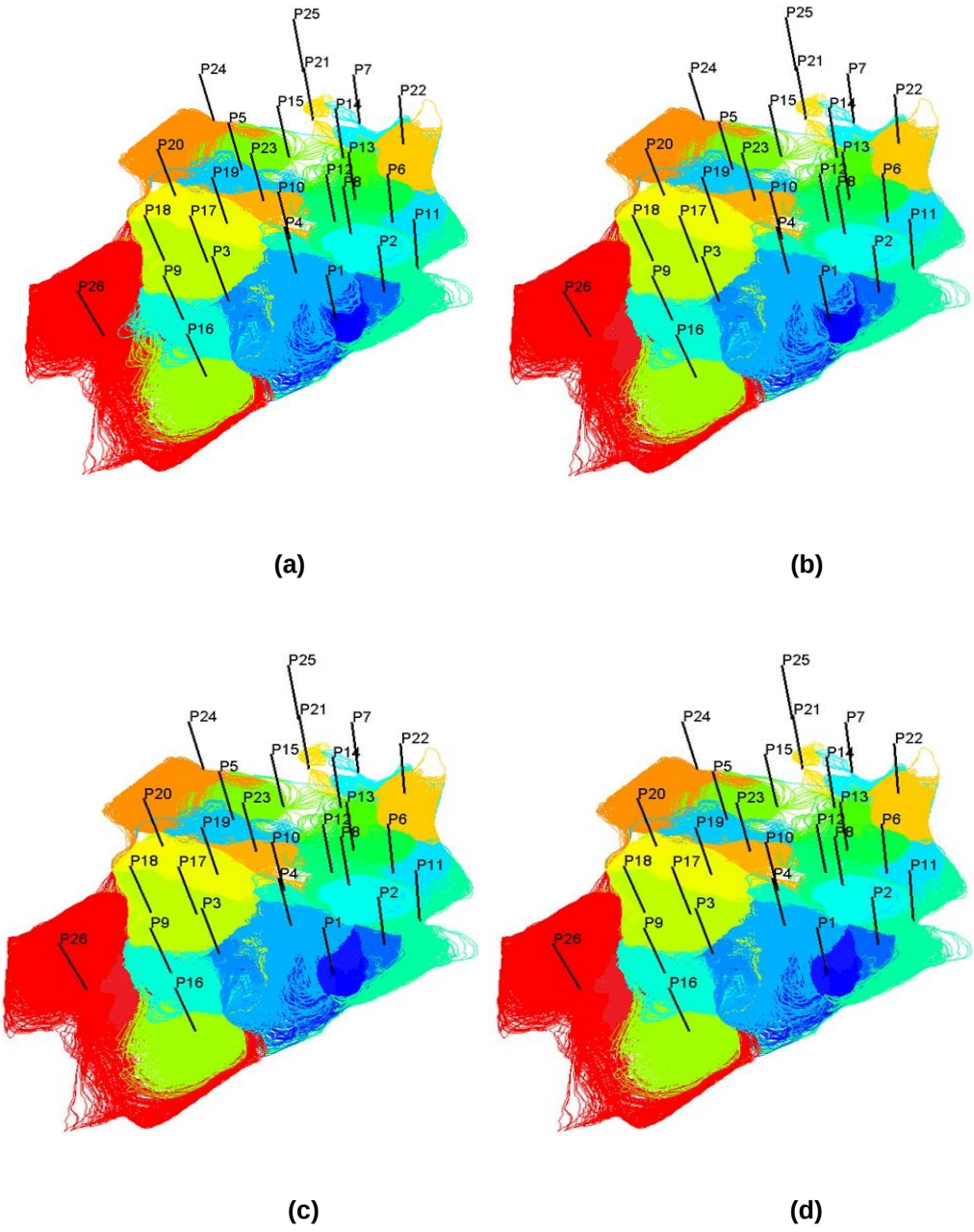

Figure 3.8 Validation of upscaling based on streamline partitions from producers (a) Fine scale (b) 64 Layers (c) 52 Layers (d) 48 Layers

Quality of our layer coarsening approach was checked by visual comparison (**Figure 3.2 – Figure 3.8**), which shows good matches between coarsened models and fine

scale model. As a result, we choose the 48 layers coarsening scheme, which reduces computational cost the most while preserving major heterogeneity and flow patterns. Areal coarsening was then conducted to further improve computational efficiency. Similarly, validation was conducted on coarsened models with different areal coarsening approaches. **Figure 3.9** and **Figure 3.10** shows the visual comparison of porosity field and permeability field between fine scale model and 2x2x48 and 3x3x48 coarsened model, which demonstrates good matches between fine scale model and coarsened models. Further validation from flow simulation results was showed in **Figure 3.11**, in terms of field water injection rate, field water production rate and field average pressure. Finally, computational costs between these models were compared and the results were shown in **Figure 3.12**. With our geologic model upscaling, we have successfully reduced more than 90% of the number of grid cells, which resulted in a computational speed up factor of 100 without significant loss of accuracy in flow response. The 3x3x48 upscaled model was then chosen for the model calibration process discussed in the next section.

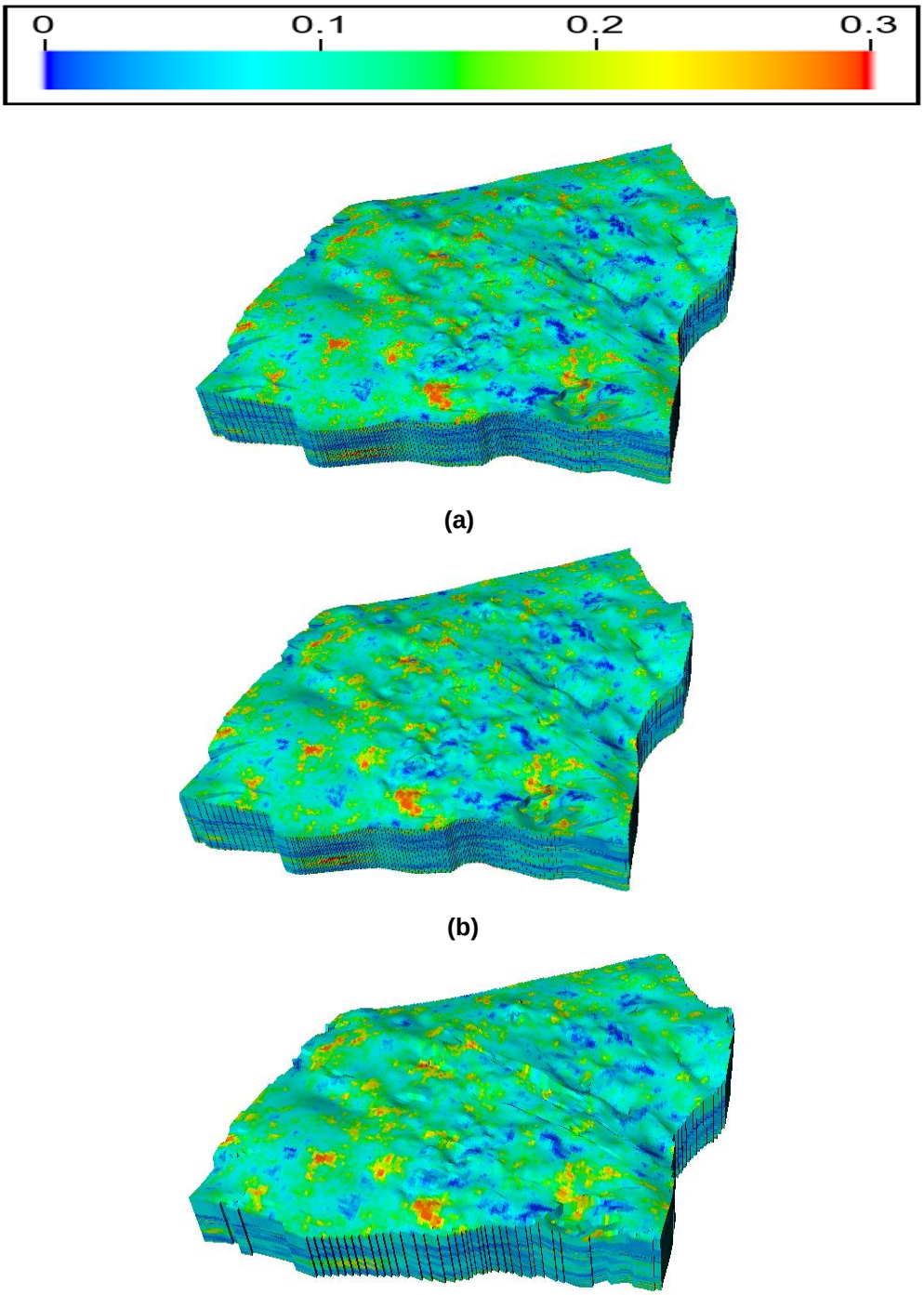

Figure 3.9 Comparison of upscaled porosity field (a) 1x1x48 (b) 2x2x48 (c) 3x3x48

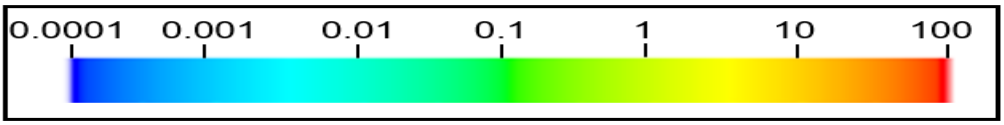

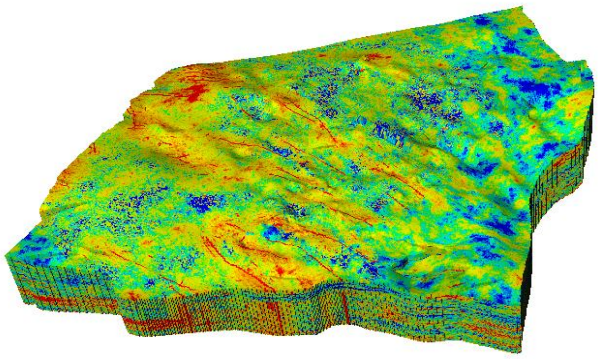

(a)

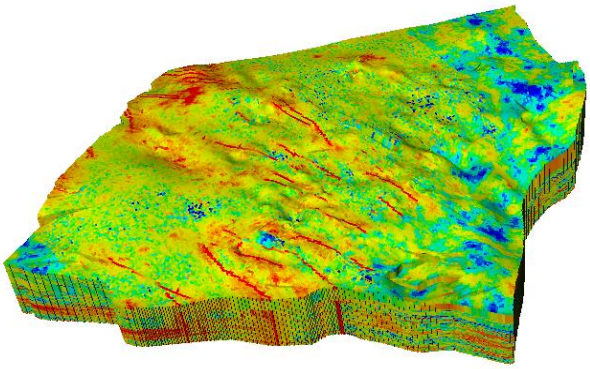

(b)

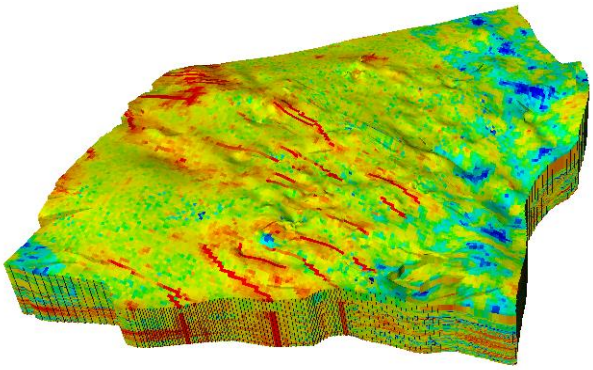

(c)

Figure 3.10 Comparison of upscaled permeability field (a) 1x1x48 (b) 2x2x48 (c) 3x3x48

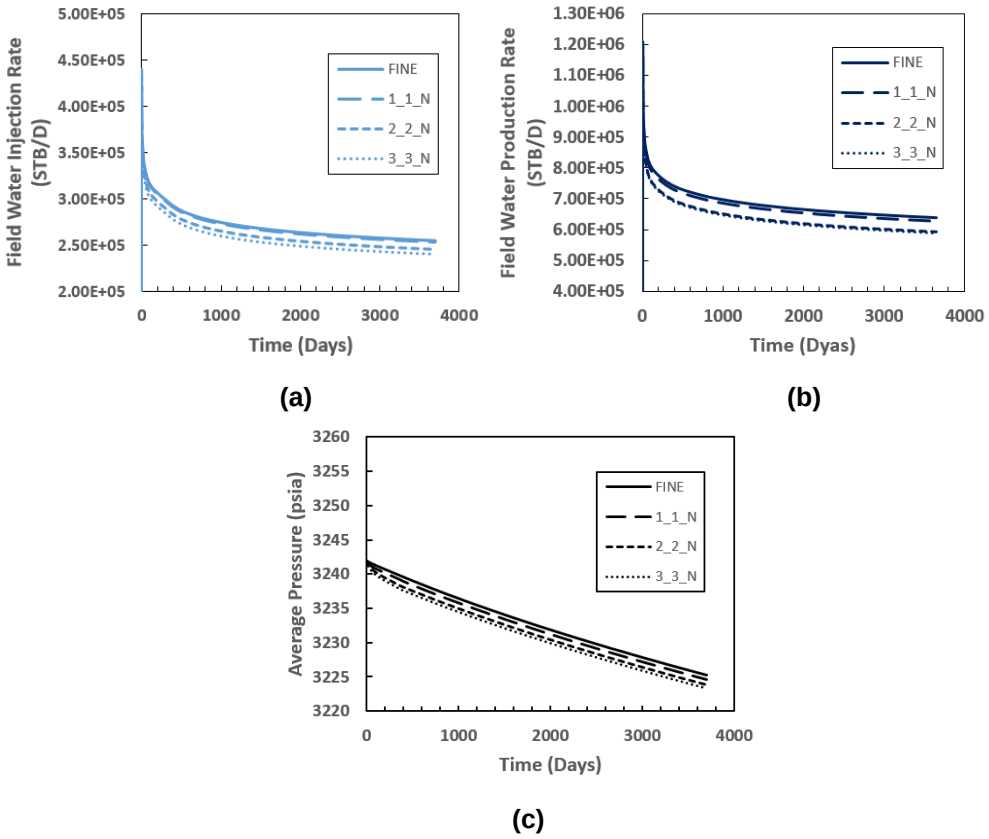

Figure 3.11 Geological model upscaling validation, comparing simulation responses between fine and coarse models based on (a) field water injection rate (b) field water production rate (c) field average pressure

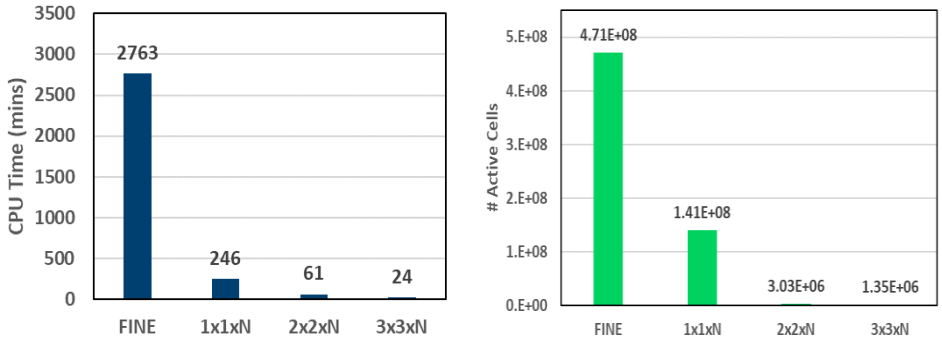

Figure 3.12 Comparison of (a) computational cost and (b) cell count between fine and coarse models

3.3 Streamline-based Model Calibration

Streamline-based history matching approach has proved to be effective and efficient to integrate various real-time data into high-resolution reservoir model, such as water cut data (Vasco et al. 1999; Cheng et al. 2006; Chen et al. 2019), bottom-hole pressure data (Tanaka et al. 2015), and time-lapse seismic data (Watanabe et al. 2017; Liu et al. 2020). **Figure 3.13** shows the streamline-based history matching workflow, in which we start with a given prior reservoir model and the history matching process proceeds in an iterative manner. During each iteration, data misfit of simulation results and observed data is checked. Streamlines are traced based on flux information from simulation results if data misfit is larger than the tolerance we set, and then model is updated based on the parameter sensitivities calculated along streamlines. This process is repeated until the data misfit is smaller than the tolerance or the maximum iteration number has been reached.

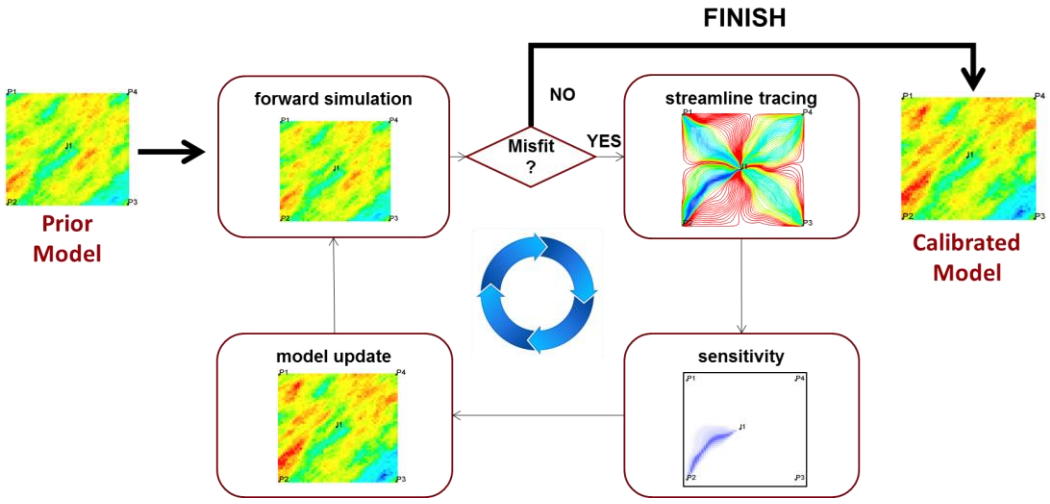

Figure 3.13 Streamline-based history matching workflow

Integration of dynamic data typically requires to solve an inverse problem to minimize the data misfit between the computed and observed response, during which a penalized misfit function is formed as follows:

$$\| \delta d - S\delta R \| + \beta_1 \| \delta R \| + \beta_2 \| L\delta R \| \tag{3.3}$$

where δd is the vector of data misfit, S is sensitivity matrix with respect to grid parameters, and δR corresponds to the change in reservoir properties. The second term, called the norm constraint, penalizes deviations from the prior model, which helps to preserve geologic realism. The third term is roughness penalty, which defines the model roughness to keep the change smooth and L is a second-spatial difference operator. An iterative least-square method is used to minimize the penalized misfit function (**Equation 3.3**).

The main parameter of inversion problem is sensitivity matrix and the advantage of streamline-based inversion method is the analytically calculated sensitivity matrix. In this study, we used bottom-hole pressure (BHP) data to calibrate the model and the illustration of the formulation of sensitivity of BHP to permeability is showed in **Figure 3.14**. The bottom-hole pressure sensitivity estimated by a single streamline segment within grid block i is given as:

$$sens_i^{p,s\ln} = \frac{\partial BHP_i^{s\ln}}{\partial k_i} = -\frac{\partial \Delta P_i^{s\ln}}{\partial k_i} = \frac{\Delta P_i^{s\ln} - \overline{\rho}_i g \Delta D_i}{k_i} \tag{3.4}$$

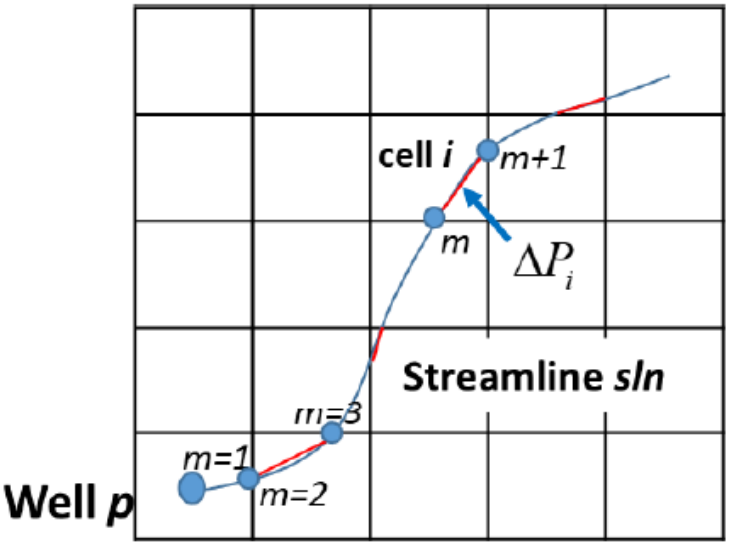

Figure 3.14 Illustration of sensitivity calculation

In this study, BHP data of 104 injectors were used to calibrate the coarsened model using streamline-based method and the history matching quality is demonstrated in **Figure 3.15**, which is the normalized data misfit vs. number of iterations. From this figure, we could see that the BHP misfit was reduced by 80% within 10 iterations and the inversion

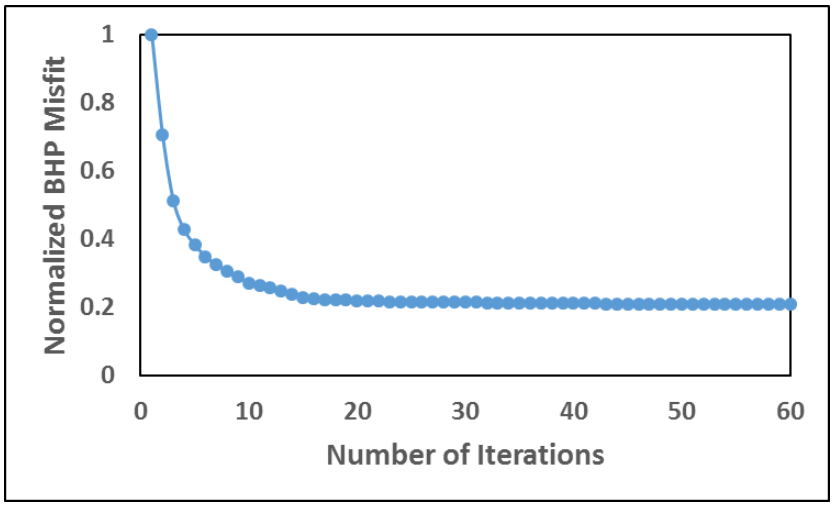

Figure 3.15 Normalized data misfit vs. number of iterations

was stabilized after that. **Figure 3.16** shows some of the well response shift after calibration, where the black dots are observed BHP converted from THP (Appendix A),

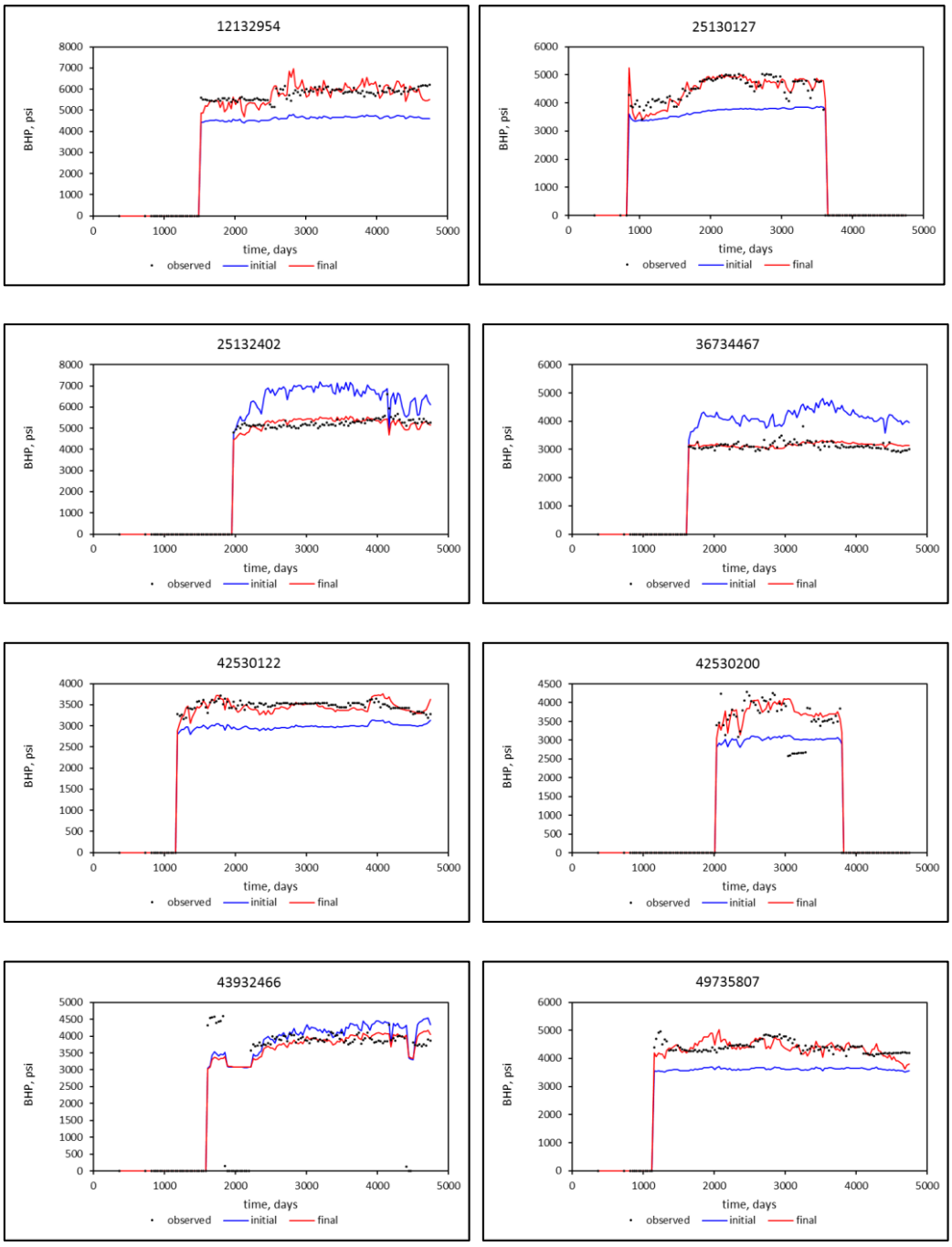

Figure 3.16 Well response shift after calibration

blue lines are simulated BHP from the initial model and red lines are simulated BHP from the calibrated model. We could see that after calibration, the simulation results match well with the observed data.

Since bottom-hole pressure is highly sensitive to near-wellbore property, permeability change during history matching tend to focus in the grid cells near wellbore. To solve this problem, we used a sensitivity smoothing method to regularize the inversion problem and ensure large scale geologic continuity over localized permeability changes. **Figure 3.17** shows the basic illustration of the sensitivity smoothing method. When we calculate the sensitivity for one grid cell, we will first define a search window and the extension of the search window depends on the degree of smoothness you would like to add into sensitivity calculation. The sensitivity for each cell is the average of sensitivity in its search window. **Figure 3.18** shows the permeability change in different layers after calibration. We could see that the permeability change is large scale so that the original geologic feature could be preserved during history matching process.

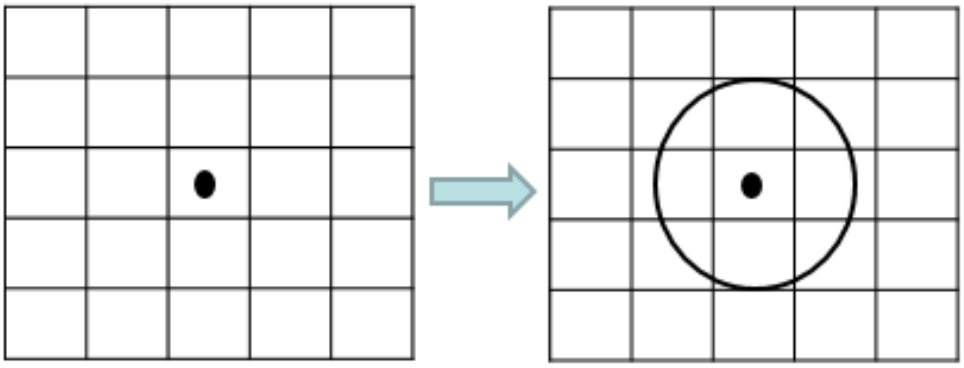

Figure 3.17 Illustration of sensitivity smoothing method

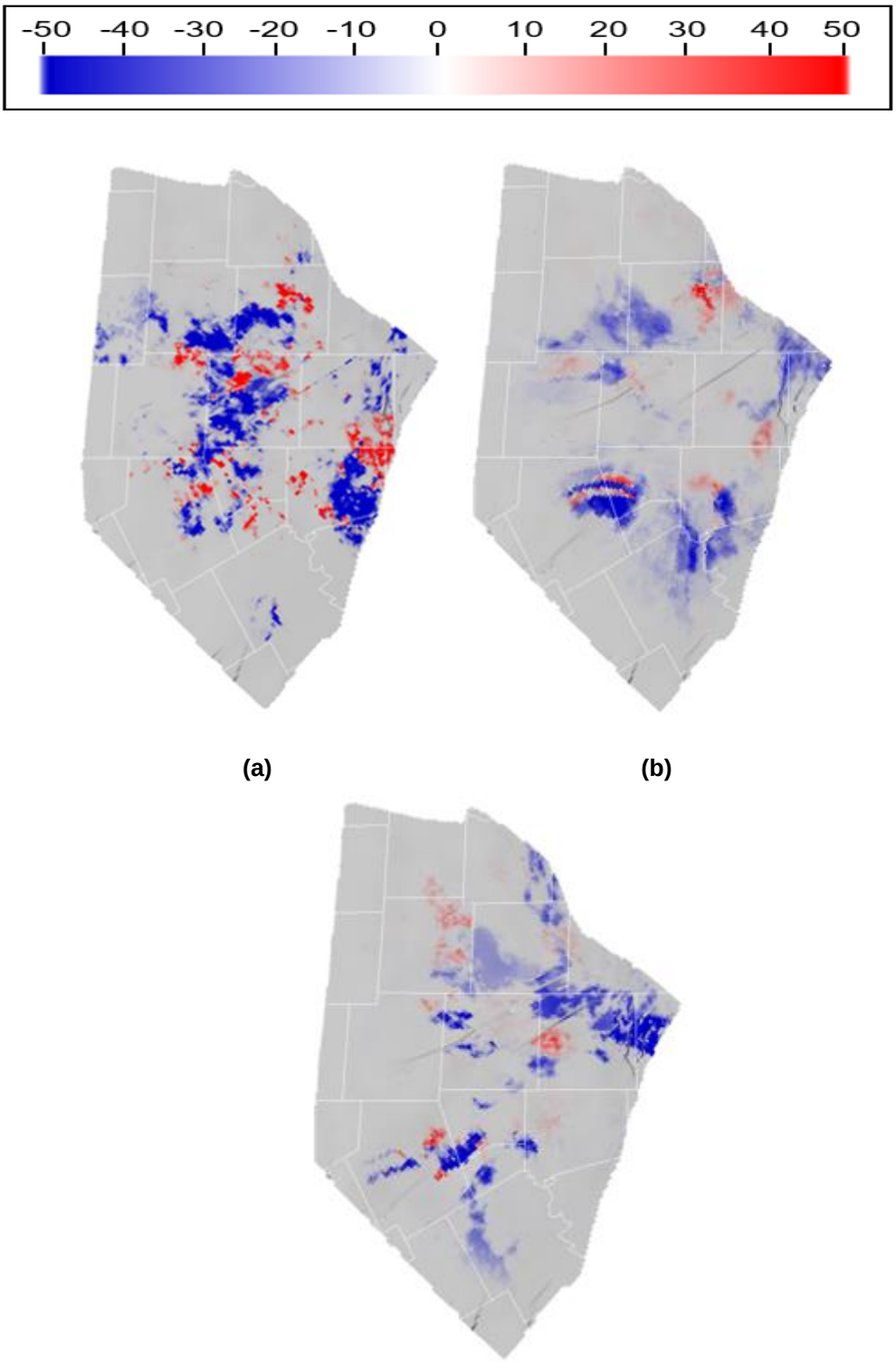

Figure 3.18 Permeability change after calibration in different layers

Figure 3.19 shows the comparison of flow partition visualized by 3D streamline of the initial model and the updated model, in which streamlines from different injectors are assigned different color. Since the inversion is designed to preserve the prior geologic model, we could see only small changes in the flow patterns after history matching.

3.4 Summary

In this Chapter, we discussed the model upscaling and calibration. For model upscaling, we use a combination of areal coarsening and layer coarsening. For vertical coarsening, we adopted a recursive sequential coarsening method, while for areal coarsening, we used a simple structural upgridding. Validation test was conducted on the coarsened model to validate the upscaling quality, including visual comparison of permeability field and porosity field, streamline TOF and streamline flow partition. The final upscaling scheme we chose was 3x3xN and the coarsened model had similar simulation results with the fine scale model. After upscaling, , we have successfully reduced more than 90% of the number of grid cells, which resulted in a computational speed up factor of 100 without significant loss of accuracy in flow response. Streamline-based method was then used to calibrate the coarsened model to BHP of 104 injectors and sensitivity smoothing method was used to keep the original geologic feature.

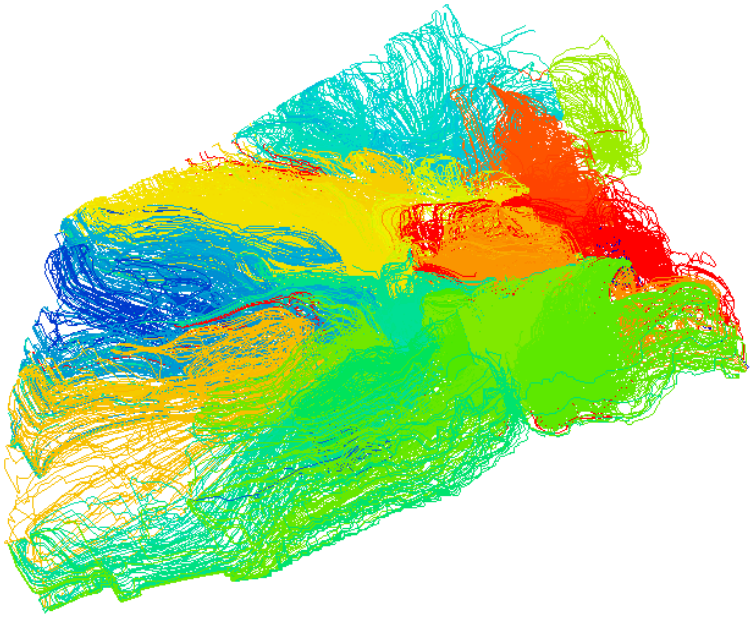

(a)

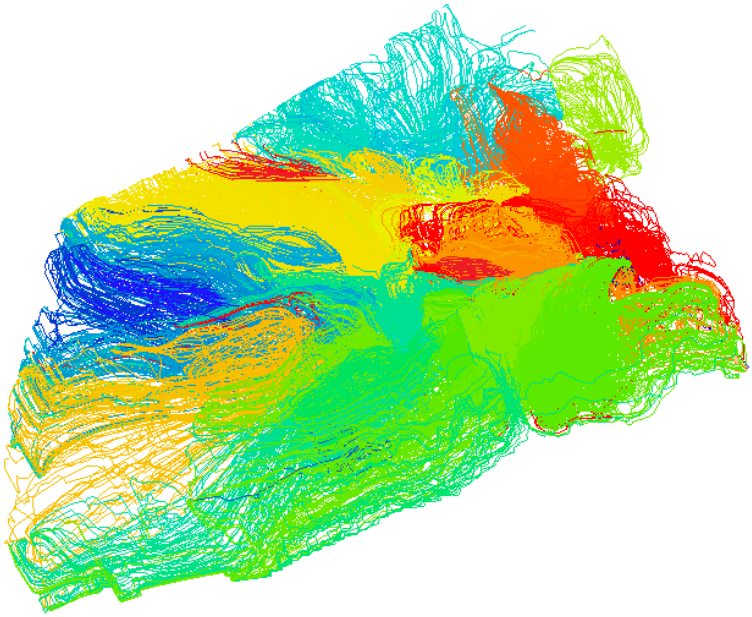

(b)

Figure 3.19 Flow pattern visualization of (a) initial model (b) updated model

CHAPTER IV

PORE PRESSURE AND FAULT SLIP POTENTIAL ANALYSIS

4.1 Introduction

There are five earthquake sequences that occurred in Fort Worth Basin, which are DFW Airport Earthquake, Cleburne Earthquake, Azle Earthquake, Irving Earthquake and Venus earthquake. These sequences are highlighted by different color circles in **Figure 4.1**. The first sequence is the Dallas Fort-Worth (DFW) Airport marked by the red circle. The DFW Airport earthquake occurred in November 2008 and was the first earthquake known in the DFW metropolitan area in historical times (Frohlich et al. 2016). Previous study (Frohlich et al. 2011) preformed a spatial and temporal correlation study between the earthquakes and wastewater injection and concluded that it is likely that the DFW Airport earthquake sequence was induced by fluid injection.

The second sequence is Cleburne Earthquake which occurred between June and August 2012 and is marked by the yellow circle. Previous study (Justinic et al. 2013), similar to the study performed by Frohlich et al. (2011), performed spatial and temporal correlation between earthquakes and wastewater injection, and concluded that the earthquake was also likely to have been induced by fluid injection.

The third sequence is Azle Earthquake, which occurred between November 2013 and January 2014, and is marked by green circle. Different from the other sequences, Azle earthquake was likely induced by not only wastewater injection, but also oil and

gas production activities that occurred adjacent to a fault in the region (Hornbach et al. 2015; Chen et al. 2018).

The fourth sequence is Irving Earthquake, which occurred in 2014, and is marked by red circle. Previous study (Hornbach et al. 2016; Zhai et al. 2018) indicated that the Irving sequence may be triggered by pore pressure increase due to wastewater injection activities.

The fifth sequence is Venus Earthquake, which occurred in May 2015, and is marked by blue circle. Previous study (Scales et al. 2017) suggested a likelihood of pore pressure increase due to wastewater disposal inducing the earthquake on the causative fault.

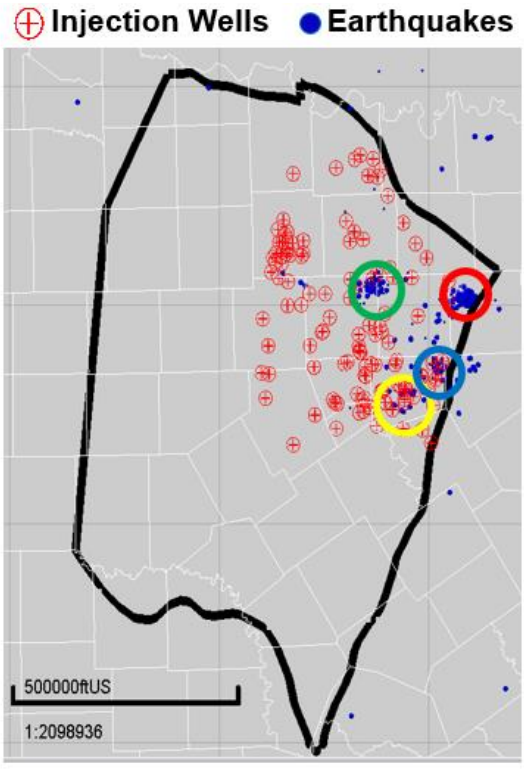

Figure 4.1 Location map of earthquake sequences

In this study, a fluid flow simulation was conducted on a calibrated model of Fort Worth Basin with a simulation period of 20 years (2006~2025). Pore pressure analysis based on the simulation results and fault slip potential analysis are presented in the following sections.

4.2 Pore Pressure Analysis

In this section, pore pressure change from simulation results were used to find time and spatial correlation between earthquake events and wastewater disposal and oil & gas production activities to understand the controlling mechanism of the induced seismic events in Fort Worth Basin.

4.2.1 Impact of Gas Production

Different from previous study (Gono et al. 2015; Hornbach et al. 2016; Zhai et al. 2018), this study is the first basin-wide study including gas production in the fluid flow modeling process. Although typically ignored, hydrocarbon gas production can contribute to greater reservoir depletion compared to brine production. The brine is produced from the Ellenburger formation because the hydraulic fractures propagate through the Barnett into the Ellenburger formation (Hornbach et al. 2015). Especially in regions where the Viola Simpson is absent above the Ellenburger, the producers in the Barnett are in direct pressure communication with the Ellenburger formation. According to **Figure 4.2**, among five earthquake sequences, only Azle and Cleburne area do not have overlying Viola Simpson. Our results show that ignoring the gas production leads

to significant under-estimation of the reservoir fluid withdrawal and reservoir pressure depletion. We converted the surface gas production to bottom-hole conditions and used the equivalent reservoir fluid withdrawal rates (Appendix B). **Figure 4.3** shows the comparison of cumulative water production, gas production and the total fluid withdrawal under reservoir conditions, from which we could see that the combination of gas production and water production is four times larger than water production only.

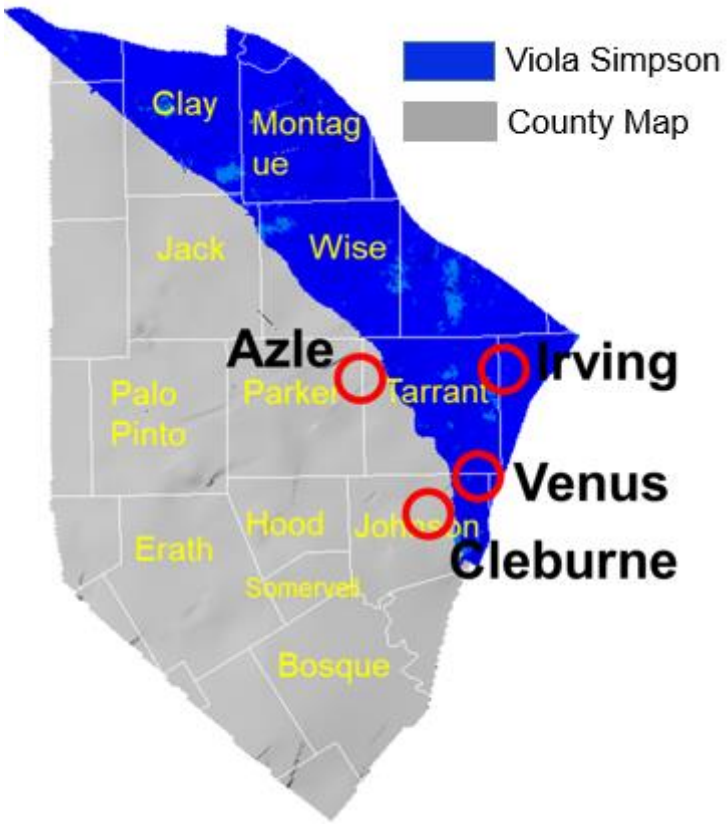

Figure 4.2 County map superimposed with the permeability distribution of Viola Simpson

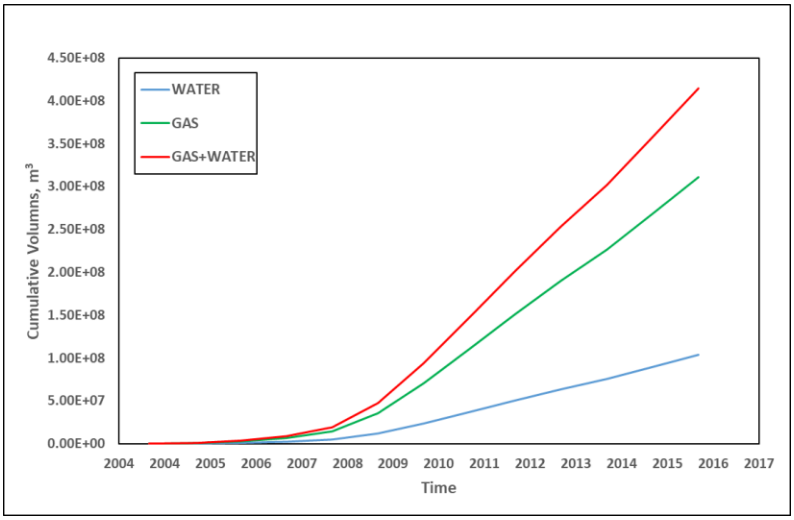

Figure 4.3 Produced fluid volumes used in this study (reservoir conditions)

Figure 4.4 shows the comparison of pore pressure change map in different years between the case with water production only and the case with a combination of water production and gas production. According to **Figure 4.4**, including gas production could reduce the degree of pore pressure increase and even cause pore pressure decrease in certain area (Azle area), which proves that hydrocarbon gas production does have an impact on pore pressure in the reservoir, especially in areas that do not have overlying Viola Simpson formation (Azle and Cleburne area), where Ellenburger formation and Barnett formation are in direct pressure communication.

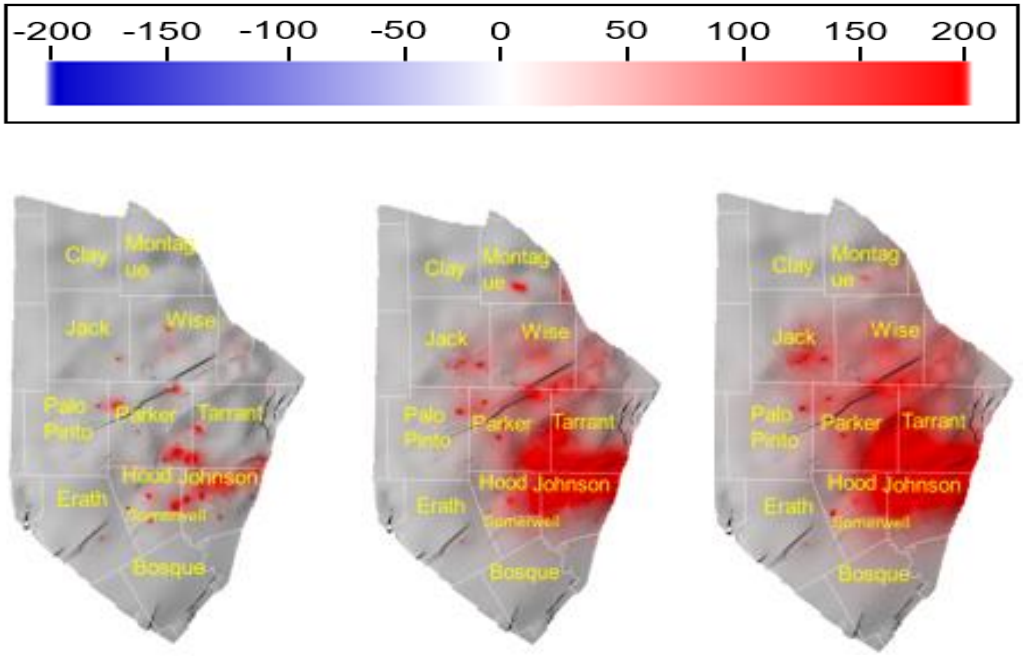

(a)

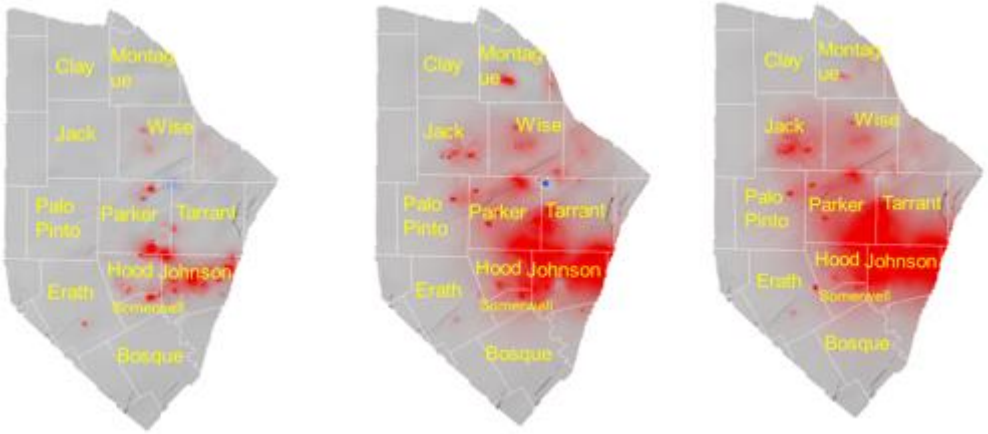

(b)

Figure 4.4 Comparison of pore pressure change map in different years between (a) case with water production only (b) case with gas and water production

4.2.2 Dallas Fort Worth (DFW) Airport Earthquakes

The Dallas Fort Worth (DFW) Airport earthquake sequence began in October 2008 and continued until May 2009. In this study, pore pressure change at the time of onset of seismic events is of interest. **Figure 4.5(a)** shows the pore pressure change map at the last layer of Ellenburger on 1 November 2008, which is the end date of the first DFW airport earthquake swarm. From **Figure 4.5(a)**, we could see that there are some areas of pore pressure increase in the vicinity of the earthquakes. **Figure 4.5 (b)** is the zoom-in pore pressure change map in the area of interest marked by the yellow circle in **Figure 4.5(a)**. According to **Figure 4.5 (b)**, two wastewater disposal wells located in DFW Airport area, denoted by two white circles and named by "North Well" and "South Well" based on their locations. We could also identify the two areas of pore pressure

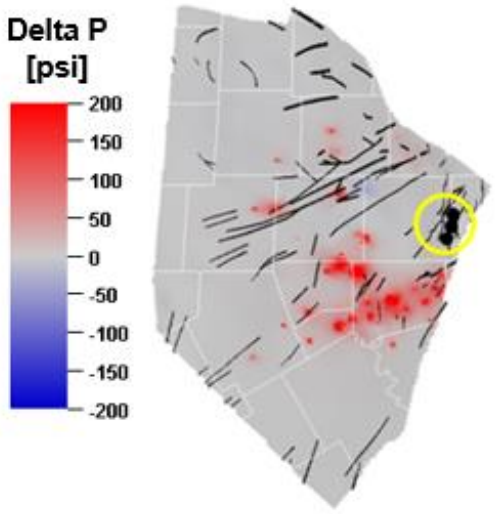

(a)

Figure 4.5 (a) Pore pressure change map in 2008 superimposed with DFW Airport Earthquake (b) zoom-in pore pressure change map in DFW Airport area

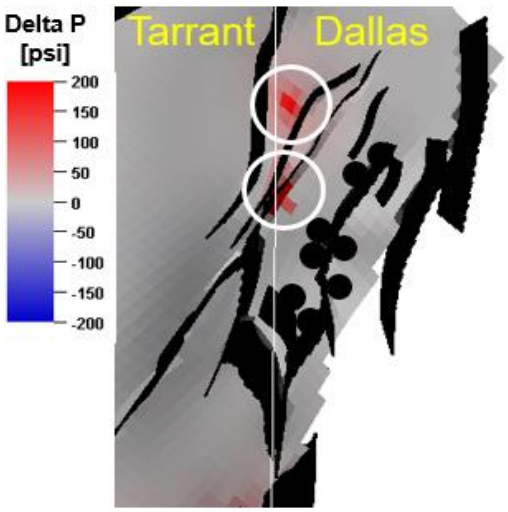

(b)

Figure 4.5 cont.

Table 4.1 Well information of two injectors in DFW Airport Area

	API (8 digit)	Total Volume Injected (10^3BBLS)	Injection Start Time	Injection End Time
"North Well"	43932003	13694.22	Nov-2007	Still Active
"South Well"	43932673	315.83	Sep-2008	Aug-2009

increase of a magnitude of 50 psi due to the injection activities of these two wells, the information of which is shown in **Table 4.1** and injection schedule in **Figure 4.6**. Since the "South Well" located closer to DFW Airport earthquakes, we will focus more on the "South Well". According to **Figure 4.6**, the "South Well" started injection in September 2008 and stopped after August 2009. As we mentioned earlier, the DFW Airport

earthquake occurred one month after wastewater injection into the Ellenburger formation commenced, which strongly suggests that there is a temporal correlation between the DFW Airport earthquake and wastewater injection.

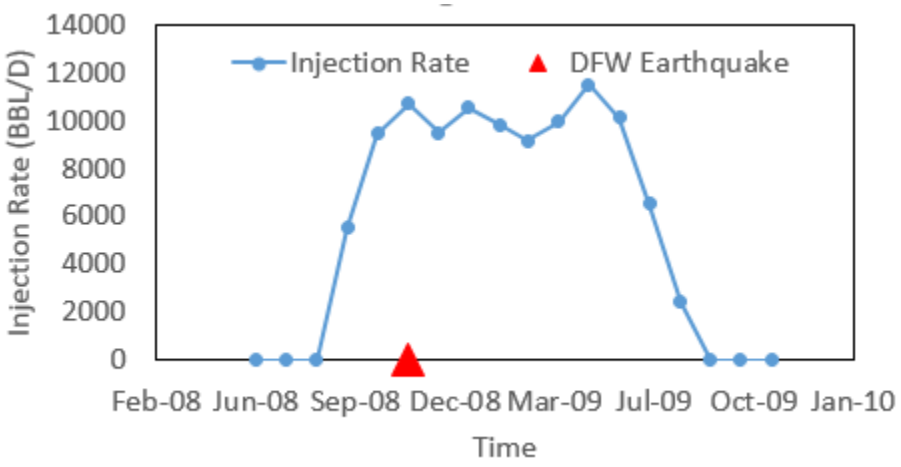

Figure 4.6 "South Well" monthly Injection Schedule

In conclusion, for DFW Airport earthquake, we could see that there is a strong spatial and temporal correlation between seismic events and area of increased pore pressure of a magnitude of 50 psi.

4.2.3 Cleburne Earthquake

Cleburne earthquake occurred in August 2012 and the pore pressure change map of the last layer of Ellenburger at the onset time of earthquake events is shown in **Figure 4.7(a)** and **Figure 4.7(b)** is the zoom-in pore pressure change map in the area of interest. From Figure 4.7, we could identify spatial correlation between pore pressure increase with a magnitude of 100 psi and seismic events in Cleburne area.

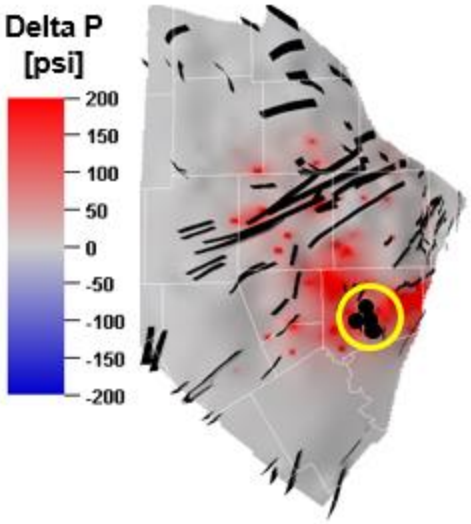

(a)

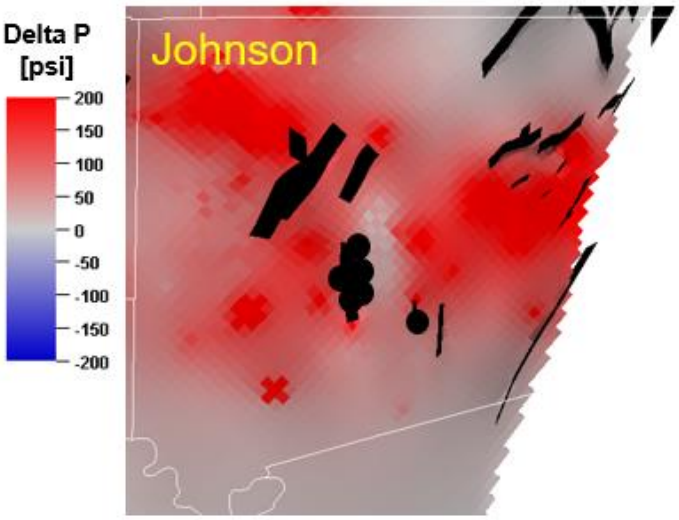

(b)

Figure 4.7 (a) Pore pressure change map in 2010 superimposed with Cleburne Earthquake (b) zoom-in pore pressure change map in Cleburne area

4.2.4 Azle Earthquake

Azle earthquake occurred in 2013 and the pore pressure change map of the last layer of Ellenburger at the onset time of earthquake events is shown in **Figure 4.8(a)** and **Figure 4.8(b)** is the zoom-in pore pressure change map in the area of interest. Different from other earthquake sequences in Fort Worth Basin, we could identify pore pressure decrease in Azle area due to hydrocarbon gas production from overlying Barnett formation and there exists a pressure imbalance between two sides of the fault that caused the Azle earthquake (**Figure 4.8(b)**). In the side where two injectors located, there was pore pressure increase with a magnitude of 50 psi; in the other side, where were no injectors but producers only, pore pressure decreased with a magnitude of 150 psi. So there was a pore pressure imbalance of around 200 psi between two sides of the fault, which may have caused an unbalanced loading on the fault and resulted in the onset of the seismic events. This special phenomenon indicated that Azle earthquake may have different controlling mechanism than other earthquake sequences. In order to further investigate pressure imbalance and unbalanced loading, a site-specific study of Azle area was conducted and will be introduced in section 4.4.

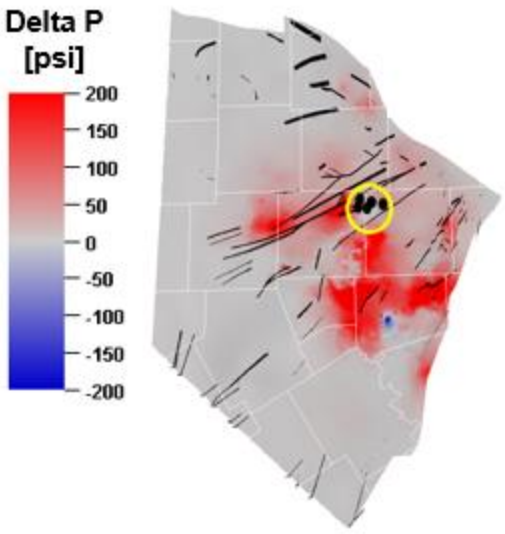

(a)

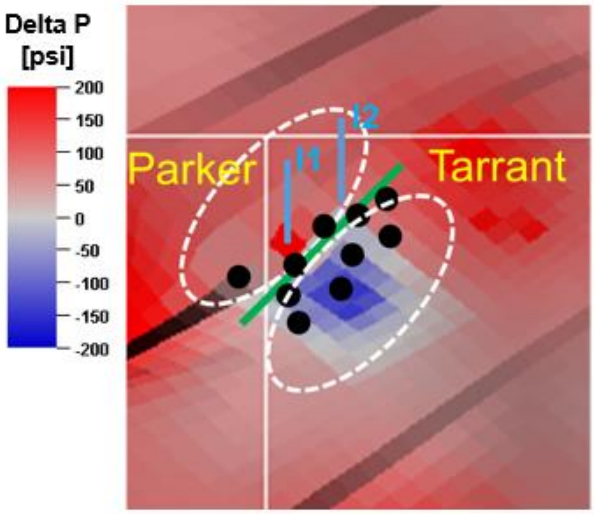

(b)

Figure 4.8 (a) Pore pressure change map in 2013 superimposed with Azle Earthquake (b) zoom-in pore pressure change map in Azle area

4.2.5 Irving Earthquake

Irving earthquake sequence started in October 2014 and the pore pressure change map of the last layer of Ellenburger at the onset time of earthquake events is showed in **Figure 4.10(a)** and **Figure 4.10(b)** is the zoom-in pore pressure change map in the area of interest. Since Irving earthquake occurred in the same area as DFW Airport earthquake, it's worthwhile to analyze the temporal correlation between seismic events and the schedule of wastewater disposal well in that area. As we mentioned in earlier section, there were two wastewater disposal wells in DFW Airport and Irving area (**Figure 4.5 (b)**). According to the well schedule showed in **Table 4.1**, only the "North Well" was active at the time of seismic events. From **Figure 4.9**, which is the injection rate schedule of the "North Well", we could see that, although operator reduced the injection rate gradually, seismic events were still initiated. It is then worthwhile to conduct fluid flow simulation to analyze pore pressure change to understand the controlling mechanism and evaluate risk associated with injection activities. From the pore pressure change of our fluid flow simulation results, consistent with previous study (Hornbach et al. 2016; Zhai et al. 2018), we also identified pore pressure increase in Irving area, with a magnitude of 150 psi.

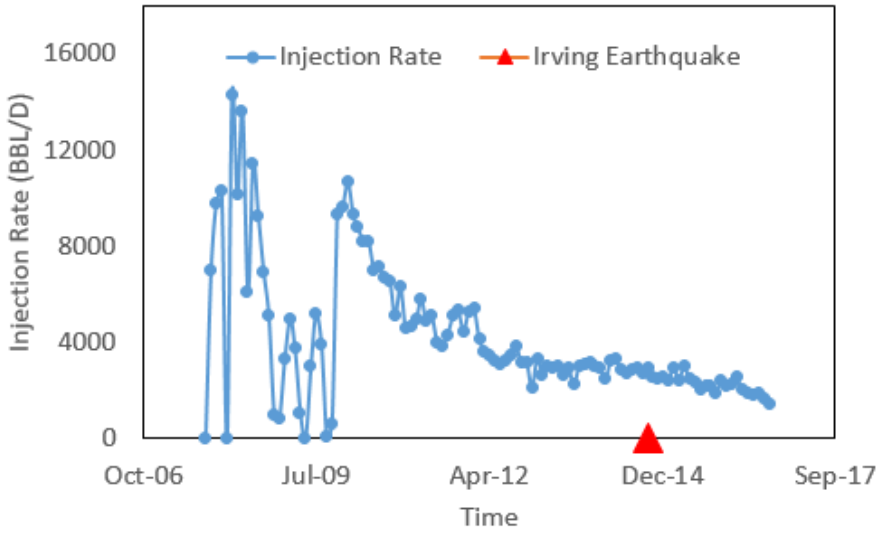

Figure 4.9 "North Well" monthly Injection Schedule

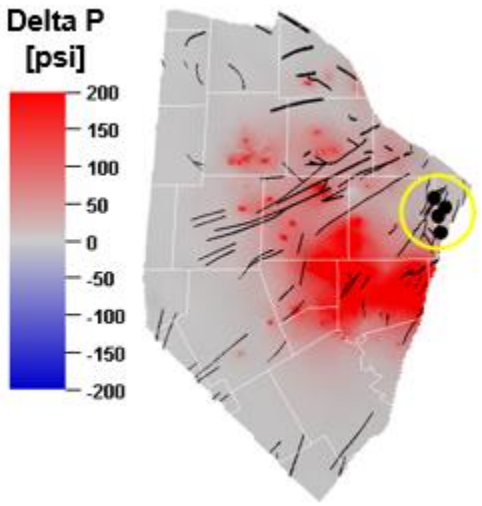

(a)

Figure 4.10 (a) Pore pressure change map in 2014 superimposed with Irving Earthquake (b) zoom-in pore pressure change map in Irving area

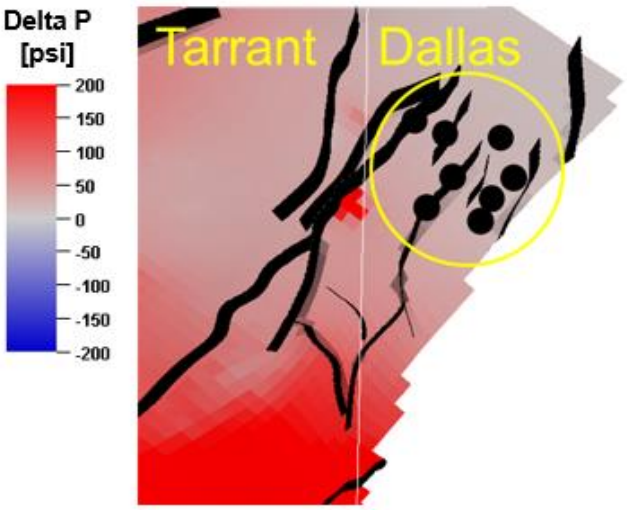

(b)

Figure 4.10 cont.

4.2.6 Venus Earthquake

Venus earthquake occurred in 2015 and the pore pressure change map of the last layer of Ellenburger at the onset time of earthquake events is showed in **Figure 4.11(a)** and **Figure 4.11(b)** is the zoom-in pore pressure change map in the area of interest. We also identified pore pressure increase in Venus area, with a magnitude of 200 psi.

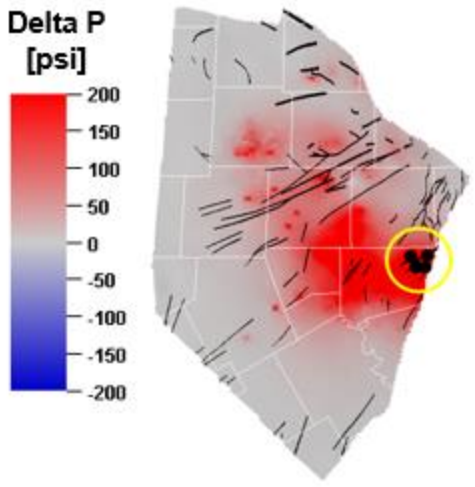

(a)

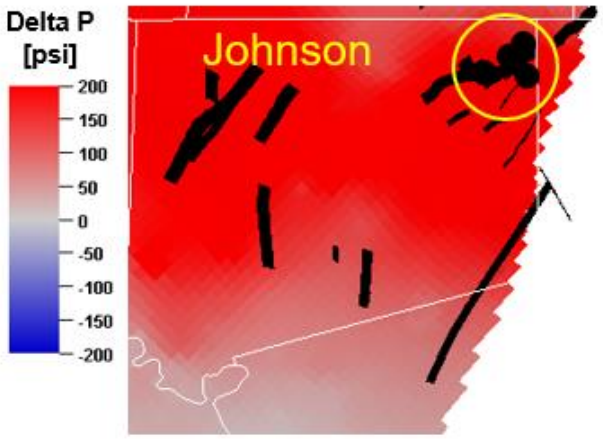

(b)

Figure 4.11 (a) Pore pressure change map in 2015 superimposed with Venus Earthquake (b) zoom-in pore pressure change map in Venus area

4.3 Fault Slip Potential Analysis

In this section, fault slip potential (FSP) was calculated and summarized for the whole Fort Worth Basin in different times to understand the controlling mechanism of earthquake sequences in the Fort Worth Basin.

FSP calculates the probability that planar fault segments will be critically stressed with the ambient stress field at a modeled pore pressure. FSP uses a linearized Mohr-Coulomb failure criterion for faults within the specified stress field and pore-pressure conditions, with critically stressed conditions occurring when the ratio of resolved shear stress to normal stress reaches or exceeds the failure envelope. Uncertainties are associated with all input parameters including the fault strike and dip, ambient stress field, fault properties, and initial fluid pressure. Our FSP calculation method utilizes Monte Carlo-type analysis to randomly sample values of each input parameter from specified, uniform uncertainty distributions (**Table 4.2, Table 4.3**) (Hennings et al. 2019). **Figure 4.12** shows the fault framework model we used and the partition of stress areas with different stress state. The details of steps of FSP calculation is showed in **Appendix C**.

In this analysis, we estimated FSP based on the pore pressure from the simulation results of our calibrated fluid flow model at the onset time of the seismic events (2008, 2010, 2013, 2014 and 2015) and also the hydrostatic initial state (**Appendix C**). Then the FSP change maps, which were calculated by subtracting FSP map at different times by the initial FSP, were used to analyze how FSP would change due to wastewater injection and oil & gas production activities.

Table 4.2 Input Parameters for FSP Calculation

Stress Area	Northwest Latitude (°)	Northwest Longitude (°)	Southeast Latitude (°)	Southeast Longitude (°)	$S_{H\,max}$ Azimuth (°)	$S_{H\,max}$ Azimuth Unc (°)	$A\phi$	$A\phi$ Unc
1	34.20	-99.00	33.25	-97.00	38	20	1.18	0.3
2	33.25	-98.80	32.10	-97.40	32	16	1.00	0.22
3	33.25	-97.40	32.10	-96.40	25	15	0.80	0.21
4	32.10	-99.40	30.70	-97.20	45	20	0.82	0.15

Table 4.2 cont.

Cohesion	Fault μ	Fault μ Unc	Initial Pp (psi/ft)	Initial Pp Unc (psi/ft)	Sv (psi/ft)	Sv Unc (psi/ft)	Fault-Strike Unc (°)	Fault-Dip Unc (°)
0	0.7	0.05	0.45	0.05	1.15	0.05	5	10
0	0.7	0.05	0.45	0.05	1.15	0.05	5	10
0	0.7	0.05	0.45	0.05	1.15	0.05	5	10
0	0.7	0.05	0.45	0.05	1.15	0.05	5	10

Table 4.3 Stress Gradients in Fort Worth Basin

Stress Area	SV (MPa/km)	$S_{h\,max}$ (MPa/km)	$S_{h\,min}$ (MPa/km)
1	26.01	28.46	14.86
2	26.01	26.01	14.20
3	26.01	23.65	14.20
4	26.01	23.89	14.20

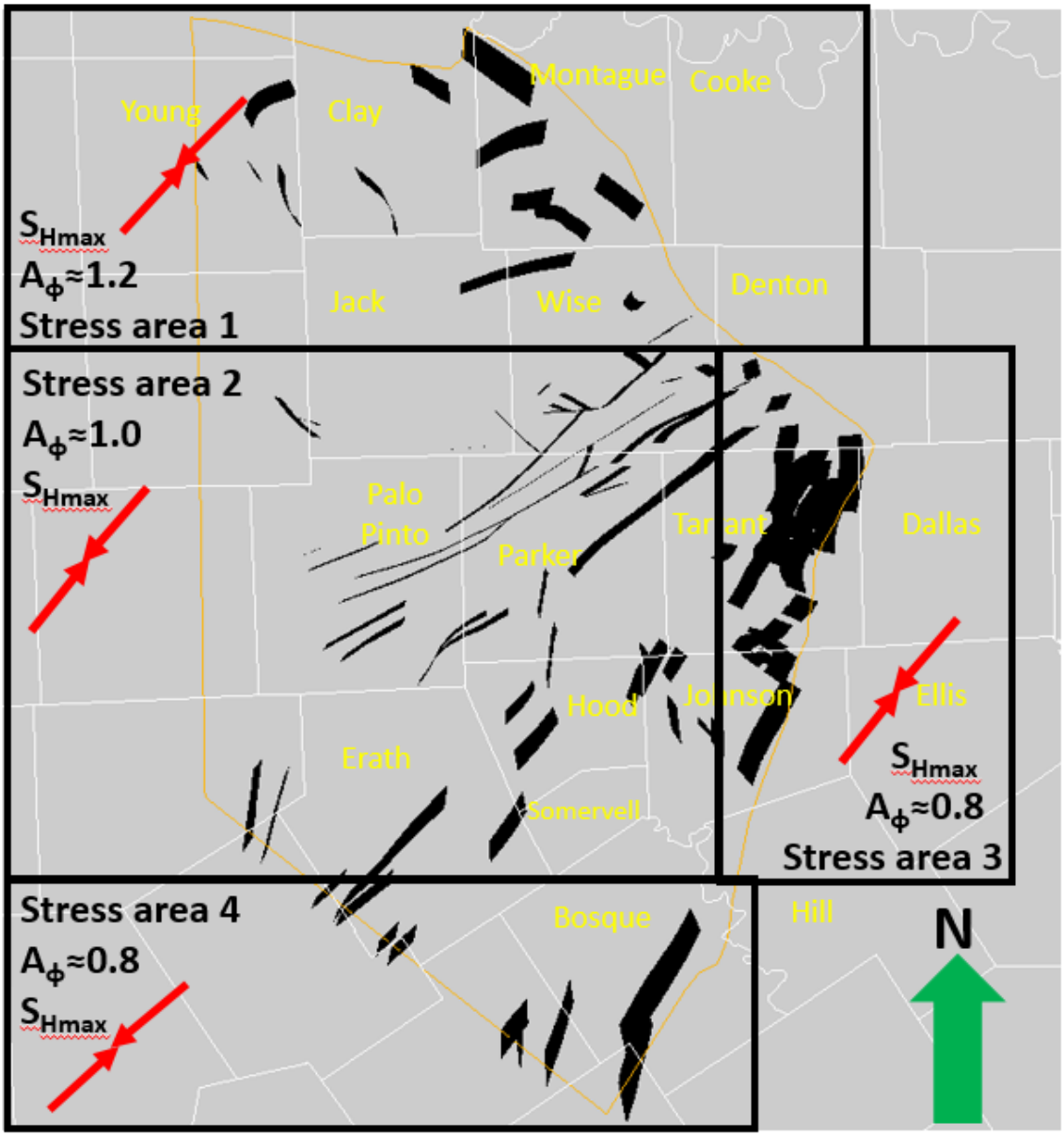

Figure 4.12 Fault framework model and partition of stress area

Figure 4.13 shows the FSP change at 2008 with the inlet study area, denoted by the dotted black box, where DFW Airport earthquake occurred and **Figure 4.14** shows the histograms of three cases: (1) FSP change of faults segments in DFW Airport area at 2008; (2) FSP change of faults segments in Fort Worth Basin excludes study area at 2008; (3)

FSP change of faults that held the DFW Airport earthquake. From **Figure 4.11**, we could see that at 2008, FSP change of Fort Worth Basin ranges from 0 to 0.1 and DFW Airport area, denoted by the dotted black box, has the highest FSP change values. We could draw the same conclusion from the comparison of histogram of three different cases shown in **Figure 4.13**, where the mean FSP change of DFW Airport area is 0.05, five times higher than the average FSP change of other areas of Fort Worth Basin. From our fluid flow modeling results, pore pressure increase at DFW Airport area at the onset time of seismic events was only 50 psi, which means that the fault could slip with a relatively small amount

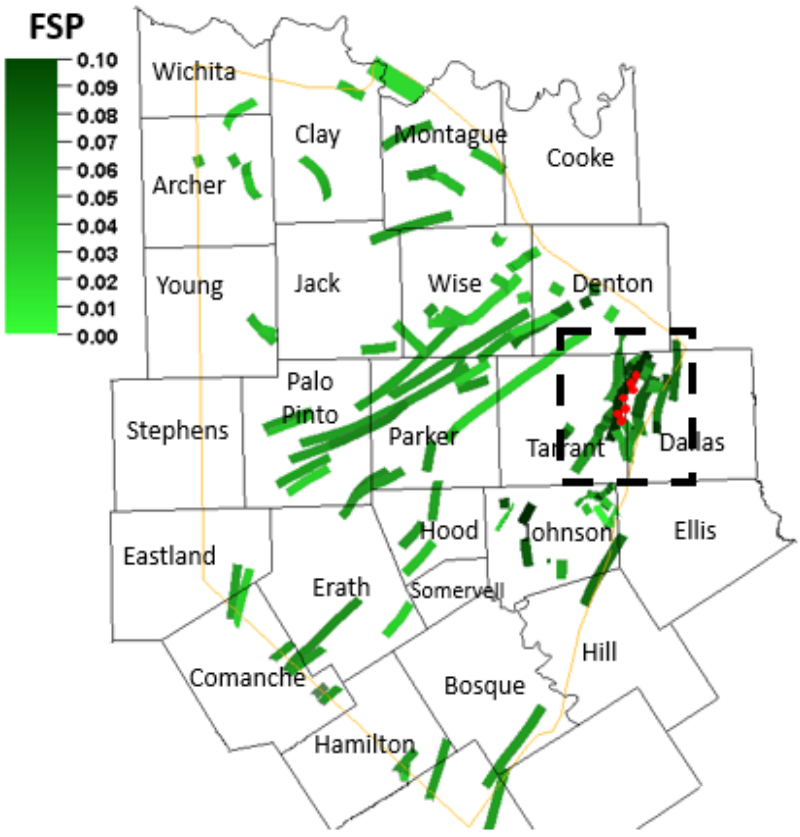

Figure 4.13 Fault slip potential change of Fort Worth Basin at 2008

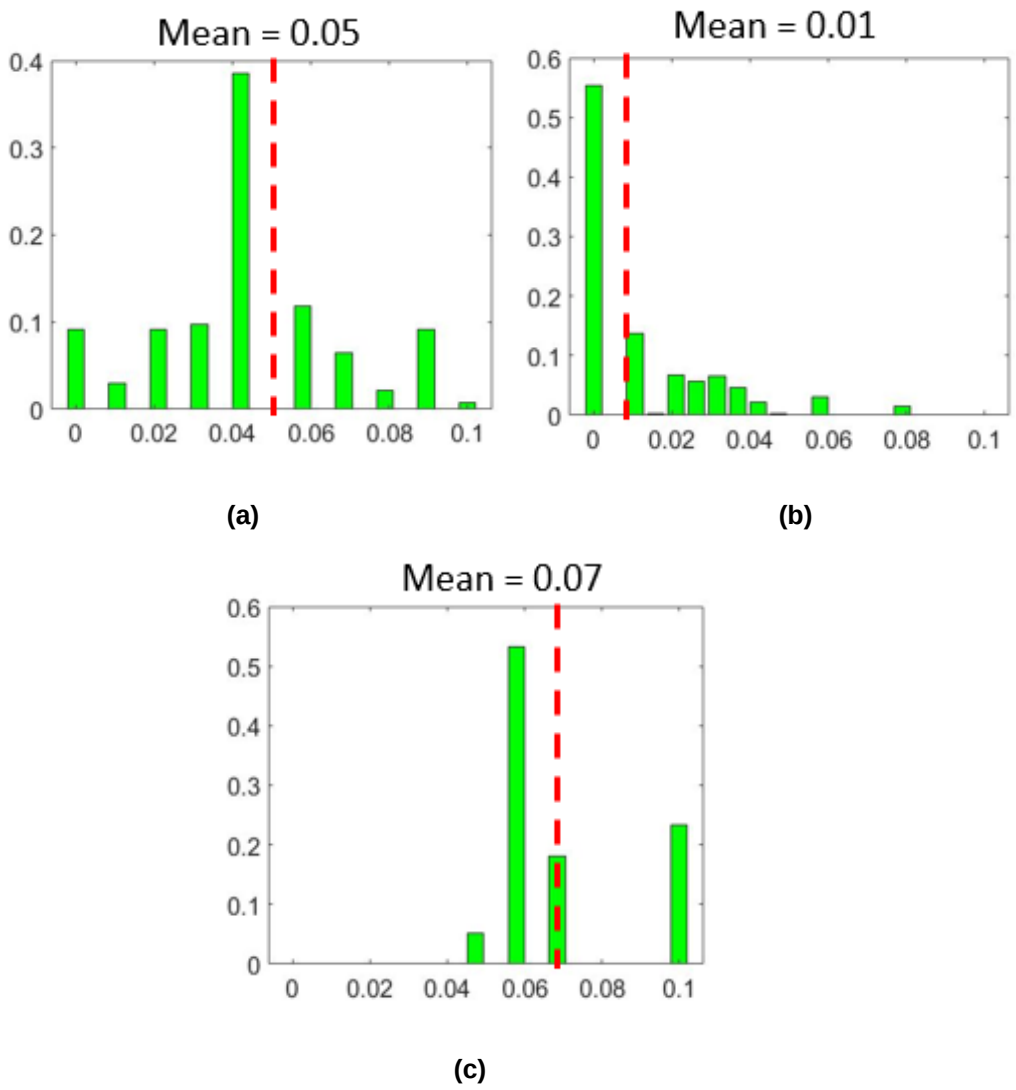

Figure 4.14 Histogram of fault slip potential change of fault segments in (a) DFW Airport Area (b) Fort Worth Basin excludes study area (c) Fault held DFW Airport earthquake

of pressure increase. We could also drew the conclusion that DFW Airport earthquake was caused by pore pressure increase due to wastewater injection in that area.

Figure 4.15 shows the FSP change of Fort Worth Basin at 2010, with the study area of Cleburne earthquake location and **Figure 4.16** shows the histogram of FSP change of three different cases. From **Figure 4.15**, we could see that FSP change at 2010 ranges from 0 to 0.2, with Cleburne area had the highest FSP change values. We could draw the

same conclusion from the comparison of histogram of three different cases shown in **Figure 4.16**, where the mean FSP change of Cleburne area is 0.15, seven times higher than the average FSP change of other areas of Fort Worth Basin. For Cleburne area, we could also conclude that pore pressure increase due to wastewater disposal correlates with seismic events. Also, FSP change value at the onset time of the Cleburne earthquake was different from that of DFW Airport earthquake, which means that it is difficult to determine a specific threshold FSP change value to determine the onset of seismic events.

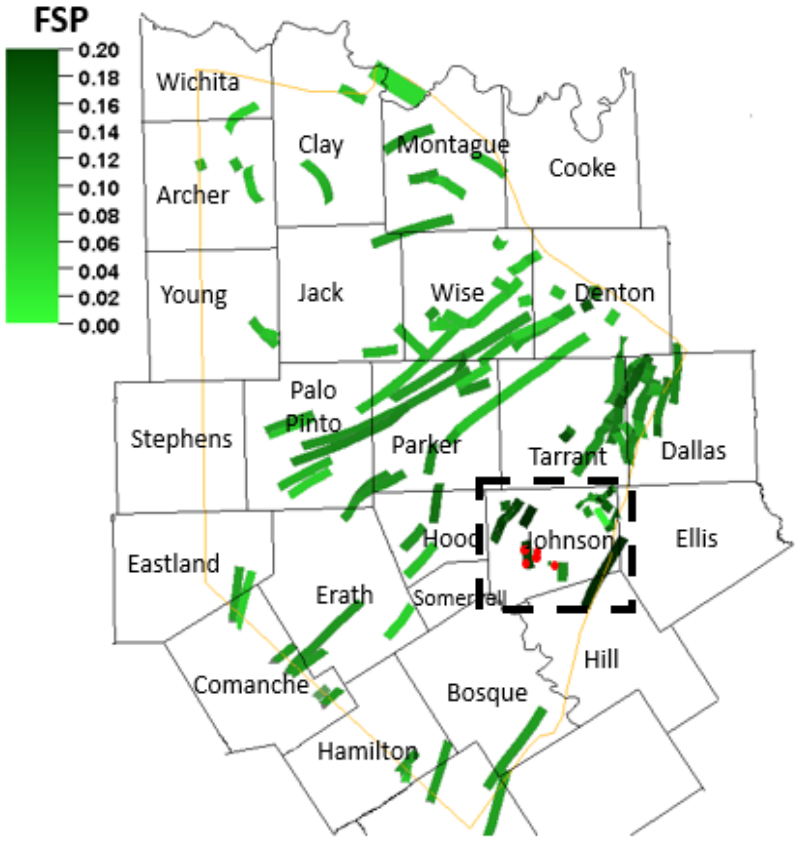

Figure 4.15 Fault slip potential change of Fort Worth Basin at 2010

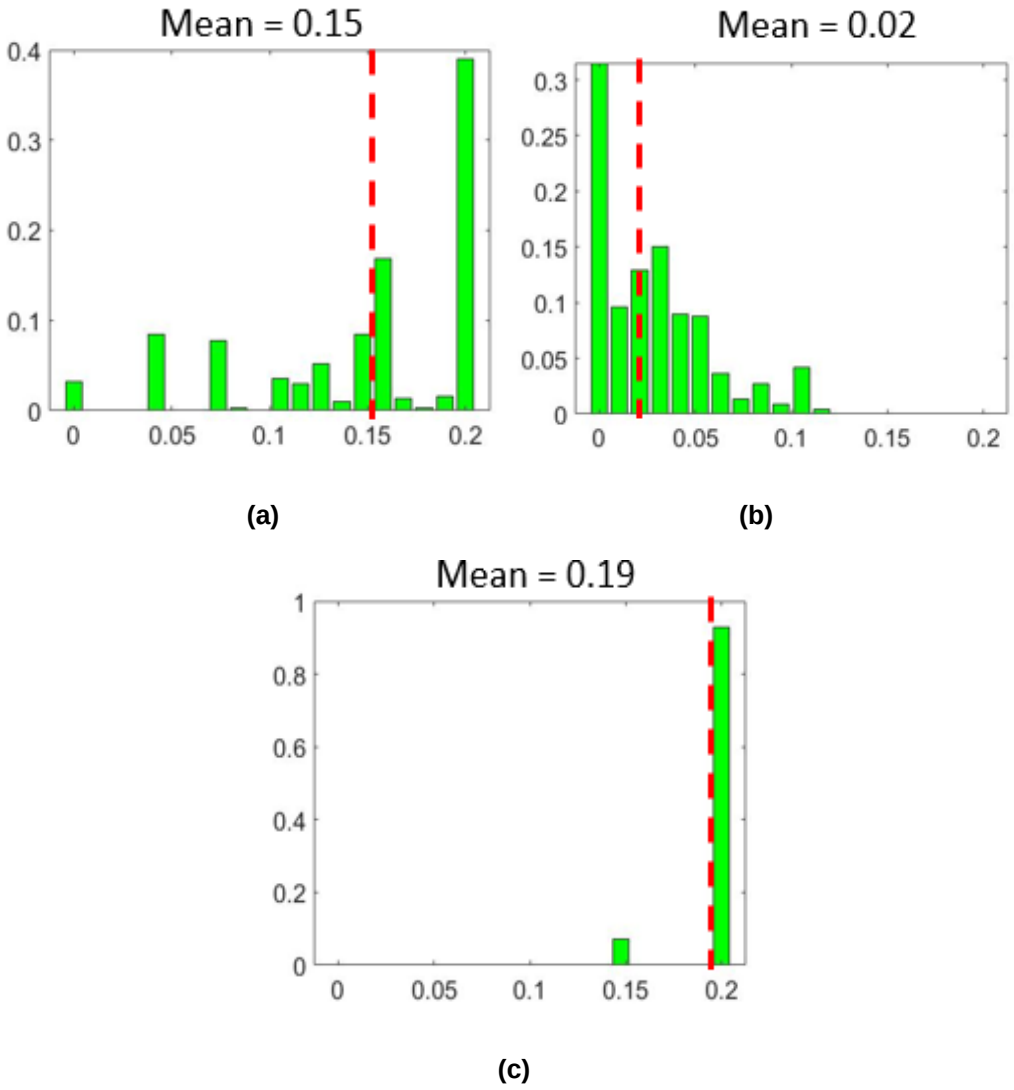

Figure 4.16 Histogram of fault slip potential change of fault segments in (a) Cleburne Area (b) Fort Worth Basin excludes study area (c) Fault held Cleburne earthquake

Figure 4.17 shows the FSP change of Fort Worth Basin at 2013, with the study area to be Azle and **Figure 4.18** shows the histogram of FSP change of three different cases. From **Figure 4.17**, we could see that FSP change at 2013 ranges from 0 to 0.2 and different from previous earthquake sequence, Azle area did not have high FSP change values compared with other areas in Fort Worth Basin. We could also see the detailed

illustration of this phenomenon from **Figure 4.18**, from which we could see that the mean FSP change in Azle area was even lower than that of the other areas in Fort Worth Basin. As we discussed in the previous pore pressure analysis of Azle area, there were pore pressure increase and decrease in this area, causing the moderate change of FSP. This special phenomenon may conclude that pore pressure change is not the controlling mechanism of Azle earthquake.

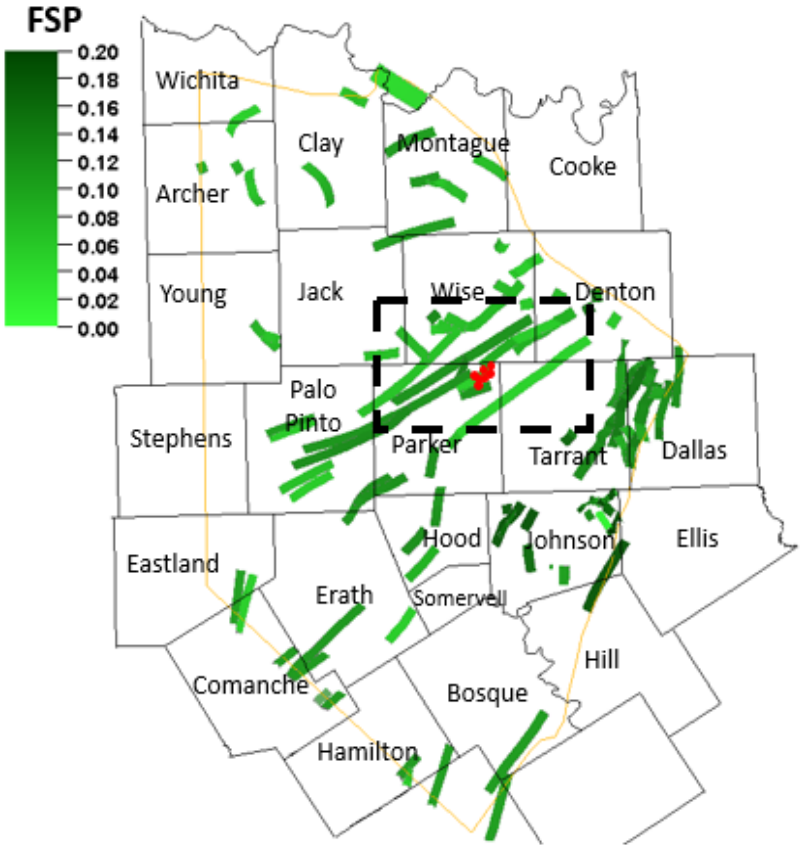

Figure 4.17 Fault slip potential change of Fort Worth Basin at 2013

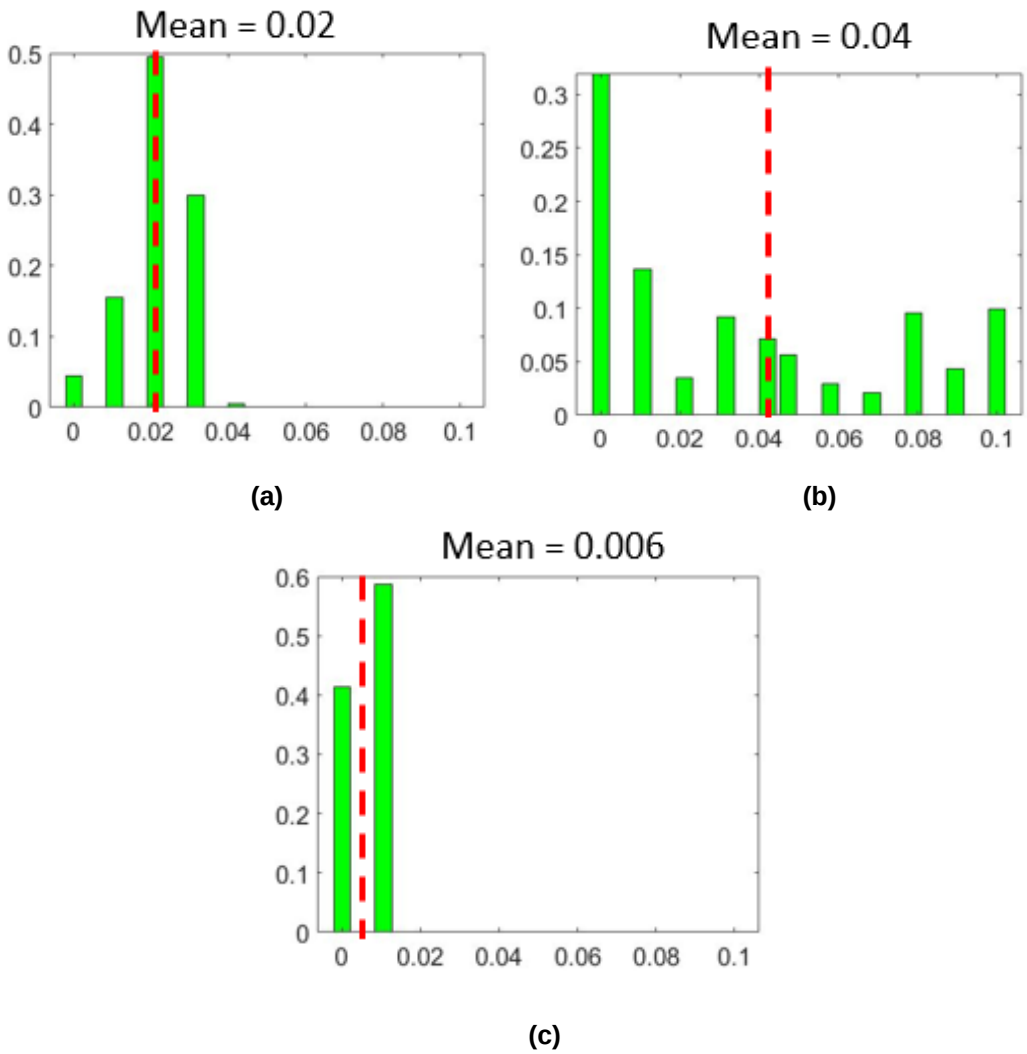

Figure 4.18 Histogram of fault slip potential change of fault segments in (a) Azle Area (b) Fort Worth Basin excludes study area (c) Fault held Azle earthquake

Figure 4.19 shows the FSP change of Fort Worth Basin at 2014, with the study area of Irving earthquake location and **Figure 4.20** shows the histogram of FSP change of three different cases. From **Figure 4.19**, we could see that FSP change at 2014 ranges from 0 to 0.3, with Irving area had the highest FSP change values. We could draw the same conclusion from the comparison of histogram of three different cases shown in **Figure 4.20**, where the mean FSP change of Irving area is 0.14, three times higher than

the average FSP change of other areas of Fort Worth Basin. For Irving area, we could also conclude that pore pressure increase due to wastewater disposal correlates with seismic events.

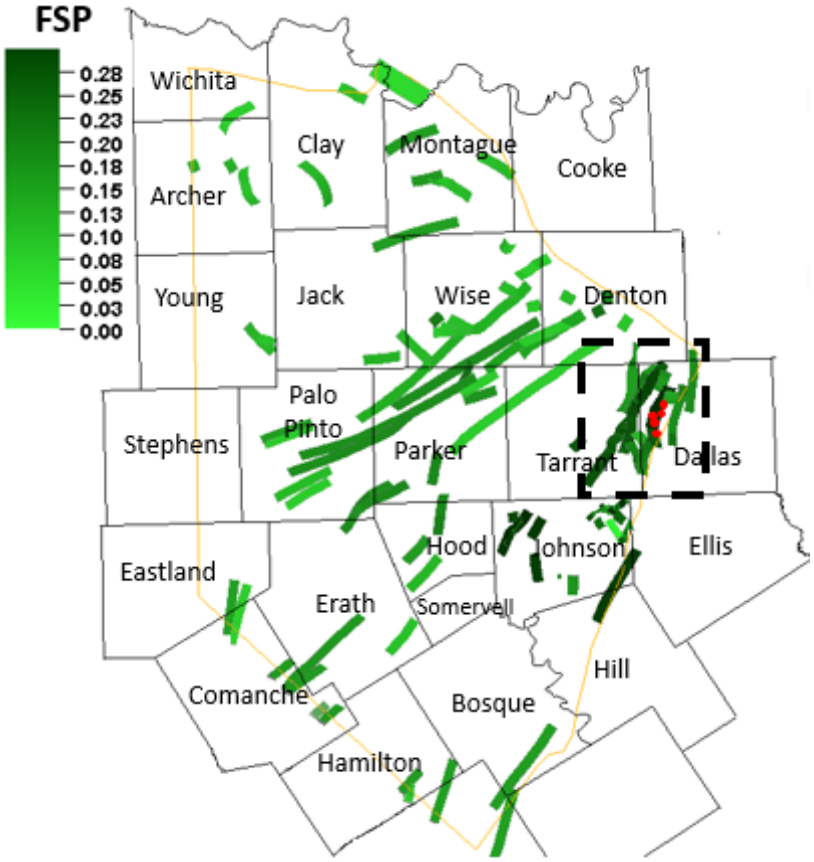

Figure 4.19 Fault slip potential change of Fort Worth Basin at 2014

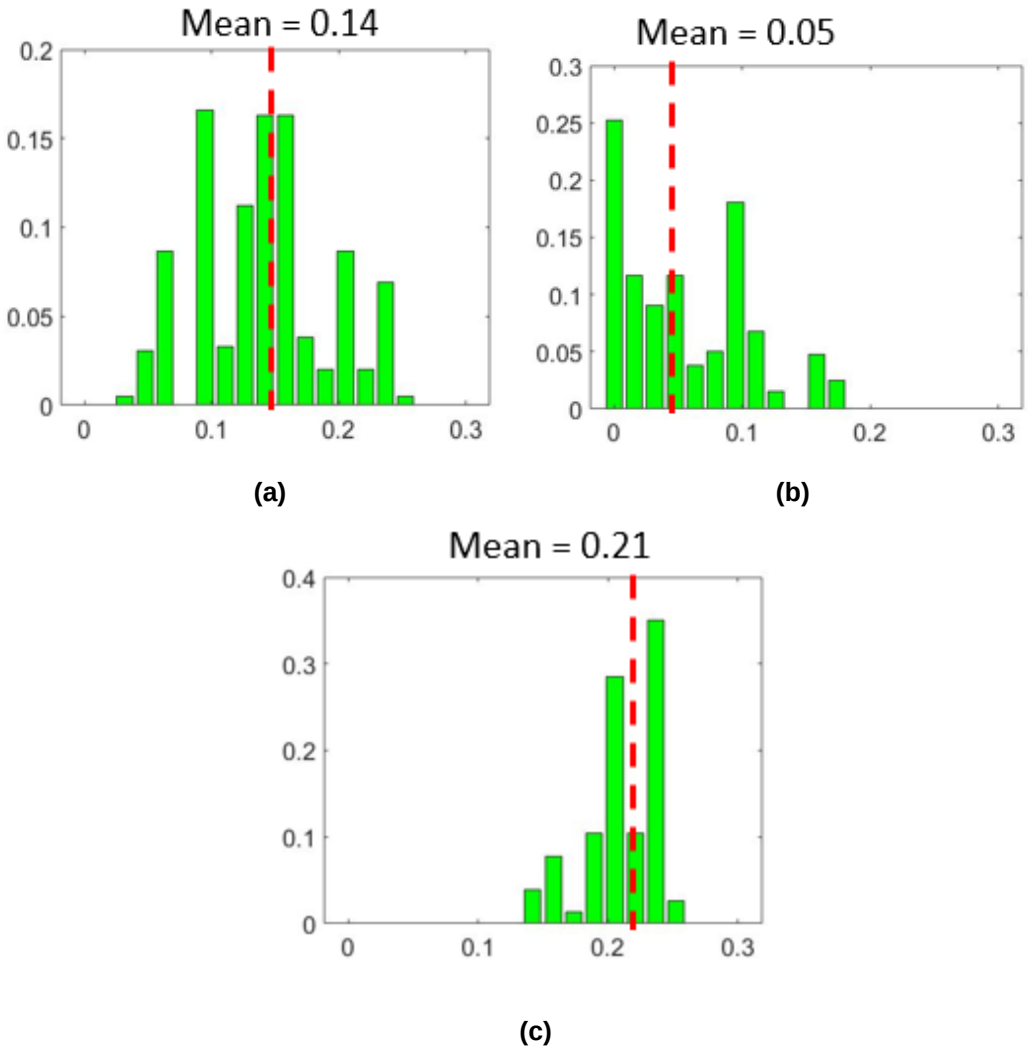

Figure 4.20 Histogram of fault slip potential change of fault segments in (a) Irving Area (b) Fort Worth Basin excludes study area (c) Fault held Irving earthquake

Figure 4.21 shows the FSP change of Fort Worth Basin at 2015, with the study area to be Venus and **Figure 4.22** shows the histogram of FSP change of three different cases. From **Figure 4.21**, we could see that FSP change at 2015 ranges from 0 to 0.5, with Venus area had the highest FSP change values. We could draw the same conclusion from the comparison of histogram of three different cases shown in **Figure 4.22**, where the mean FSP change of Irving area is 0.25, four times higher than the average FSP change of

other areas of Fort Worth Basin. For Venus area, we could also conclude that pore pressure increase due to wastewater disposal correlates with seismic events.

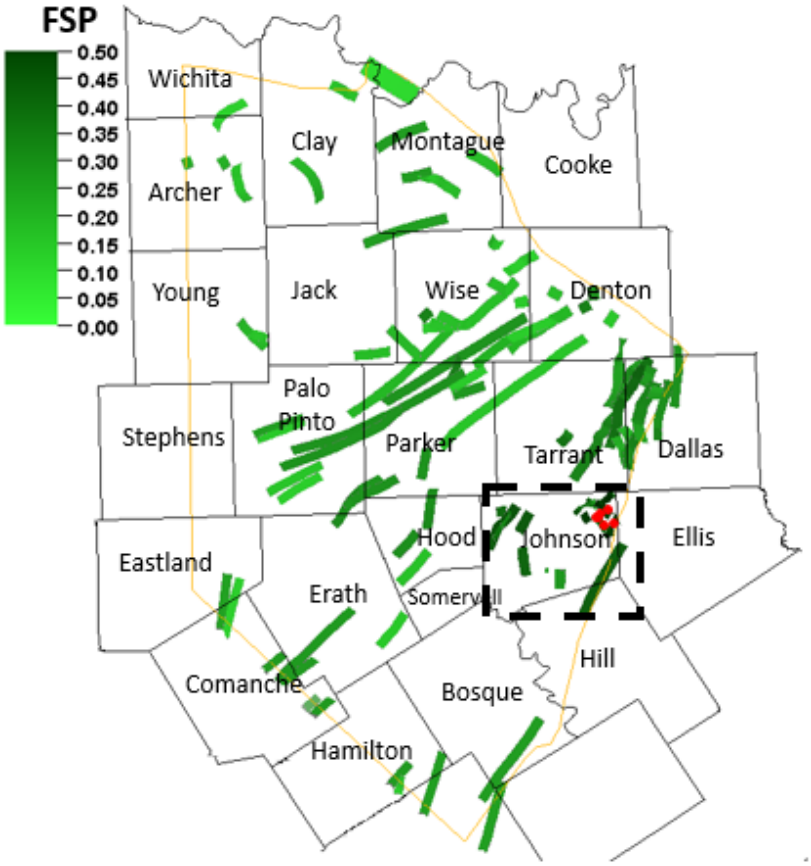

Figure 4.21 Fault slip potential change of Fort Worth Basin at 2015

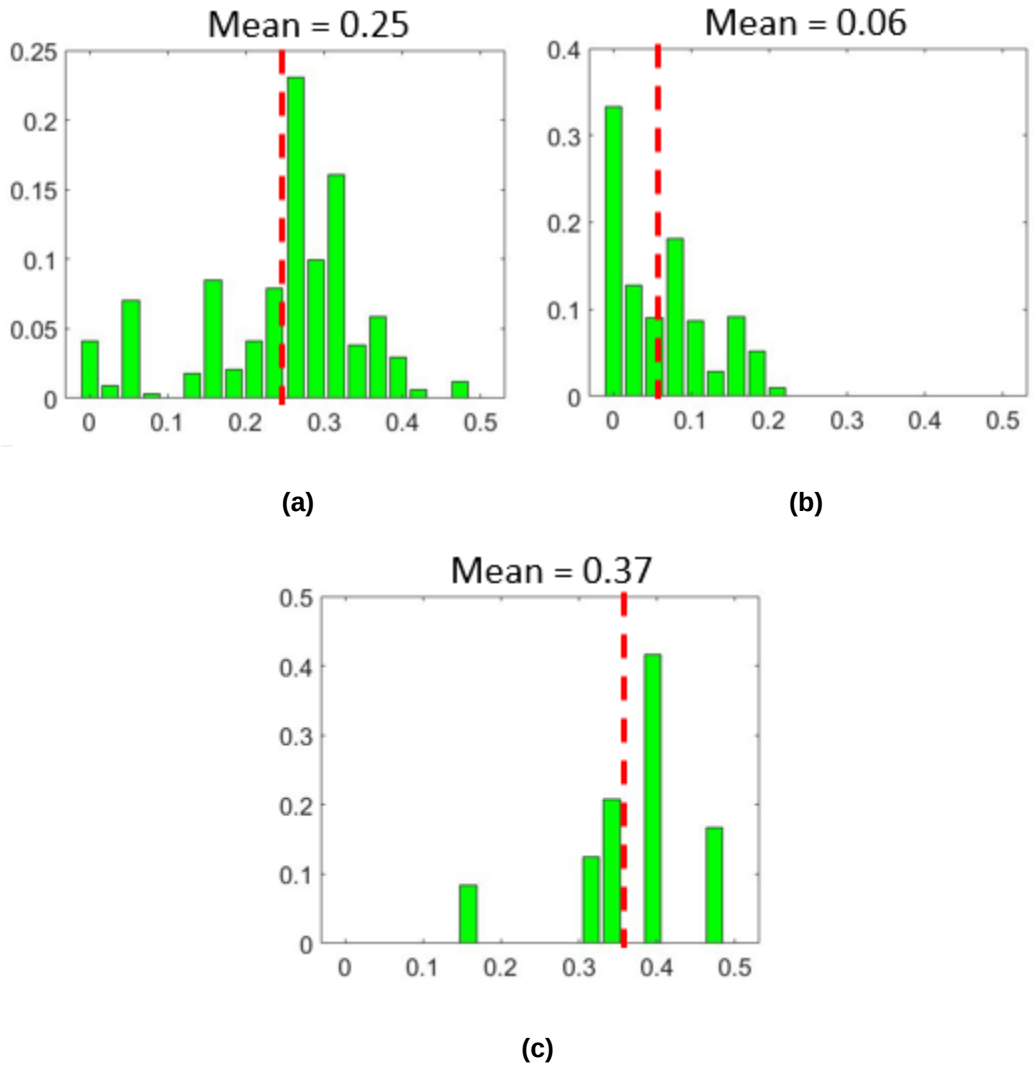

Figure 4.22 Histogram of fault slip potential change of fault segments in (a) Venus Area (b) Fort Worth Basin excludes study area (c) Fault held Venus earthquake

Table 4.4 summarizes the average FSP change in different years at different areas, from which we could see that, except for Azle, study area (earthquake location) always holds the highest mean FSP change value, several times higher than the average FSP change of other areas in the basin. This could be a proof of the controlling mechanism of seismic activities in Fort Worth Basin to be pore pressure increase. However, Azle area is a special case, where the study area does not experience a higher FSP change while having

earthquake occurrence, which means pore pressure change is not the controlling mechanism of seismicity in Azle area. In order to further investigate Azle area, a site-specific study was conducted and will be discussed in the next subchapter. Also, due to increasing amount of wastewater disposal activities in Fort Worth Basin over the years, the average FSP change value of whole basin is increasing, posing a risk of future occurrence of seismic events near critically stressed faults.

Table 4.4 Summary of mean FSP change in different area

Years	Study Area	Whole basin excludes study area	Fault held earthquakes
2008	0.05	0.01	0.07
2010	0.15	0.02	0.2
2013	0.02	0.04	0.006
2014	0.14	0.05	0.21
2015	0.25	0.06	0.37

4.4 Azle Site-Specific Study

In order to further investigate and validate the unbalanced loading mechanism for Azle area, a site-specific study was conducted and introduced in this subchapter. A fine-scale Azle model with more than 2.7 million cells has been constructed. Streamline-based inversion method was used to calibrate the model to BHP of two injectors in Azle area and streamlines are traced after calibration to visualize the flow paths. The injector-producer flow pattern was analyzed to validate the identified controlling mechanism from

previous analysis of pore pressure change and fault slip potential change and previous study (Chen et al. 2019).

4.4.1 Fine-Scale Geologic Model

A high-resolution subsurface geologic model of the Azle area is shown in **Figure 4.23**. This high resolution geologic model has been constructed in the Petrel Geomodeling tool for application to the geomechanical assessment of fault reactivation and seismicity. The domain of the model is a 144 km2 area in NW Tarrant County, NE Parker County, and southern Wise County. The model consists of stratigraphic control surfaces and through-going normal faults that have been interpreted in a 3D structural framework following the general workflow outlined in Krantz and Neely (2016). Approximately 2,000 vertical and horizontal wells from the general region were used to constrain the stratigraphic surfaces in the model (top Lower Barnett formation at ~1,830 m SSTVD, top of Ellenburger formation ~1,920 m SSTVD, and top of igneous and metamorphic basement at ~2,900 m SSTVD). Faults in the region were constrained by an integration of stratigraphic mapping, structural interpretation, earthquake hypocenters (Hornbach et al. 2015), and review of existing publications and public records from the Texas Rail Road Commission. There are three NE-striking normal faults in the model that are in close proximity to the earthquakes: Azle (6.5 km long, 50 m throw at the top of the Ellenburger formation), Azle Antithetic (3.0 km long, 60 m throw), and Reno (3.4 km long, 40 m throw). These faults are part of the Llano Fault System in the Fort Worth Basin as described by Ewing (1991). The lateral extent, strike, and general dip of the faults was

constrained by 3D interpretation and earthquake hypocenter location. The petrophysical interpretation of porosity and permeability for the stratigraphic units in the model was conducted by analysis of 14 wells in the vicinity for which triple combo digital well log suites are available. Porosity was calculated using neutron-density cross plot techniques and a permeability index was derived using porosity to permeability transforms described in Lucia (2007). Total water saturation was calculated using an Archie equation. The calculated petrophysical attributes from the wells were distributed throughout the model using both sequential Gaussian simulation and moving average techniques.

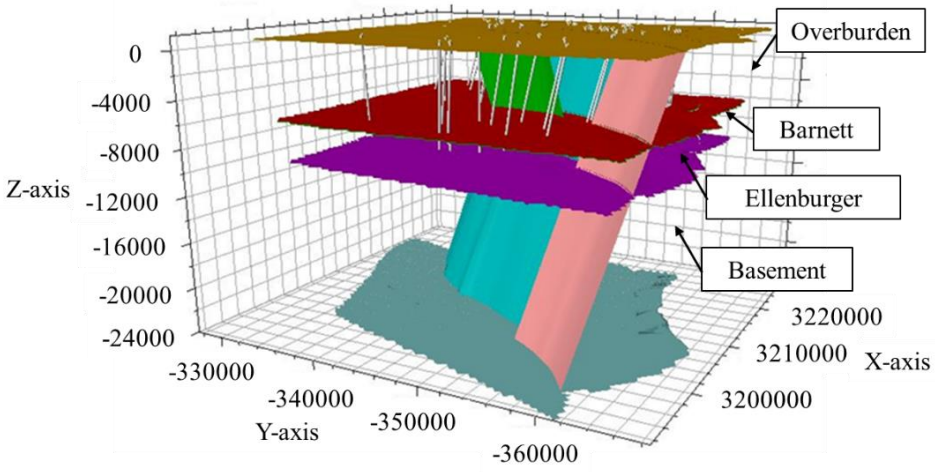

Figure 4.23 Azle fine-scale geologic model

4.4.2 Streamline-based Model Calibration

In this study, BHP data of 2 injectors were used to calibrate the model using streamline-based method and the history matching quality is demonstrated in **Figure 4.24**, which is the normalized data misfit vs. number of iterations. From this figure, we could see that the BHP misfit was reduced by 80% within 10 iterations and the inversion was stabilized after that. **Figure 4.25** shows the well response shift after calibration,

where the black dots are observed BHP converted from THP (Appendix A), blue lines are simulated BHP from the initial model and red lines are simulated BHP from the calibrated model. We could see that after calibration, the simulation results match well with the observed data.

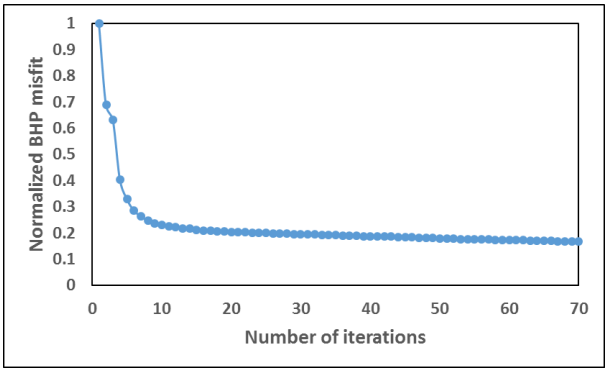

Figure 4.24 Normalized data misfit vs. number of iterations

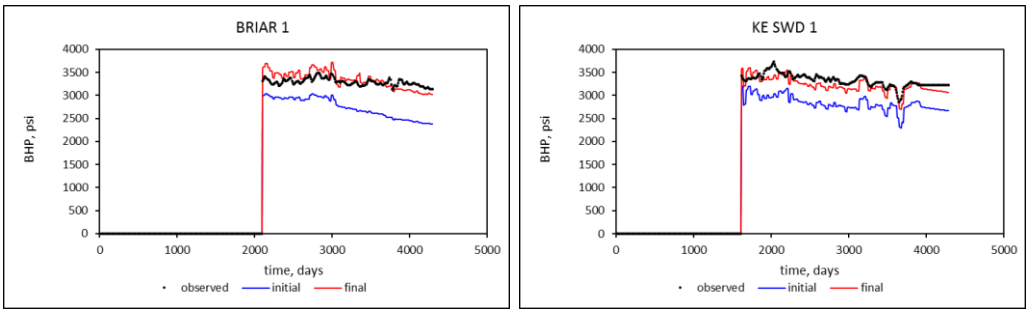

Figure 4.25 Well response shift after calibration

4.4.3 Streamline Visualization and Result Analysis

Streamline was traced based on the flux from simulation results of the calibrated fine-scale model. **Figure 4.26 (a)** shows the streamlines distribution after 10 years of production, where light blue lines are for producers and dark blue lines are for injectors. It is clear that wastewater injected through injectors will not transport to the southeast side of the main fault and also there are more streamlines from producers on the

northwest side of the main fault, consistent with unbalanced loading on different sides of the main fault. From **Figure 4.26 (b)**, we can see that there is no streamline in the basement, indicating there is no volumetric flux or pressure change in the basement. **Figure 4.27** shows the pressure distribution along streamlines after 10 years of production. We can see that there is a pressure difference between the two sides of the main fault, which results in the unbalanced loading on the basement to cause the onset of seismicity at the weaker elements of the basement.

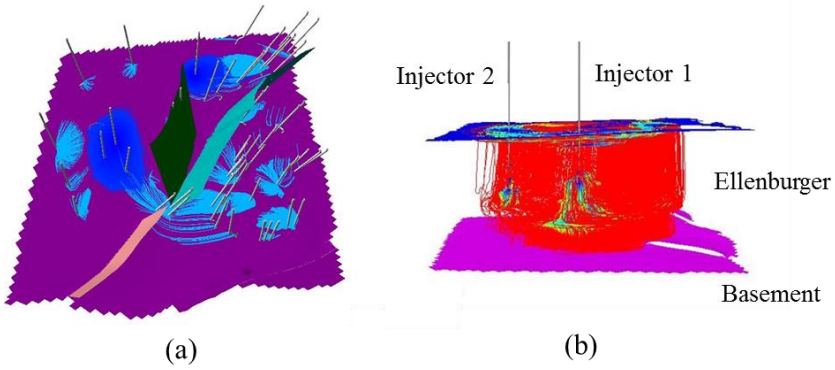

Figure 4.26 (a) Horizontal view of streamlines from producers and injectors (10000 days cut-off) (b) vertical view of streamlines from producers and injectors

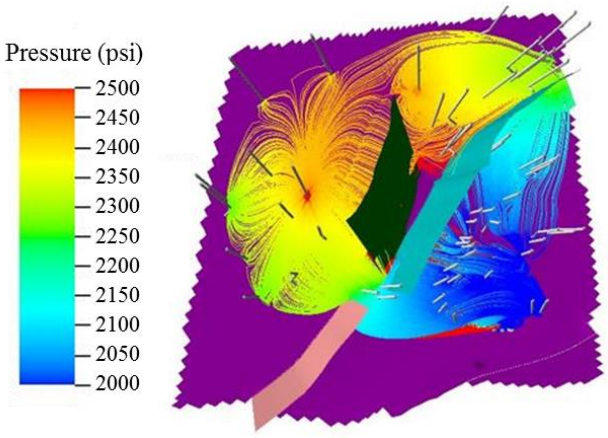

Figure 4.27 Pressure distribution along streamlines

Further investigation of the unbalanced loading mechanism has been conducted by Chen et al. 2019. They performed a coupled fluid flow and geomechanical modeling of Azle and analyzed the relative contribution of pore pressure change and poroelastic stress change on the Coulomb failure stress change ($\Delta\tau$), which is defined as

$$\Delta\tau = \Delta\tau_s + \mu(\Delta p + \Delta\sigma) = \mu\Delta p + (\Delta\tau_s + \mu\Delta\sigma) \tag{4.1}$$

where $\Delta\tau_s$ is the change in the shear stress, $\Delta\sigma$ is the change in normal stress calculated on the fault, Δp is the change in pore pressure and μ is the friction coefficient. **Figure 4.28** shows the change in pore pressure versus the change in poroelastic stress at the top of the basement, from which we could see that poroelastic stress change dominate in the basement with no noticeable change in pore pressure. This study further validated that Azle earthquake was triggered due to poroelastic stress transmitted to the basement without elevated pore pressure.

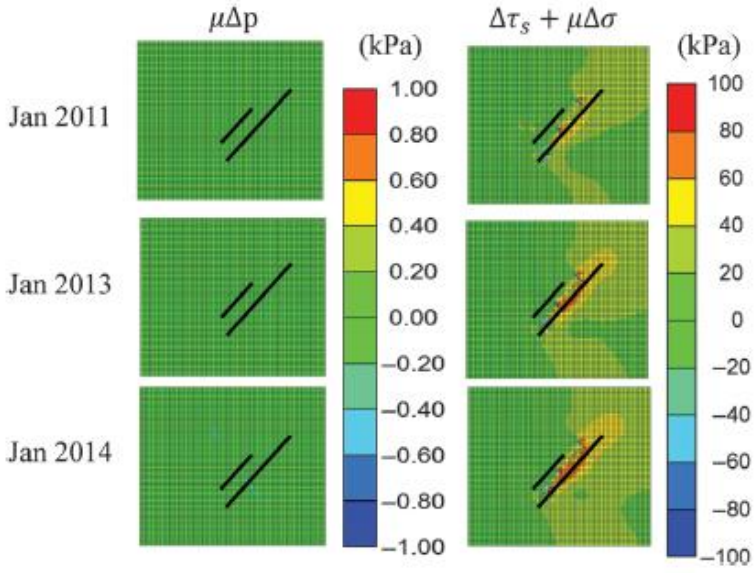

Figure 4.28 Pore pressure change and poroelastic stress change at the top of basement (Chen et al. 2019)

4.5 Summary

In this chapter, we analyzed pore pressure change from the fluid flow simulation results of the calibrated coarsened Fort Worth Basin model and also the fault-slip potential change calculated based on our pore pressure modeling results and fault framework model. From the pore pressure change analysis, we concluded that, except for Azle earthquake, other earthquake sequences that occurred in Fort Worth Basin over the years had temporal and spatial correlation with pore pressure increase due to wastewater disposal activities and the magnitude of pore pressure increase at onset time of seismic events varied from location to location, which may depend on the stress state of the fault. From the fault-slip potential change analysis, we further validated the correlation between seismic events and pore pressure increase due to wastewater injection. For the special phenomenon in Azle area, where we found both pore pressure increase and decrease and fault-slip potential did not increase at the time of Azle earthquake, we proposed the controlling mechanism of Azle earthquake to be unbalanced loading on different sides of the fault, which was validated by the Azle site-specific study. Another Azle site-specific study (Chen et al. 2019) also validated the unbalanced loading mechanism in Azle area through a coupled geomechanical and fluid flow modeling method, in which they concluded that poroelastic stress change transmitted to the basement triggered seismicity without elevated pore pressure.

CHAPTER V

SUMMARY AND RECOMMENDATIONS

5.1 Summary

In Chapter I-III, we presented the upscaling and calibration of a high resolution basin-scale geologic model. For the purpose of increasing computation efficiency, we adopted a combination of areal coarsening and layer coarsening. For vertical coarsening, we used a recursive sequential coarsening method, while for areal coarsening, we used a simple structural upgridding. Validation test was conducted on the coarsened model to validate the upscaling quality, including visual comparison of permeability field and porosity field, streamline TOF and streamline flow partition. After upscaling, , we have successfully reduced more than 90% of the number of grid cells, which resulted in a computational speed up factor of 100 without significant loss of accuracy in flow response. Our calibration workflow relies on a streamline-based inversion technique. Bottom-hole pressure of 104 injectors were integrated into the model during the calibration process.

In Chapter IV, pore pressure change and fault-slip potential were analyzed to understand the controlling mechanism of seismic events in Fort Worth Basin. Spatial and temporal correlations between seismic events and the location of pore pressure increase are evident from the pore pressure modeling results. The level of spatial and temporal correlations varies between locations, however a clear visual spatial correlation can be observed. Pore pressure increase leads to a higher potential of the faults to slip in area of

interest. The pore pressure simulation results and fault slip potential results are summarized below.

For the DFW Airport earthquakes, areas of pore pressure increase were observed at the last layer of Ellenburger at the onset time of seismic events, November 2008. Two injectors located in DFW Airport area corresponded to the areas of pore pressure increase. In terms of temporal correlation, DFW Airport earthquakes began after the injection activities of the "South Well" in DFW Airport area. In terms of spatial correlation, DFW Airport earthquake occurred near the area of pore pressure increase and the magnitude of pore pressure increase at the time of earthquake was 50psi. Based on the fault slip potential analysis, at 2008, DFW Airport area had the highest fault slip potential change values compared to other areas in Fort Worth Basin. So we could conclude that the controlling mechanism of seismic events in DFW Airport area to be pore pressure increase.

For the Cleburne earthquakes, there is a strong spatial and temporal correlation between earthquake events and areas of increased pore pressure, with a magnitude of 100 psi. Fault slip potential change analysis, in which Cleburne area had the highest FSP change at 2010, also confirmed that there was correlation between pore pressure increase and seismic events. So we could also conclude that the controlling mechanism of seismic events in Cleburne area to be pore pressure increase.

For the Azle earthquakes, however, there was not direct correlation between pore pressure increase and seismic events since we identify both pore pressure increase and pore pressure decrease occurred in Azle area. There was a pressure imbalance between two sides of the fault that held the Azle earthquake, where we found a pore pressure

increase with a magnitude of 50 psi on one side of the fault and a pore pressure decrease of 150 psi on the other side of the fault. A 200 psi pressure imbalance may cause an unbalanced loading on the fault and lead to the onset of the seismic events at the weaker elements of the basement. Fault-slip potential analysis also confirmed that there was no obvious FSP change increase in Azle area at 2013. Site-specific study of Azle area further validated our proposed mechanism of unbalanced loading.

For the Irving earthquakes, there is a strong spatial and temporal correlation between earthquake events and areas of increased pore pressure, with a magnitude of 150 psi. Fault slip potential change analysis, in which Irving area had the highest FSP change at 2014, also confirmed that there was correlation between pore pressure increase and seismic events. So we could also conclude that the controlling mechanism of seismic events in Irving area to be pore pressure increase.

For the Venus earthquakes, there is a strong spatial and temporal correlation between earthquake events and areas of increased pore pressure, with a magnitude of 200 psi. Fault slip potential change analysis, in which Venus area had the highest FSP change at 2015, also confirmed that there was correlation between pore pressure increase and seismic events. So we could also conclude that the controlling mechanism of seismic events in Venus area to be pore pressure increase.

From the pore pressure change analysis and FSP change analysis, we could find that both pore pressure increase and FSP increase at the location of earthquakes at their onset time vary from location to location. So there is no threshold value of pore pressure increase and FSP increase to determine the onset of seismic events.

5.2 Recommendation

Since there is no specific threshold value of pore pressure increase and fault slip potential increase to determine the onset of seismic events, further geomechanical modeling is needed to evaluate the risk of seismicity. Pore pressure change and fault slip potential modeling could serve as the fundamental step to identify the area with high risk of earthquake occurrence and site-specific geomechanical modeling should be conducted to further investigate the area of interest. Fault interpretation is also important for seismicity risk evaluation since the accuracy of fault slip potential calculation and geomechanical modeling rely on the confidence of fault information.

REFERENCES

Ansari, A. M., N. D. Sylvester, O. Shoham, and J. P. Brill. 1990, A comprehensive mechanistic model for upward two-phase flow in wellbores. Paper SPE 20630 presented at SPE Annual Technical Conference and Exhibition, New Orleans, LA, USA, 23-26 September.

Beggs, D. H., and J. P. Brill, 1973. A study of two-phase flow in inclined pipes: *Journal of Petroleum Technology*, 25, 607-617.

Bradley, H. B., 1987. Petroleum engineering handbook: Society of Petroleum Engineers.

Chen, H., Onishi, T., Olalotiti-Lawal, F., & Datta-Gupta, A. (2020). Streamline tracing and applications in embedded discrete fracture models. *Journal of Petroleum Science and Engineering*, 106865.

Chen, H., Yang, C., Datta-Gupta, A., Zhang, J., Chen, L., Liu, L., Bahar, A. (2019, March 22). A Hierarchical Multiscale Framework for History Matching and Optimal Well Placement for a HPHT Fractured Gas Reservoir, Tarim Basin, China. International Petroleum Technology Conference. doi:10.2523/IPTC-19314-MS

Chen, N. H., 1979. An explicit equation for friction factor in pipe: *Industrial & Engineering Chemistry Fundamentals*, 18, 296-297.

Chen, R.Q., Xue X., Yao C.Q. et al. 2018. Coupled Fluid Flow and Geomechanical Modeling of Seismicity in the Azle Area North Texas. Paper SPE 191623 presented at SPE Annual Technical Conference and Exhibition, Dallas, Texas, USA, 24-26 September.

Chen, R.Q., Xue X., Park, J. et al. 2019. New insights into the mechanisms of seismicity in the Azle area, North Texas: *Geophysics 85* (01): 1JF-Z3

Cheng, H., Osaka, I., Data-Gupta, Akhil et al. 2006. A rigorous compressible streamline formulation for two and three-phase black oil simulation: *SPE Journal 11* (04): 407-417

Economides, M. J., A. D. Hill, C. Ehlig-Economides, and D. Zhu, 2013, Petroleum production systems: Pearson Education.

Gono, V., Olson, J. E., & Gale, J. F. 2015. Understanding the Correlation between Induced Seismicity and Wastewater Injection in the Fort Worth Basin. Paper AMRA 15-00419 presented at the 49th US Rock Mechanics/ Geomechanics Symposium, San Francisco, CA, USA, 28 June – 1 July.

Durlofsky, L.J., R.A.Behrens, R.C.Jones, and A.Bernath, 1996. Scale Up of Heterogeneous Three Dimensional Reservoir Descriptions. *SPE Journal* 313.

Du, S, 2012. Multiscale Reservoir Simulation: Layer Design, Full Filed Pseudoization and Near Well Modeling. Dissertation.

Frohlich, C. et al. 2011. The Dallas-Fort Worth Earthquake Sequence: October 2008 through May 2009. *Bulletin of the Seismological Society of America, 101*(1): 327-440

Frohlich, C. 2012a. A Survey of Earthquakes and Injection Well Locations in the Barnett Shale, Texas. *The Leading Edge, 31*(12): 1446-1451

Frohlich, C. 2012b. Two-year Survey Comparing Earthquake Activity and Injection-Well Locations in the Barnett Shale, Texas. *Proceedings of the National Academy of Sciences, 109*(35): 13934-13938

Frohlich, C., DeShon H., Stump B., et al. 2016. A Historical Review of Induced Earthquakes in Texas. *Seismological Research Letters* 87(4): 1022-1038.

Granville, V., Krivanek, M. and Rasson, J. P. 1994. Simulated Annealing: A Proof of Convergence: Pattern Analysis and Machine Intelligence, *IEEE Transactions on 16* (6): 652-656, DOI: 10.1109/34.295910.

Govier, G. W., and K. Aziz, 1972. The flow of complex mixtures in pipes: Van Nostrand Reinhold Company.

Hastings, W. K. 1970. Monte Carlo Sampling Methods Using Markov Chains and Their Applications. *Biometrika 57* (1): 97-109, DOI: 10.1093/biomet/57.1.97.

Hoffman, B. T., Caers, J. K., Wen, X. and Strebelle, S. B. 2006. A Practical Data Integration Approach to History Matching: Application to a Deepwater Reservoir: *SPE Journal 11* (04): 464-479, DOI: 10.2118/95557-PA.

Hosseini, S.A. and Kelkar, M.G. 2008. Analytical Upgridding Method to Preserve Dynamic Flow Behavior. Paper SPE 116113 presented at SPE Annual Technical Conference and Exhibition, Denver, Colorado, USA, 21-24 September

Justinic, A.H. et al. 2013. Analysis of the Cleburne, Texas, Earthquake Sequence from June 2009 to June 2010. *Bulletin of the Seismological Society of America*, 103 (6): 30833093-

King, M.J., K.S.Burn, Pengju Wang, et al. 2005. Optimal Layer coarsening of 3D Reservoir Models for Flow Simulation. Paper SPE 96258 presented at SPE Annual Technical Conference and Exhibition, Dallas, Texas, USA, 9-12 October.

Li, D. and Lake, L.W. 1995. Scaling Fluid Flow through Heterogeneous Permeable Media. *SPE Advanced Technology Series 3* (1): 188-197. DOI: 10.2118/26648-pa

Li, D., and B.Becker. 2000. Optimal Uplayering for Scaleup of Muitimillion-Cell Geologic Models. Paper SPE 62927 presented at SPE Annual Technical and Exhibition, Dallas, Texas, USA, 1-4 October

Liu, T., Chen, H., Hetz, G., & Datta-Gupta, A. (2020). Integration of time-lapse seismic data using the onset time approach: The impact of seismic survey frequency. *Journal of Petroleum Science and Engineering*, 106989.

Mattew J. Hornbach, Madeline Jones, et al. 2016. Ellenburger Wastewater Injection and Seismicity in North Texas, *Physics of the earth and planetary interiors*, 261 (A): 54-68.

Peter H. Hennings, Jens-Erik Lunk Snee, etal. 2019. Injection-Induced Seismicity and Fault-Slip Potential in the Fortt Worth Basin, Texas, *Bulletin of the Seismological Society of America*, 109:1615-1634.

Stern, D. and Dawson, A.G. 1999. A Technique for Generating Reservoir Simulation Grids to Preserve Geologic Heterogeneity. Paper SPE 51942 presented at SPE Reservoir Simulation Symposium, Houston, Texas, USA, 14-17 February

Taitel, Y., D. Barnea, and A. Dukler, 1982. A film model for the prediction of flooding and flow reversal for gas-liquid flow in vertical tubes: *International Journal of Multiphase Flow*, 8: 1-10.

Tanaka, S., Kam, D., Datta-Gupta, A. et al. 2015: Streamline-based history matching of arrival times and bottom-hole pressure data for multicomponent compositional systems. Paper SPE 174750 presented at SPE Annual Technical Conference and Exhibition, Houston, Texas, 28-30 September

Vasco, D Wr, Seongsik, and Datta-Gupta, Akhil, 1999: Integrating dynamic data into high-resolution reservoir models using streamline-based analytic sensitivity coefficients: *SPE Journal 4* (04): 389-399.

Vega, L., Rojas, D. and Datta-Gupta, A. 2004. Scalability of the Deterministic and Bayesian Approaches to Production-Data Integration into Reservoir Models: *SPE Journal 9* (03): 330-338, DOI: 10.2118/88961-PA.

Watanabe, S., Han, J., Hetz, G. et al. 2017: Streamline-based time-lapse-seismic data integration incorporating pressure and saturation effects, *SPE Journal 22* (04): 1261-1279, DOI: 10.2118/166395-PA

Yang, P. H. and Watson, A. T. 1988. Automatic History Matching With Variable-Metric Methods: *SPE Journal 3* (03): 995-1,001, DOI: 10.2118/16977-PA.

APPENDIX A

TUBING HEAD PRESSURE (THP) TO BOTTOM HOLE PRESSURE (BHP)

The THP to BHP calculation is routine in the petroleum engineering literature (Govier and Aziz, 1972; Beggs and Brill, 1973; Chen, 1979; Taitel et al., 1982; Bradley, 1987; Ansari et al., 1990; Economides et al., 2013). The calculation below follows Economides et al. (2013). Since injection wells in this study are wastewater disposal wells, a single-phase incompressible flow model will be used. The Reynolds number needs to be calculated to determine if the flow is laminar or turbulent

$$N_{re} = \frac{Du\rho}{\mu}, \tag{B-1}$$

where D is the wellbore diameter, u is the average velocity, ρ is the fluid density, and μ is the fluid viscosity. If N_{re} is larger than 2100 (Economides et al., 2013), it is turbulent flow. Otherwise, it is laminar flow.

The overall pressure drop between the well head and the bottom hole consists of three parts: potential energy, kinetic energy, and frictional pressure drop

$$\Delta p = \Delta p_{PE} + \Delta p_{KE} + \Delta p_F . \tag{B-2}$$

Since there is no change in the inner diameter of the disposal well and thus no change in the velocity of the fluid $\Delta p_{KE} = 0$. Δp_{PE} accounts for the pressure change due to the weight of the column of fluid. Since the injected fluid is water, the potential energy change is low and it can be calculated as:

$$\Delta p_{PE} = \frac{g}{g_c}\rho\Delta Z , \tag{B-3}$$

where ΔZ is the difference in elevation. The frictional pressure drop Δp_F can be obtained from the Fanning equation (Fanning, 1892):

$$\Delta p_F = \frac{2 f_f \rho u^2 L}{g_c D}, \tag{B-4}$$

where u is the velocity and f_f is the Fanning friction factor:

$$f_f = \begin{cases} \dfrac{16}{N_{re}}, N_{re} < 2100 \\ \dfrac{1}{-4\log\left(\dfrac{\epsilon}{3.7065} - \dfrac{5.0452}{N_{re}} * \log\left(\dfrac{\epsilon^{1.1098}}{2.8257} + \left(\dfrac{7.149}{N_{re}} \right)^{0.8981} \right) \right)^2}, N_{re} > 2100 \cdot \end{cases} \tag{B-5}$$

APPENDIX B

GAS PRODUCTION CALCULATION

In this study, gas production was converted at the surface condition to the reservoir condition, which is a routine calculation in reservoir engineering.

The gas formation volume factor, B_g, defined as the ratio of the volume of gas at the reservoir temperature and pressure to the volume at the standard temperature and pressure, can be calculated by rearranging the real gas equation (Dake 2013):

$$B_g = \frac{V_{res}}{V_{sc}} = \frac{\mathrm{p}_{sc} * z * T}{Z_{sc} * T_{sc} * \mathrm{p}_{res}} \tag{B-1}$$

The standard condition pressure and temperature are:

$$\mathrm{p}_{sc} = 14.7\ psi \tag{B-2}$$

$$T_{sc} = 520°R \tag{B-3}$$

We use a pressure gradient of 0.45psi/ft and a geothermal gradient of 12°F/1000ft (Rathje and Olson 2007). The average depth for Barnett is 2100m which corresponds to 6888ft. We can then calculate reservoir pressure and temperature.

$$\mathrm{p}_{res} = 3100\ psi \tag{B-4}$$

$$T_{res} = 603°R \tag{B-5}$$

The only unknown is the gas compressibility factor, Z, which requires the gas composition. The gas composition is shown in Table B-1 (Hill et al. 2007).

Table B-1: Gas composition and critical pressure and temperature calculation.

	C_1	C_2	C_3	CO_2	N_2	Mixture
Gas Composition	93.7	2.6	0	2.7	1	
Critical Temperature (^oR)	343.30	549.90	666.10	547.80	227.40	
Critical Pressure (psi)	666.00	708.00	616.00	1071.60	493.10	
y_i*T_c	321.67	14.30	0	14.79	2.27	353.0
y_i*P_c	624.04	18.41	0	28.93	4.93	676.3

Knowing the gas compressibility, we estimate the Z-factor to be 0.82 (McCain 1990). Substituting back into Eq. B-1,

$$B_g = \frac{14.7*0.82*603}{1*520*3100} = 0.00451\left[\frac{rm^3}{sm^3}\right] \quad \text{(B-6)}$$

APPENDIX C

FAULT SLIP POTENTIAL CALCULATION AND RESULTS

FSP calculates the probability that planar fault segments will be critically stressed with the ambient stress field at a modeled pore pressure using a linearized Mohr-Coulomb failure criterion. Fault slip with Mohr-Coulomb failure criteria can be graphically analyzed using Mohr-Circle (**Figure C1**), which could be drawn with effective normal stresses. Given principle stresses ($\sigma_1 > \sigma_2 > \sigma_3$), effective stresses σ' could be calculated as follows:

$$\sigma_i' = \sigma_i - P$$

where P is fluid pressure. We could see that the Mohr-Circle could shift due to fluid pressure change, which would have an impact on the failure criteria of a fault plane. In **Figure C1**, dashed blue line corresponds to Mohr-Coulomb failure line, the slope of

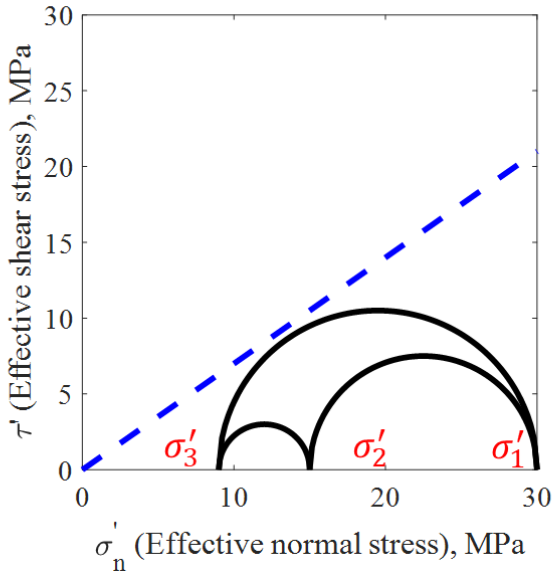

Figure C1 Illustration example of Mohr-Circle

which depends on friction coefficient and the intercept of which depends on cohesion. If the Mohr-Circle touches the line, there is a slip given stress state and the slip would start in the most vulnerable plane.

In Mohr-Coulomb theory, each fault plane is represented by a point in Mohr-Circle after projecting effective principle stresses on given fault plane. The projection consists of two series of stress transform: 1) principle stress coordinate to global coordinate; 2) global coordinate to fault plane coordinate. For the first step, the transformation is based on a series of equations:

$$\sigma_e = R_1^T \sigma_p R_1$$

$$\sigma_p = \begin{Bmatrix} \sigma_H & 0 & 0 \\ 0 & \sigma_h & 0 \\ 0 & 0 & \sigma_V \end{Bmatrix}$$

$$R_1 = \begin{Bmatrix} \cos(\alpha_s)\cos(\beta_s) & \sin(\alpha_s)\cos(\beta_s) & \sin(\beta_s) \\ -\sin(\alpha_s) & \cos(\alpha_s) & 0 \\ -\cos(\alpha_s)\sin(\beta_s) & -\sin(\alpha_s)\sin(\beta_s) & \cos(\beta_s) \end{Bmatrix}$$

where σ_p is principal stress, σ_e is global stress, α_s is azimuth of σ_h (North to East)) and β_s is the angle between σ_v and $\sigma_{v'}$. **Figure C2** also shows the definitions of these parameters. For the second step, the transformation is based on another series of equations:

$$\sigma_f = R_2 \sigma_p R_2^T$$

$$\sigma_e = R_1^T \sigma_p R_1$$

$$R_2 = \begin{Bmatrix} \cos(\alpha_w)\cos(\beta_w) & \sin(\alpha_w)\cos(\beta_w) & \sin(\beta_w) \\ -\sin(\alpha_w) & \cos(\alpha_w) & 0 \\ -\cos(\alpha_w)\sin(\beta_w) & -\sin(\alpha_w)\sin(\beta_w) & \cos(\beta_w) \end{Bmatrix}$$

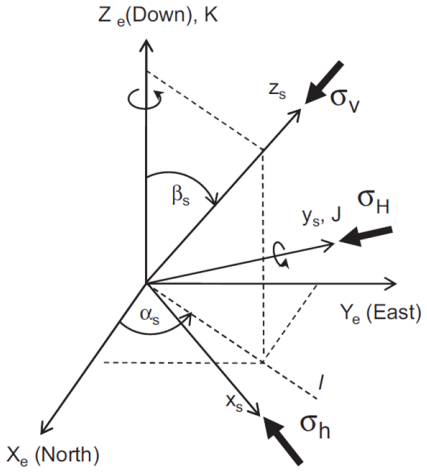

Figure C2 Illustration of stress transformation from principal to global

where σ_e is global stress, σ_f is stress of fault plane, α_w is dip direction minus 180^0 and β_w is dip angle. **Figure C3** also shows the definitions of these parameters.

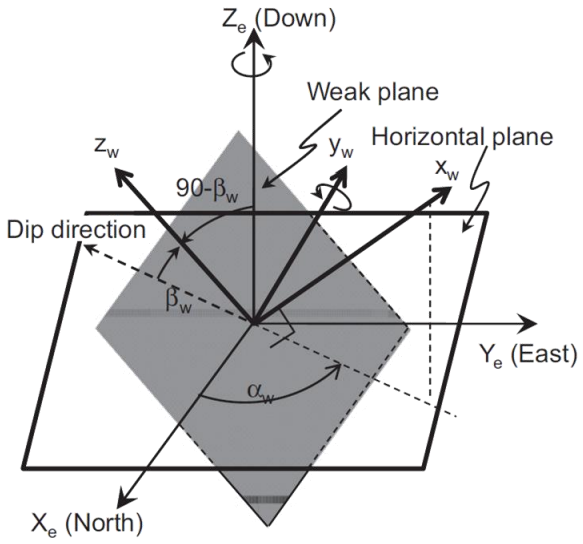

Figure C3 Illustration of stress transformation from global to fault plane

After these two transformation, the normal stress σ_w on a fault plane and shear stress τ_w on a fault plane is defined as:

$$\sigma_w = \sigma_{xx}^w$$

$$\tau_w = \sqrt{(\sigma_{xy}^w)^2 + (\sigma_{xz}^w)^2}$$

The workflow of fault flip calculation is threefold: First, we need to generate multiple realizations within the uncertain range of input parameters (**Table 4.2**) using Monte-Carlo approach. Then evaluate fault slip using linearized Mohr-Coulomb failure criteria. The last step is to calculate the percentage of realizations that met Mohr-Coulomb failure criteria, which is the fault slip potential. **Figure C4** shows an example further illustrates the definition of fault slip potential and the impact of pore pressure increase to the result of fault slip potential. In **Figure C4**, we has three cases: the initial case, in which

we use hydrostatic pressure gradient to calculate pore pressure; case with a pore pressure increase of 1MPa and case with a pore pressure increase of 2Mpa. We could see that for

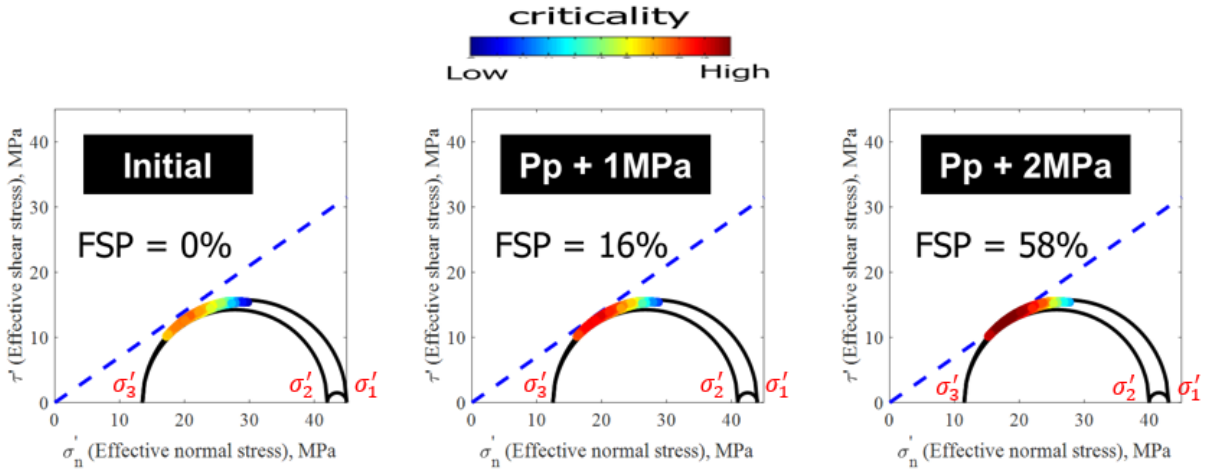

Figure C4 Example illustrates FSP calculation

the initial case, none of the realizations we generated met the Mohr-Coulomb failure criteria, and hence the fault slip potential is 0. For the second case, after pore pressure increased by 1MPa, the Mohr-Circle moved to the left and 16% of the realizations met the failure criteria. With pore pressure further increasing, fault slip potential also elevated in the last case.

One output of our FSP calculation is the fault slip potential for each fault at different times with the corresponding pore pressure change from the simulation result of the calibrated flow model. **Figure C5- Figure C10** show the FSP result of the whole Fort Worth Basin for initial state and in different years with the onset of seismic events. The detailed analysis of FSP results is showed in Chapter IV.

Another output of our FSP calculation is the cumulative density function (CDF) of fault slip potential of the realizations per fault. The calculation of CDF is illustrated by **Figure C11**, in which the horizontal distance between the point of realization and the failure line, meaning the additional pore pressure increase needed for the fault to slip. CDF of the faults held the five earthquake sequences in Fort Worth Basin (6 faults) and faults haven't held earthquake events (9 faults) were generated and showed in **Figure C12**. In **Figure C12**, we could identify a clear difference between the CDF of faults held earthquakes and faults haven't held earthquakes, where the faults held earthquakes is steeper than those haven't held earthquakes. The steep CDF means that the fault is more "dangerous" since it could slip with a slight amount of pore pressure increase; and the flat CDF means the fault is more "safe".

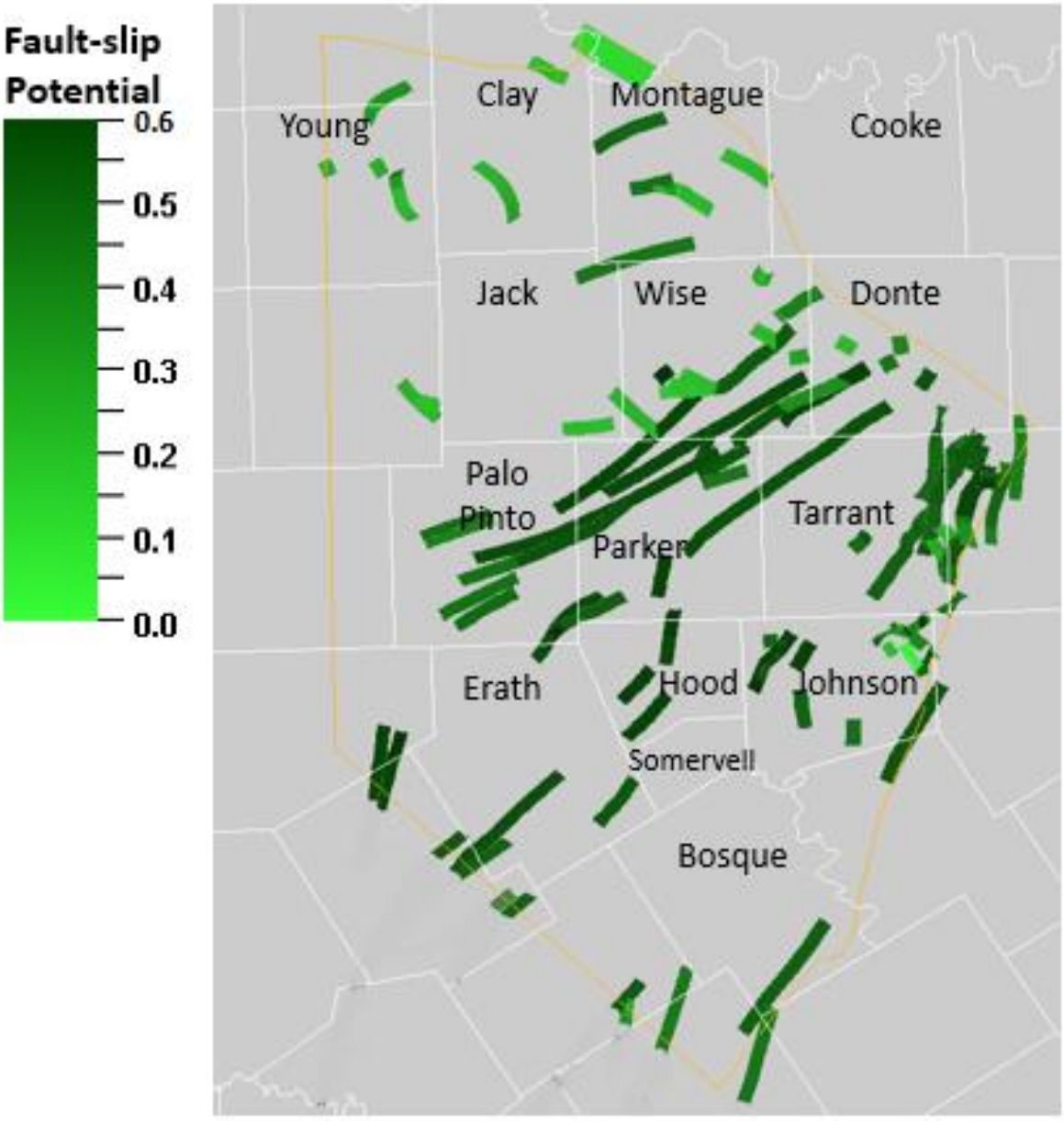

Figure C5 Fault Slip Potential (FSP) of Fort Worth Basin at hydrostatic state

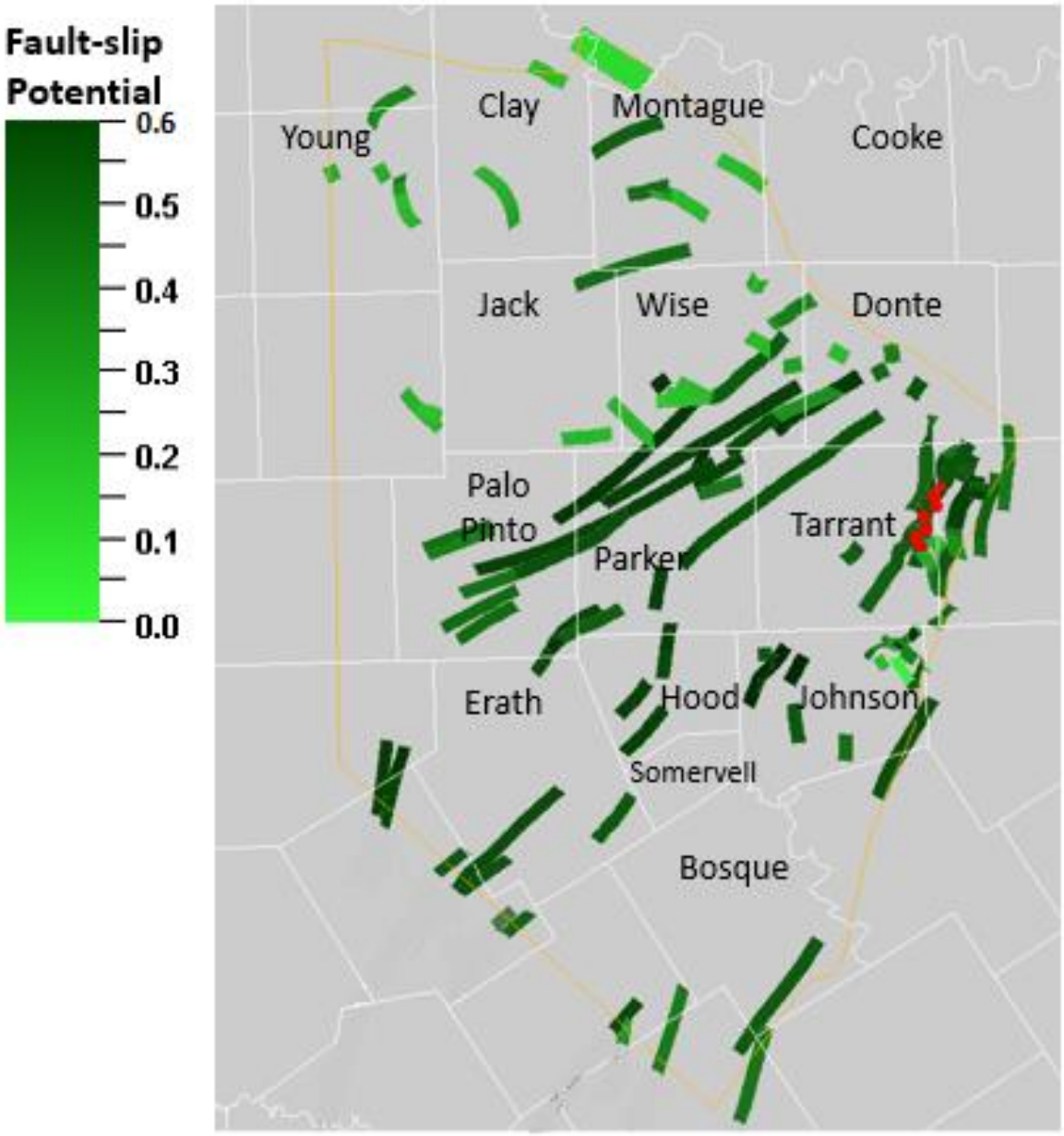

Figure C6 Fault Slip Potential (FSP) of Fort Worth Basin at 2008 superimposed with DFW Airport earthquake

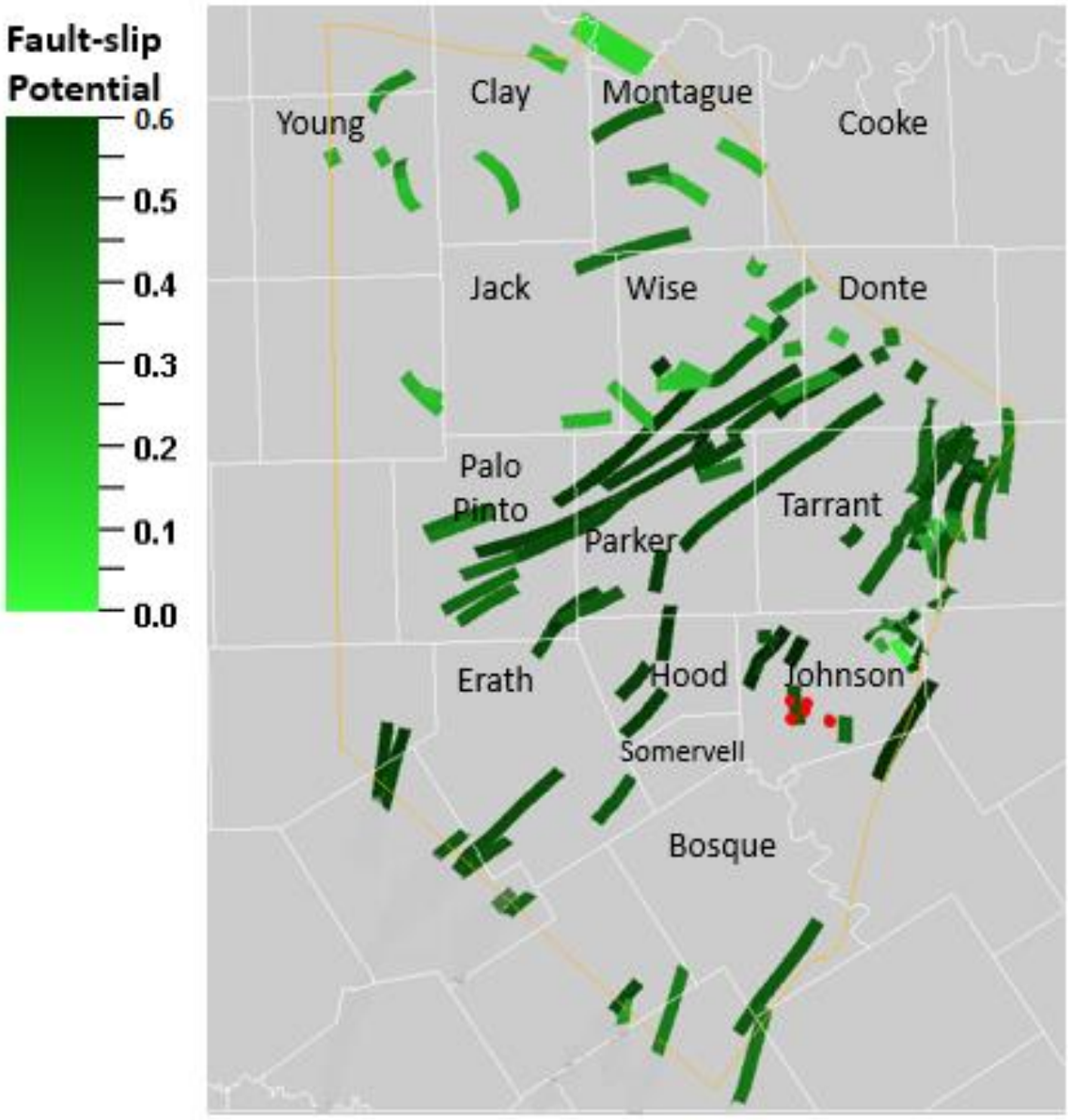

Figure C7 Fault Slip Potential (FSP) of Fort Worth Basin at 2010 superimposed with Cleburne earthquake

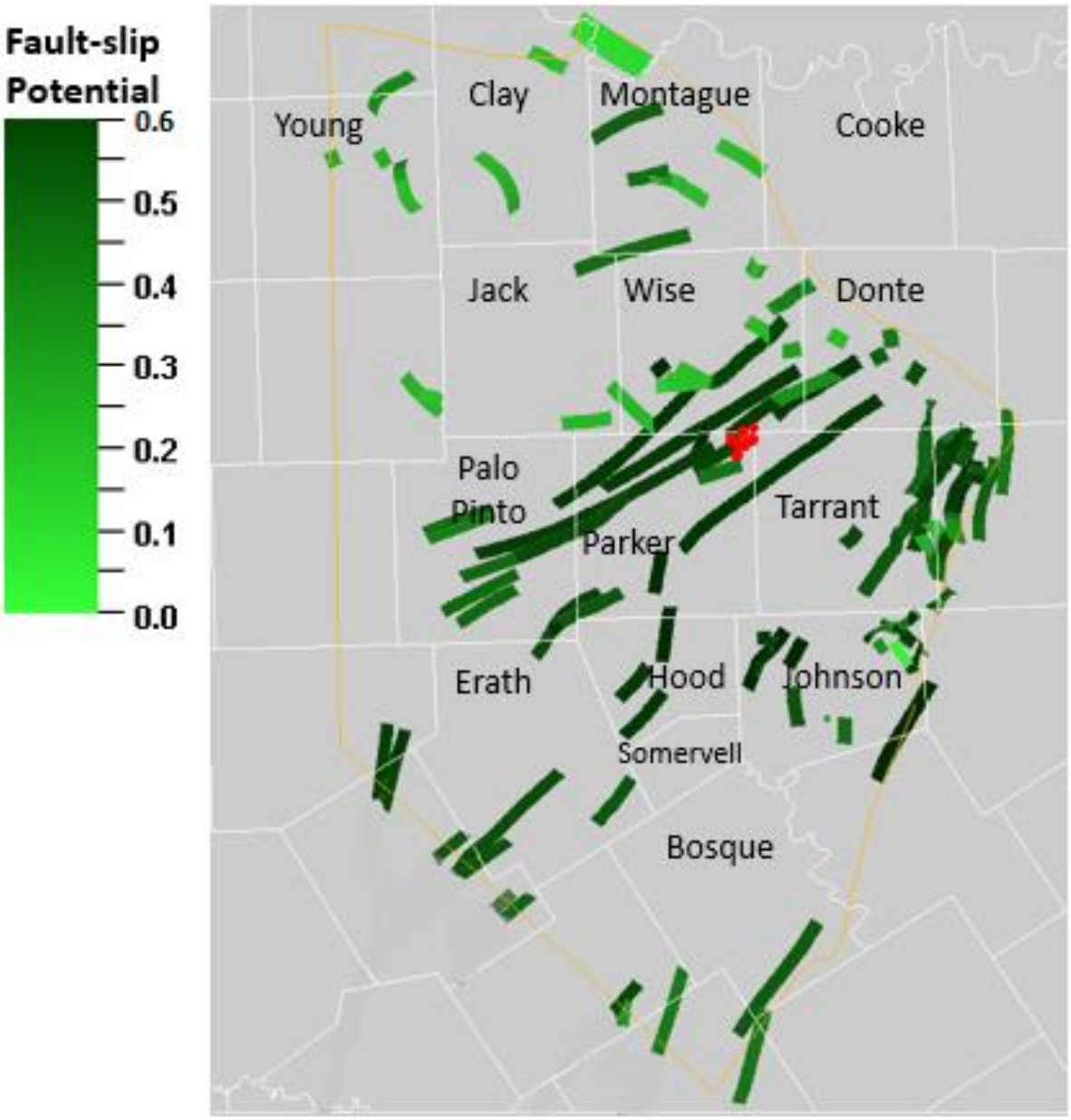

Figure C8 Fault Slip Potential (FSP) of Fort Worth Basin at 2013 superimposed with Azle earthquake

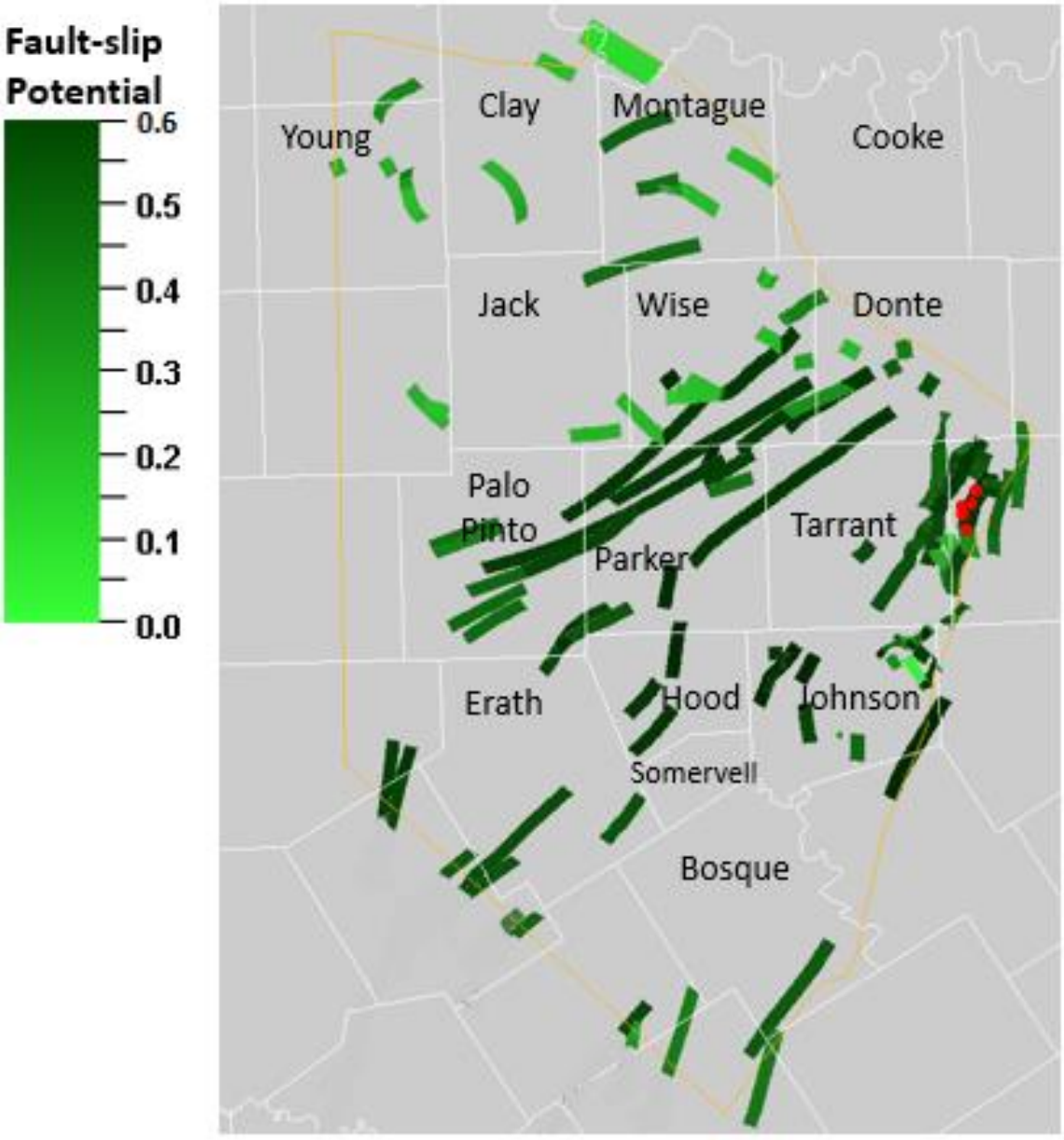

Figure C9 Fault Slip Potential (FSP) of Fort Worth Basin at 2014 superimposed with Irving earthquake

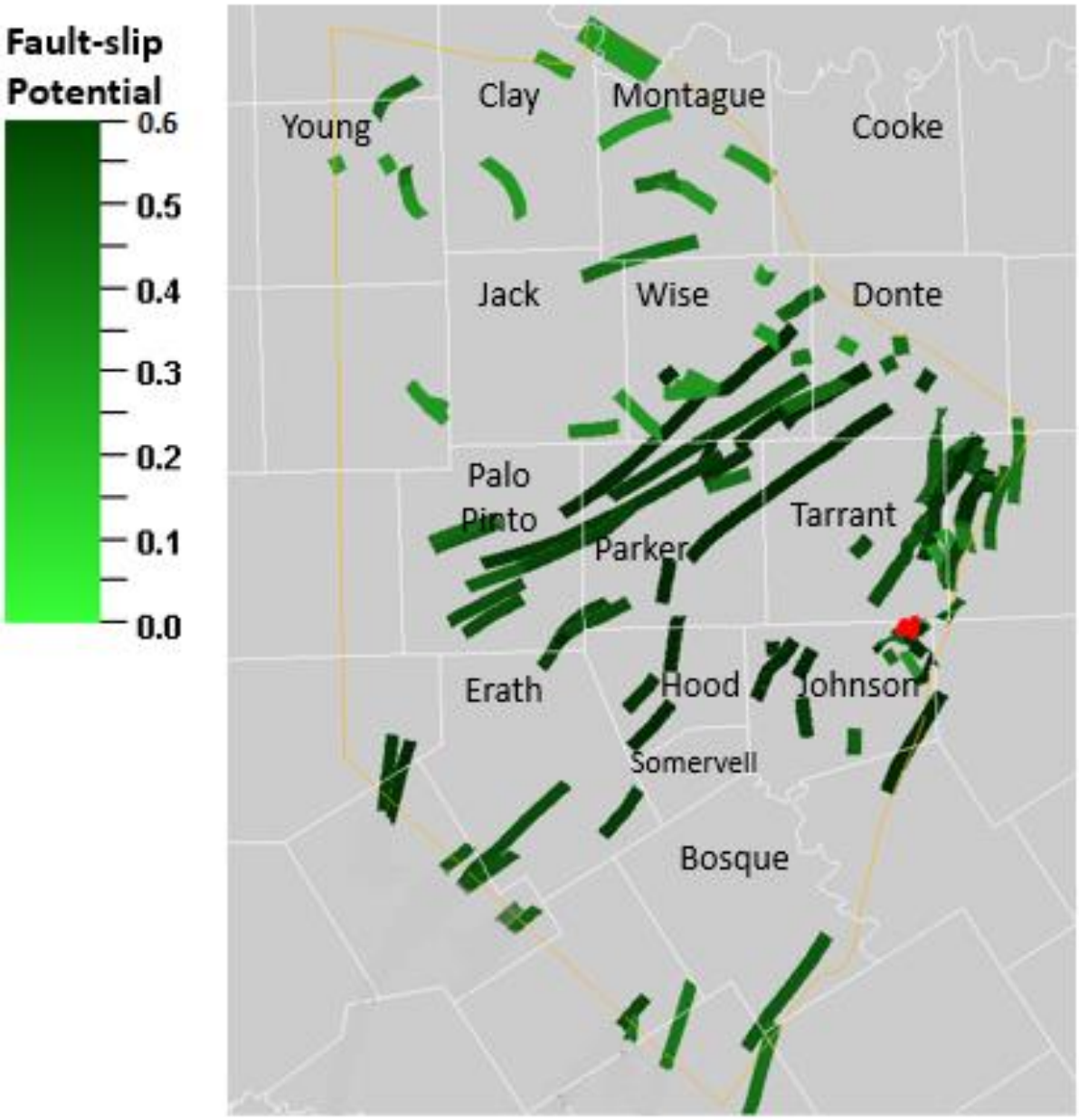

Figure C10 Fault Slip Potential (FSP) of Fort Worth Basin at 2015 superimposed with Venus earthquake

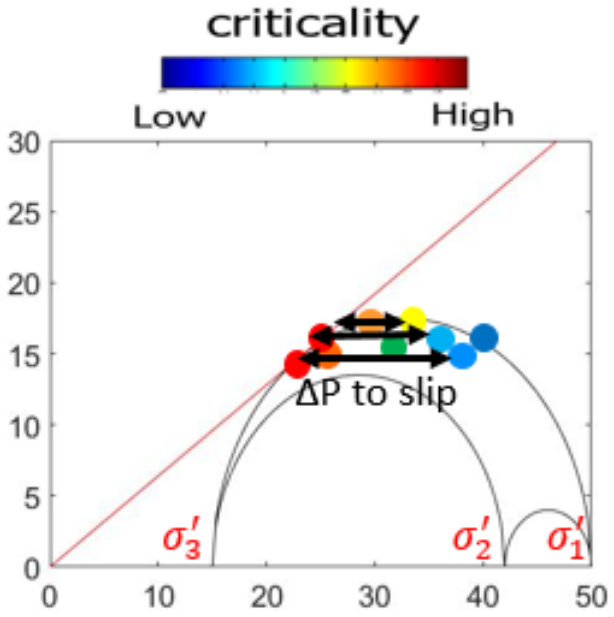

Figure C11 Illustration of the calculation of CDF

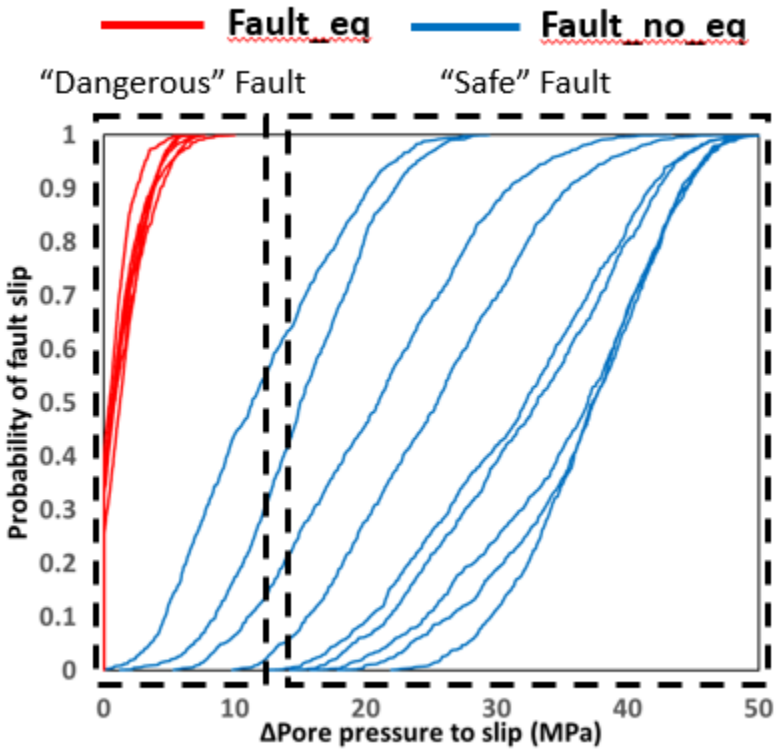

Figure C12 CDF of faults in Fort Worth Basin